

Nanomechanical Properties of Hydrated Organic Thin Films

By

Jae Hyeok Choi

M.S. Civil & Environmental Engineering
Yonsei University, Seoul, Korea 2000

SUBMITTED TO THE DEPARTMENT OF CIVIL & ENVIRONMENTAL
ENGINEERING IN PARTIAL FULFILLMENT OF THE REQUIREMENTS FOR THE
DEGREE OF DOCTOR OF PHILOSOPHY IN THE FIELD OF
NANOMECHANICS AND BIOMATERIALS / STRUCTURES AND MATERIALS
AT THE
MASSACHUSETTS INSTITUTE OF TECHNOLOGY
SEPTEMBER 2007

© 2007 Jae Hyeok Choi. All rights reserved.

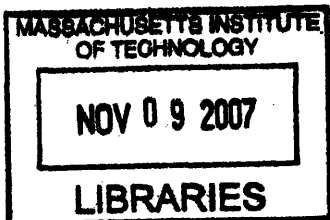
The author hereby grants to MIT permission to reproduce and to distribute publicly paper and
electronic copies of this thesis document in whole or in part
in any medium now known or hereafter created.

Signature of Author: _____
Department of Civil and Environmental Engineering
August 10, 2007

Certified by: _____
Christine Ortiz
Professor of Materials Science and Engineering
Thesis Supervisor

Accepted by: _____
Professor Philip M. Gschwend
Professor of Civil and Environmental Engineering
Chairman of Doctoral Thesis Committee

Accepted by: _____
Daniele Veneziano
Professor of Civil and Environmental Engineering
Chairman of Departmental Committee for Graduate Student



ARCHIVES

Nanomechanical Properties of Hydrated Organic Thin Films

By

Jae Hyeok Choi

SUBMITTED TO THE DEPARTMENT OF CIVIL & ENVIRONMENTAL
ENGINEERING ON AUGUST 10, 2007 IN PARTIAL FULFILLMENT OF
THE REQUIREMENTS FOR THE DEGREE OF DOCTOR OF PHILOSOPHY
IN THE FIELD OF NANOMECHANICS AND BIOMATERIALS
/ STRUCTURES AND MATERIALS

ABSTRACT

Hydrated organic thin films are biological or synthetic molecularly thin coatings which impart a particular functionality to an underlying substrate and which have discrete water molecules associated with them. Such films exist in biology (e.g. cell membrane lipid bilayers) and have a broad array of potential engineering applications (e.g. biological implant and sensor surfaces, marine antifouling paints etc.). This doctoral thesis focuses on two important classes of hydrated organic thin films that were prepared and studied *in vitro*. The first model system was an oligo(ethylene oxide)-based self-assembling monolayer (OEO-SAM) which is a synthetic material that is known to exhibit exceptional resistance to nonspecific protein adsorption and, hence, it is a viable candidate for producing implant surfaces with improved biocompatibility. The second model system was the biologically relevant phosphorylcholine(PC)-supported lipid layer which mimics the structure of the cell membrane. The objective of this doctoral thesis was to quantify the functional form of the net surface interaction (force versus separation distance, $F(D)$), as well as the contact mechanical properties (e.g. elasticity, plasticity, fracture) of these two model systems under different solution conditions, in order to formulate a hypothesis for the molecular origins of the dominant interactions and furthermore, to gain a mechanistic understanding of their *in vivo* function and performance. For the OEO-SAMs, $F(D)$ was found to exhibit the maximum monotonic repulsive functional form for intermediate surface packing densities (~70%) on loading (approach) and negligible adhesion ($F_{adhesion} < 0.3\text{nN}$) on unloading (retract). Both were attributed to an electrostatic component arising from a dipole induced effective surface charge, as well as a nm-thick hydrated water layer. For the PC lipid layers, the effect of length scale on the yield threshold force, F_y , was studied by varying the probe tip end radius, R_{tip} , used for the surface force measurements. F_y decreased by 20x (Force/Radius) as R_{tip} increased from 30 nm to 80 nm, presumably due to the fact that the contact area possessed an increased density of molecular-level defects, thereby causing stress concentrations and a

reduction in mechanical stability of the layer.

Thesis Supervisor: Christine Ortiz

Title: Associate Professor of Materials Science and Engineering

ACKNOWLEDGEMENTS

Thanks Lord, Jesus Christ who has been with me all the time! He guided me sincerely at every moment of my life. He led me have a talent and passion in the interdisciplinary study.

Thanks so much to all! This interdisciplinary thesis would not have been the same without the support of such a large number of people. First, I want to thank Christine Ortiz, my advisor who has always given me great advice about this study and inspired my excitement about interdisciplinary study. I also thank Professor Philip Gschwend who gave me the great inspiration for my research. I appreciate the support from Professors Patrick Jaillet, Oral Buyokozturk, Eduardo Kausel, and Lorna Gibson in MIT. I also give my best gratitude to my previous advisors in Yonsei University, Korea, Professor Keun-Joo Byun, Ha-Won Song, and Jang-Ho Jay Kim. If there had been no support from these professors, I could not have dreamed about the interdisciplinary study. I also thank Professor Haseo Ki in Yonsei University who showed me the passion as a scientist.

My lab-mates have been a great pleasure to work with. I like to thank all present and previous members of the Ortiz group; Delphine, Monica, Celia, Jen, Kuangshin, Miao, Ben, Lin, Bobae, Juha, Hsu-Yi, Hamin, etc. I also thank my all UROP students; Haile, Sarah, and Nan.

My family has been a tremendous support to me. My wife, Suhyeon Chai has always been with me as a friend, lover, and advisor. My son, David Jae Choi has always encouraged me to study hard! My mother, Sungshin Hong has always supported me with a passion and love. My father who knows what is the responsibility of the man, has always done his best for me. He has always been there as a father in this world. I respect

him. My younger sister, Haesun Choi is the one of the wisest people that I have ever met. Sometimes, I feel she is more matured than me.

I really appreciate the great voice lessons by Mr. Robert Honeysucker. He gave me the joy of singing and the happiness to worship God with the well-trained voice. I thank to my Pastor Young-Ho Kim and his wife Young-Ok Whang, who are serving in the First Korean Presbyterian Church in Cambridge. They have always prayed for me and guided me sincerely. I also thank Pastor Tae-Whan Kim and his wife Gyesuk Kim. I also give my best gratitude to Pastor Dae-Sung Choi who has a passion as a Christian Scientist and Pastor Michel Dean. They have always prayed for me and supported me sincerely. Because of their help, I could survive in MIT. I give a sincere gratitude to all previous and present staffs in CEE; Patricia, Pat, Anthee, Dona, Jennet, Kris, Cynthia, etc. Patricia Dixon has always supported and encouraged me. I also thank Patricia Glidden who gave the best help to arrange schedule and print out this nice thesis.

I thank conductor Bill Cutter and all MIT chamber choir members. It was a great time to sing French, Russian, German, Italian, and English art songs and opera arias in MIT as a choir member and soloist.

Lastly, I thank God again for calling me out to MIT and the interdisciplinary study in nanomechanics and biomaterials. The Lord has been with me every step of my life and will surely continue now and on through the end and beyond with this phrase in the bible.

But now thus saith the LORD that created thee, O Jacob, and he that formed thee, O Israel, Fear not: for I have redeemed thee, I have called thee by thy name; thou art mine. (Isaiah Chapter 43:1)

CONTENTS

ABSTRACT	2
ACKNOWLEDGEMENTS.....	4
CONTENTS.....	6
LIST OF FIGURES.....	9
LIST OF TABLES.....	23
CHAPTER 1	24
General Introduction	24
1.1 Hydrated Organic Thin Films	24
1.1.1. Definition	24
1.1.2. Hydrated Organic Thin Films for Use as Protein Resistant Biomaterial Coatings.....	24
1.1.4 Structure and Properties of Oligo(ethylene oxide) Self-Assembling Monolayers (OEO-SAMs).....	26
1.1.5 Structures and Properties of Phosphorylcholine (PC) Lipid Layers.....	30
1.2 Nanomechanical Properties	32
1.2.1 Nanomechanical Experiments.....	32
1.2.2 Theoretical Approach.....	35
1.3 Specific Aim and Nanomechanical Experiments	36
CHAPTER 2	38
Molecular Origins of the Bioinert Properties of Methyl 1-(3-Mercaptopropyl) Penta(ethylene oxide) (C_3EO_5) Self-Assembled Monolayers (SEM).....	38
2.1 Introduction.....	38
2.2 Material Preparation	42
2.2.1 Materials.....	42
2.2.2 SAM Preparation	42
2.2.3 Choices and Preparation of Functionalized Tips	43
2.2.4 Choices of Ionic Strengths.....	44
2.3 Experimental Method	44
2.4 Experimental Results	45
2.4.1 Contact Angle Measurement.....	45
2.4.2 Hydrophilic OH-Terminated Probe Tip vs C_3EO_5 SAM Planar Surface	45
2.4.3 Hydrophobic CH_3 -Terminated Probe Tip vs C_3EO_5 SAM Planar Surface	51
2.4.4 Hydrophilic and Negatively Charged COOH-Terminated Tip vs C_3EO_5	

SAM Planar Surface	51
2.4.5 C ₃ EO ₅ -SAM probe tip versus C ₃ EO ₅ -SAM planar surface	52
2.4.6 Protein (HSA) Functionalized Tip vs C ₃ EO ₅ -SAM	52
2.5 Discussion	63
2.6 Conclusion	69
CHAPTER 3	71
High Resolution Atomic Force Microscopy Imaging of Supported Lipid Bilayers	71
3.1 Introduction.....	71
3.1.1 Theoretical Calculation of the Height of Phosphorylcholine (PC) in an Aqueous Solution	73
3.2 1-Palmitoyl-2-Oleoyl- <i>sn</i> -Glycero-3-Phosphocholine (POPC).....	77
3.2.1 Sample Preparation.....	77
3.2.2 Experimental Method.....	81
3.2.3 POPC AFM Imaging Result & Discussion	83
3.3 1,2-Dipalmitoyl- <i>sn</i> -Glycero-3-Phosphocholine (DPPC).....	95
3.3.1 Sample Preparation.....	95
3.3.2 Selection of AFM probe tips.....	97
3.3.3 Experimental Method.....	97
3.3.4 AFM Imaging Result & Discussion	98
3.4 Conclusion	106
CHAPTER 4	108
High Resolution Force Spectroscopy of Lipid Bilayers as a Function of Solution Ionic Strengths (ISs)	108
4.1 Introduction.....	108
4.2 1-Palmitoyl-2-Oleoyl- <i>sn</i> -Glycero-3-Phosphocholine (POPC).....	111
4.2.1 Sample Preparation.....	111
4.2.2 Experimental Method.....	112
4.2.3 Experimental Results and Discussion	115
4.3 1,2-Dipalmitoyl- <i>sn</i> -Glycero-3-Phosphocholine (DPPC).....	126
4.3.1 Sample Preparation.....	126
4.3.2 Experimental Method.....	127
4.3.3 Experimental Results and Discussion	129
4.4 Interpretation and Comparison with the Literature	137
4.4.1 One-Yield Forces vs. Double-Yield Thresholds.....	137
4.4.2 Change of the Slopes between the First Elastic Compression and the Second Elastic Compression	138

4.5 Conclusion	140
CHAPTER 5	141
Effect of Length Scale and Geometry on the Nanoscale Surface Interactions and Compressibility of Supported Lipid Bilayers	141
5.1 Introduction.....	141
5.2 Materials.....	142
5.2.1 Selection of Lipid.....	142
5.2.2 Sample Preparation.....	143
5.2.3 Selection of Tips.....	143
5.3 Experimental Method	143
5.4 Results and Discussion	144
5.4.1 0.01 M IS condition	144
5.4.2 0.1M IS condition	154
5.5 Conclusion	155
CHAPTER 6	159
Summary and Future Research Directions	159
6.1 Introduction.....	159
6.2 Protein Resistant Design for Synthetic Polymer	159
6.3 Protein Resistant Design for Phosphorylcholine (PC) Lipid Bilayers.....	162
6.4 Future work.....	164
APPENDIX	165
REFERENCES	167

LIST OF FIGURES

Figure 1-1 Possible confirmation of OEO in aqueous solution; OEO may take on a trans-trans-gauche (ttg) configuration where the ether oxygen atoms have hydrogen bonding. 27

Figure 1-2. Chemical structure and self-assembled monolayers (SAMs) of C_3EO_5 on Au. (a) 2D all-trans form, (b) 3D 7/2 helical conformation, (c) 60-80% surface area coverage, (d) 100% coverage of surface. 29

Figure 1-3. Chemical structure of phosphorylcholine (PC). (a) POPC, (b) DPPC, pictures by ©Avanti Polar Lipids. 31

Figure 1-4. Lipid bilayers on the hydrophilic surface (a) Lipid bilayers on mica, (b) Lipid bilayers on a hydrophilic OH-terminated SAM on bare Au; the hydrophilic head group of lipid is green dots and hydrophobic tail is two black chains. 31

Figure 1-5 (a) three main steps in the Langmuir–Blodgett transfer of lipid monolayers from water onto a solid substrate.⁴³ (b) the vesicle fusion technique which is working on the lower diameter (under 100nm diameter) vesicle.⁴⁴ 32

Figure 1-6. Molecular Force Probe (MFP) from Asylum Research. 33

Figure 1-7. PicoForce Atomic Force Microscopy (AFM) from Veeco. 33

Figure 2-1 Several types of conformers of $(EG)_3$ without water molecules (left column), with one water molecule (center column), and with two water molecules.⁵⁸ 34

Figure 2-2 Self-assembled monolayers (SAMs) of C_3EO_5 on Au (a) 7/2 helical conformation, (b) 60~80% coverage of surface area, (c) 100% coverage of surface. 41

Figure 2-3. Static-, advancing- and receding-deionized water-contact angle measurement of unfunctionalized Au substrate and C_3EO_5 self-assembling monolayer from 95% ethanol solution (0.5 mM) at room temperature 25°C. Each bar represents the mean of 4 locations on one sample. The Hi-Lo bars show the standard deviation. The difference of contact angle between Au (0% surface coverage) and 5 seconds (60-80% coverage) or 5 seconds (60-80% coverage) and 3 hours (near to 100%) is statistically significant. 46

Figure 2-4. Nanomechanical data for OH-terminated self-assembling monolayer (SAM)-coated cantilever tip vs C_3EO_5 SAMs on flat Au as a function of incubation time in the C_3EO_5 solution (95% ethanol, 0.5 mM) and ionic strength of the aqueous media during the approach and retract. Graphs (a), (c), and (e) are the approach curves for incubation times of 5 seconds, 24 hours, and 3 days, respectively. Graphs (b), (d), and (f) are the corresponding retract curves. A *Veeco* Au-coated Digital Instruments cantilever tip was used (spring constant: 0.06 N/m, probe tip end radius: 100 nm, displacement rate = 1 μ m/sec). All experiments were carried out with a single probe tip. 48

Figure 2-4A (Magnified from Figure 2-4). Nanomechanical data for OH-terminated self assembling monolayer (SAM)-coated cantilever tip vs C_3EO_5 SAMs on flat Au as a function of incubation time in the C_3EO_5 solution (95% ethanol, 0.5 mM) and ionic strength of the aqueous media during approach and retract Graphs (a), (c), and (e) are the approach curves for incubation times of 5 seconds, 24 hours, and 3 days, respectively. Graphs (b), (d), and (f) are the corresponding retract curves. A *Veeco* Au-coated Digital Instruments cantilever tip was used (spring constant: 0.06 N/m, probe tip end radius: 100 nm, displacement rate = 1 μ m/sec). All experiments were carried out with a single probe tip. 49

Figure 2-5. (a) Adhesion force and (b) pull-off frequency histogram plots of the retract curves for the OH-terminated self-assembling monolayer (SAM)-coated cantilever tip vs C_3EO_5 SAMs on flat Au (incubation time = 24 hr; 1M ionic strength); (c) and (d) are analogous plots of retract curves for C_3EO_5 SAMs (incubation time = 3 days; 1 M ionic strength). 50

Figure 2-6. Nanomechanical data for CH₃-terminated self assembling monolayer (SAM)-coated cantilever tip vs C₃EO₅ SAMs on on flat Au as a function of incubation time in the C₃EO₅ solution (95% ethanol, 0.5 mM) and the ionic strength of the aqueous media during approach and retract. Graphs (a), (c), and (e) are the approach curves for incubation times of 5 seconds, 24 hours, and 3 days, respectively. Graphs (b), (d), and (f) are the corresponding retract curves. A Veeco Au-coated Digital Instruments cantilever tip was used (spring constant: 0.06 N/m, probe tip end radius: 96 nm, displacement rate = 1 μm/sec). All experiments were carried out with a single probe tip.

53

Figure 2-6A (Magnified from Figure 2-6). Nanomechanical data for CH₃-terminated self assembling monolayer (SAM)-coated cantilever tip vs C₃EO₅ SAMs on on flat Au as a function of incubation time in the C₃EO₅ solution (95% ethanol, 0.5 mM) and ionic strength of the aqueous media during approach and retract. Graphs (a), (c), and (e) are the approach curves for incubation times of 5 seconds, 24 hours, and 3 days, respectively. Graphs (b), (d), and (f) are the corresponding retract curves. A Veeco Au-coated Digital Instruments cantilever tip was used (spring constant: 0.06 N/m, probe tip end radius: 100 nm, displacement rate = 1 μm/sec). All experiments were carried out with a single probe tip.

54

Figure 2-7. (a) Adhesion force and (b) pull off frequency histogram plots of retract curves for the CH₃-terminated self assembling monolayer (SAM)-coated cantilever tip vs C₃EO₅ SAMs on flat Au (incubation time = 24 hr; 1 M ionic strength). (c) and (d) Analogous plots of retract curves for C₃EO₅ SAMs (incubation time = 3 days; 1 M ionic strength). There appears to be a regular distribution similar to that found in Figure 2-5.

55

Figure 2-8. Nanomechanical data for COOH-terminated self assembling monolayer (SAM)-coated cantilever tip vs C₃EO₅ SAMs on on flat Au as a function of incubation time in the C₃EO₅ solution (95 approach and retract. % ethanol, 0.5 mM) and ionic strength of the aqueous media during Graphs (a), (c), and (e) are the approach curves for incubation times of 5 seconds, 24 hours, and 3 days, respectively. Graphs (b), (d), and (f) are the corresponding retract curves. A Veeco Au-coated Digital Instruments cantilever tip was used (spring constant: 0.06 N/m, probe tip end radius: 100 nm,

displacement rate = $1\ \mu\text{m}/\text{sec}$). All experiments were carried out with a single probe tip.

56

Figure 2-8A (magnified from Figure 2-8). Nanomechanical data for COOH-terminated self assembling monolayer (SAM)-coated cantilever tip vs C_3EO_5 SAMs on on flat Au as a function of incubation time in the C_3EO_5 solution (95% ethanol, 0.5 mM) and ionic strength of the aqueous media during approach and retract. Graphs (a), (c), and (e) are the approach curves for incubation times of 5 seconds, 24 hours, and 3 days, respectively. Graphs (b), (d), and (f) are the corresponding retract curves. A *Veeco* Au-coated Digital Instruments cantilever tip was used (spring constant: 0.06 N/m, probe tip end radius: 100 nm, displacement rate = $1\ \mu\text{m}/\text{sec}$). All experiments were carried out with a single probe tip.

57

Figure 2-9. Nanomechanical data for C_3EO_5 -terminated self assembling monolayer (SAM)-coated cantilever tip vs C_3EO_5 SAMs on on flat Au as a function of incubation time in the C_3EO_5 solution (95% ethanol, 0.5 mM) and ionic strength of the aqueous media during approach and retract. Graphs (a), (c), and (e) are the approach curves for incubation times of 5 seconds, 24 hours, and 3 days, respectively. Graphs (b), (d), and (f) are the corresponding retract curves. A *Veeco* Au-coated Digital Instruments cantilever tip was used (spring constant: 0.06 N/m, probe tip end radius: 100 nm, displacement rate = $1\ \mu\text{m}/\text{sec}$). All experiments were carried out with a single probe tip.

58

Figure 2-9A (magnified from 2-9). Nanomechanical data for C_3EO_5 -terminated self assembling monolayer (SAM)-coated cantilever tip vs C_3EO_5 SAMs on on flat Au as a function of incubation time in the C_3EO_5 solution (95% ethanol, 0.5 mM) and ionic strength of the aqueous media during approach and retract. Graphs (a), (c), and (e) are the approach curves for incubation times of 5 seconds, 24 hours, and 3 days, respectively. Graphs (b), (d), and (f) are the corresponding retract curves. A *Veeco* Au-coated Digital Instruments cantilever tip was used (spring constant: 0.06 N/m, probe tip end radius: 100 nm, displacement rate = $1\ \mu\text{m}/\text{sec}$). All experiments were carried out with a single probe tip.

59

Figure 2-10. Nanomechanical data for Protein (Human Serum Albumin)-functionalized

cantilever tip vs C_3EO_5 self assembling monolayers (SAMs) on flat Au as a function of incubation time in the C_3EO_5 solution (95% ethanol, 0.5 mM) and ionic strength of the aqueous media during approach and retract. Graphs (a), (c), and (e) are the approach curves for incubation times of 5 seconds, 24 hours, and 3 days, respectively. Graphs (b), (d), and (f) are the corresponding retract curves. A Veeco Au-coated Digital Instruments cantilever tip was used (spring constant: 0.06 N/m, probe tip end radius: 100 nm, displacement rate = $1\mu\text{m}/\text{sec}$). All experiments were carried out with a single probe tip.

60

Figure 2-10A (magnified from Figure 2-10). Nanomechanical data for Protein (Human Serum Albumin)-functionalized cantilever tip vs C_3EO_5 self assembling monolayers (SAMs) on flat Au as a function of incubation time in the C_3EO_5 solution (95% ethanol, 0.5 mM) and ionic strength of the aqueous media during approach and retract. Graphs (a), (c), and (e) are the approach curves for incubation times of 5 seconds, 24 hours, and 3 days, respectively. Graphs (b), (d), and (f) are the corresponding retract curves. A Veeco Au-coated Digital Instruments cantilever tip was used (spring constant: 0.06 N/m, probe tip end radius: 100 nm, displacement rate = $1\mu\text{m}/\text{sec}$). All experiments were carried out with a single probe tip.

61

Figure 2-11. Nanomechanical data for CH_3 , mica, OH, and COOH SAM on AU vs. an HSA protein tip. (a) approach curves and (b) retract curves. An Au-coated Digital Instruments cantilever tip was used (spring constant: 0.06 N/m, displacement rate = $1\mu\text{m}/\text{sec}$).

62

Figure 2-12. Nanomechanical data for all types of cantilever tips vs 5 second incubated C_3EO_5 SAMs on flat Au in the C_3EO_5 solution (95% Ethanol, 0.5 mM) with different ionic strengths of the aqueous media during approach. Graphs (a), (c) & (e) are on 0.01 M, 0.1 M & 1 M ISs of aqueous media consecutively. Graphs (b), (d) & (f) are magnified from (a), (c) & (e) consecutively. Veeco Au-coated Digital Instruments cantilever tips were used (spring constant: 0.06 N/m, displacement rate = $1\mu\text{m}/\text{sec}$). 64

Figure 2-13. Numerical calculation of the average force (nN) versus distance, D (nm). The experimental C_3EO_5 -terminated self assembling monolayer (SAM)-coated cantilever tip vs C_3EO_5 SAMs on flat Au approach curve (blue) is compared to the

DLVO electrostatic surface charge model (electrostatic force + van der Waals force, pink), the only van der Waals force model (yellow), and the only electrostatic force mode model (green), $\kappa^{-1} = 3 \text{ nm}$, IS = 0.01 M, Hamaker constant, $D = 0.33 \cdot 10^{-20} \text{ J}$, fitting range: 5 ~ 15 nm. σ_{eff} of the C_3EO_5 -SAM was numerically calculated as -0.0069 C/m^2

68

Figure 3-1. Schematic of endothelium cell membrane⁹³

72

Figure 3-2. Chemical structure of phosphorylcholine (PC) (a) POPC, (b) DPPC, pictures by ©Avanti Polar Lipids.

73

Figure 3-3. DMPC structure in fluid- and hydrogen-bonded oxygen atoms on the head group near phosphate phosphorus and nitrogen chloride. Adapted from reference.¹⁰⁶

75

Figure 3-4. Typical structure of the phosphorylcoline lipid bilayer on a flat mica substrate. Lipid bilayer picture from Wikipedia (http://en.wikipedia.org/wiki/Lipid_bilayer).

77

Figure 3-5. Distribution of POPC vesicle size by a particle size analyzer (90 Plus Particle Size Analyzer, Brookhaven Instruments Corporation).

78

Figure 3-6. Tip images from scanning electronic microscope (SEM) (a) CH_3 -terminated tip, and (b) OH-terminated tip. Gold-coated Veeco pyramidal DNP silicon nitride tips (spring constant: 0.06N/m) were incubated in 5mM solution of 11-Mercapto-undecanol ($\text{HS}-(\text{CH}_2)_{11}\text{-OH}$) and 30 μL of 1-dodecanethiol ($\text{HS}-(\text{CH}_2)_{11}\text{-CH}_3$) in an ethanol solvent.

79

Figure 3-7. The Microcontact-Printing procedure.

74

Figure 3-8. SPR result: a flowing POPC vesicle on the CH_3 -terminated SAM. 0.2 mM POPC vesicles (size < 50 nm) in 10 mM Tris buffer (150 mM NaCl, pH 7.8).

81

Figure 3-9. Schematic view of AFM scan on the lipid bilayer and monolayer which is on the surface of hydrophilic OH-terminated SAM and hydrophobic CH₃-terminated SAM (not drawn to scale). 82

Figure 3-10. Height images and section analysis on contact mode (a) μ CP AFM images of CH₃- and OH- terminated SAMs in deionized water before POPC incubation (control samples), (b) μ CP AFM images of SAM functionalized samples in Tris buffer after POPC incubation, (c) cross-sectional analysis of the selected line from the image of (b). 85

Figure 3-11. Average height difference between hydroxyl and methyl SAMs before and after POPC incubation measured in tapping mode. Three images were scanned continuously on the same position. 86

Fig 3-12. Friction images on contact mode (a) μ CP AFM images of CH₃- and OH-terminated SAMs in deionized water before POPC incubation (control samples), (b) μ CP AFM images of the SAM functionalized samples in Tris buffer after POPC incubation. 87

Figure 3-13. Phase images in tapping mode (a) μ CP AFM images of CH₃- and OH-terminated SAMs in deionized water before POPC incubation (control samples), (b) μ CP AFM images of the SAM functionalized samples in Tris buffer after POPC incubation. 87

Figure 3-14. AFM height images and section analysis from POPC vesicle incubation (a) & (a') μ -printed OH- (light outside) and CH₃-terminated SAM (dark line), (b) & (b') after 15 min. POPC incubation, lipid bilayer on OH-SAM and monolayer on CH₃-SAM, (c) & (c') after 3 hours POPC incubation. 90

Figure 3-15. 1 μ m x 1 μ m AFM images for the POPC incubating time intervals (no POPC, 15 minutes, every 3 hr for incubating, rinsing and changing ionic strength) by using OH-terminated tip and OH-terminated SAM. 92

Figure 3-16. 200 nm x 200 nm AFM images for the intervals of the POPC incubating time (every 3 hr for incubating, rinsing and changing ionic strength) by using OH-terminated tip and OH-terminated SAM. 93

Figure 3-17. Several sizes of images after 3 hr incubation & 3 hr rinsing 94

Figure 3-18. AFM images after square test on 1 M IS 94

Figure 3-19. Setup and procedure of direct deposit method (a) setup, (b) before dropping, (c) immediately after dropping, (d) after drying out. 97

Figure 3-20. Tip images from scanning electronic microscope (SEM). (a) Veeco DNP tip, (b) Veeco DNP-S (sharpened) tip (spring constant: 0.06N/m), (c) μ masch sting tip, and (d) Vista tip. 98

Figure 3-21. AFM deflection images of DPPC lipid bilayer and monolayer on the boundary of bilayers. (a) 3 μ m x 3 μ m (the “square test” was performed in the middle of the left image), (b) 500 nm x 500 nm, and (c) 287.9 nm x 287.9 nm. AFM images on (b) and (c) are from the randomly selected area of (a). AFM images on (b) and (c) were not exposed to the square test. DNP-S (sharpened) tip was used with the low scan rate (under 0.8Hz) in 10mM tris (hydroxymethyl) aminomethane buffer (0.01M IS, pH 7.6). Sample was prepared by direct deposit method. 103

Figure 3-22. AFM height images and section analysis of lipid bilayer and monolayer on the boundary of bilayers. (a) 3 μ m x 3 μ m (the “square test” was performed in the middle of the left image), (b) 500 nm x 500 nm, and (c) 287.9 nm x 287.9 nm. Images are the same as those in Figure 3-17. DNP-S tip was used with the low scan rate (under 0.8 Hz) in 10 mM tris (hydroxymethyl) aminomethane buffer (0.01M IS, pH 7.6). Sample was prepared by the upgraded direct deposit method. 103

Figure 3-23. AFM images of lipid bilayer by (a) 5 μ m x 5 μ m by using DNP-S (sharpened) tip on 0.1M IS, (b) 5 μ m x 5 μ m by using Vista tip on 0.01 M IS (the end radii of the tip is under 10 nm diameter), and (c) 5 μ m x 5 μ m by using μ masch Sting tip on 0.01M IS. Tips were used with the low scan rate under 0.8 Hz. Sample was prepared

by the upgraded direct deposit method. 10 mM Tris buffer was used. 104

Figure 3-24. AFM images of the lipid bilayer by using an μ masch Sting tip after changing IS from 0.01M to 0.1M. (a) 7.5 μ m x 7.5 μ m, (b) 5 μ m x 5 μ m, and (c) 1.2 μ m x 1.2 μ m. Scanning images continuously from (a) to (c) made the surface more homogeneous. The debris (white spots on (a)) after changing from 0.01 M to 0.1 M ionic strength buffer disappeared after several scans. The low scan rate (under 0.8 Hz) was used in 10 mM tris (hydroxymethyl) aminomethane buffer (0.1 M IS, pH 7.6). This sample was prepared with the upgraded direct deposit method. 105

Figure 4-1. Effect of NaCl in lipid molecule packing.¹²⁵ 109

Figure 4-2. Schematic of HRFS experiment involving compression of opposing lipid monolayers; the size of the lipids and CH₃-terminated SAMs are not drawn to scale. 114

Figure 4-3. Schematic of the HRFS experiment involving compression of opposing lipid bilayers; the size of the lipids and OH-terminated SAMs are not drawn to scale. 114

Figure 4-4. Examples of Individual Force-Distance curves on approach of opposing POPC mono layers interaction (Figure 4-2). (a) 0.01 M IS and (b) 0.1 M IS. On 1 M IS, same shape of two yield threshold forces were observed as shown in (b). Only difference is that the yield threshold forces were higher on 1 M IS than on 0.1 M IS. 117

Figure 4-5 Plots on approach of opposing POPC mono-layer interactions (Figure 4-2). (a) Plots of a normalized first-yield threshold force with varying ionic strengths. (b) Plots of the first-yield threshold distance (the initial distance of break-through force) with varying ionic strengths. The difference is considered extremely statistically significant in force and distance as the IS changes from 0.01 M to 0.1 M (force: $p < 0.0003$, distance $p < 0.0001$). or 1 M ($p < 0.0001$). 118

Figure 4-6. Plots on approach of opposing POPC mono layers interaction (Figure 4-2). (a) Plots of a normalized second yield threshold force with varying ionic strengths. (b) Plots of the second yield threshold distance (the initial distance of breakthrough force) with varying ionic strengths. The difference is considered to be extremely statistically significant in the force as IS is changed from 0.01M to 0.1M or 1M ($p < 0.0001$). 119

Figure 4-7. 2 Two-dimensional distribution and histograms of nanomechanical test on the approach of opposing POPC mono-layers interaction. (a) Distribution of the first yield threshold distances and forces with varying ionic strengths, (b) & (c) histogram of yield threshold distances and forces with 0.01 M IS (d) & (e); histogram of yield threshold distances and forces with 0.1 M IS (f) & (g), histogram of yield threshold distances and forces with 1 M IS. 120

Figure 4-8. 2 Two-dimensional distribution and histograms of nanomechanical test on approach of opposing POPC mono-layers interaction. (a) Distribution of the second yield threshold distances and forces with varying ionic strength, (b) & (c) histogram of yield threshold distances and forces with 0.01 M IS; (d) & (e) histogram of yield threshold distances and forces with 0.1 M IS, (f) & (g) histogram of yield threshold distances and forces with 1 M IS. 121

Figure 4-9. Individual force-distance curves on approach of opposing POPC bilayers interaction (Figure 4-3). (a) 0.01 M IS (b) 0.1 M IS and (c) 1 M IS solution concentration. 122

Figure 4-10. Plots on opposing POPC bilayers interactions (Figure 4-3). (a) Plots of the yield threshold force with varying ionic strength (b); plots of the yield threshold distance (the initial distance of breakthrough force) with varying ionic strengths. The difference is considered extremely statistically significant in force and distance as IS changes from 0.01 M to 1 M ($p < 0.0001$). 123

Figure 4-11. Two-Dimensional distribution and histograms for a nanomechanical test on

opposing POPC bilayers interaction (Figure 4-3). (a) Distribution of yield threshold distances and forces with varying ionic strengths; (b) & (c) histogram of first yield threshold distances and forces with 0.01 M IS; (d) & (e) histogram of yield threshold distances and forces with 0.1 M IS; (f) & (g) histogram of yield threshold distances and forces with 1 M IS. 124

Figure 4-12. Schematic drawings of potential interaction mechanisms between lipid bilayers from SFA study.¹²⁰ 126

Figure 4-13. Plots of the yield threshold force with varying tip speed on approach. The difference in yield threshold forces between 100 nm/s and 200nm/s ($p < 0.0168$) is statistically significant. 128

Figure 4-14. Schematic of the HRFS experiment involving the interaction of a bare Si_3N_4 AFM probe tip and a single lipid bilayer supported on planar mica. 128

Figure 4-15. Nanomechanical data on the approach of the silicon nitride cantilever tip vs. the DPPC lipid bilayers on flat mica. (a) 0.01 M IS (b) 0.1 M IS and (c) 1 M IS. 131

Figure 4-16. Typical individual approach curves for a DPPC-functionalized silicon nitride probe tip vs. a DPPC-functionalized substrate on 1 M IS (spring constant: 0.06 N/m, radius: 60 nm, displacement rate = 100 nm/sec). 132

Figure 4-17. (a) Plots of a normalized first yield threshold force with varying ionic strengths. (b) Plots of the first yield threshold distance (the initial distance of breakthrough force) with varying ionic strengths. Because there is only one yield-threshold force and a distance of 0.01 M IS, these are plotted together. 133

Figure 4-18. (a) Plots of a normalized second yield threshold force with varying ionic strengths. (b) Plots of the second yield threshold distance (the initial distance of

breakthrough force) with varying ionic strengths. Because there is only one yield threshold force and distance of 0.01 M IS, these are plotted together. The difference is considered extremely statistically significant in the force as IS changes from 0.01 M to 1 M ($p < 0.0001$) and in the distance IS changes from 0.01 M to 0.01 M or 0.1 M ($p < 0.0001$).

134

Figure 4-19. Two-dimensional distribution and histograms of a nanomechanical test (DPPC bilayer on mica vs. Veeco DNP tip). (a) Distribution of the first yield threshold distances and forces with varying ionic strengths; (b) & (c) histogram of yield threshold distances and forces with 0.01 M IS (d) & (e); histogram of yield threshold distances and forces of 0.1 M IS; (f) & (g) histogram of yield threshold distances and forces with 1 M IS.

135

Figure 4-20. Two-dimensional distributions and histograms of a nanomechanical test (DPPC bilayer on mica vs. Veeco DNP tip). (a) Distribution of the second yield threshold distances and forces with varying ionic strengths; (b) & (c) histogram of yield threshold distances and forces with 0.01 M IS; (d) & (e) histogram of yield threshold distances and forces with 0.1 M IS; (f) & (g) histogram of yield threshold distances and forces with 1 M IS.

136

Figure 5-1 Nanomechanical data on approach. (a) μ masch sting ($R_{tip} \sim 30$ nm), (b) DNP-S ($R_{tip} \sim 50$ nm), (c) DNP ($R_{tip} \sim 80$ nm) silicon nitride cantilever tip vs DPPC lipid bilayers on flat mica with Tris buffer (0.01 M IS).

147

Figure 5-2. (a) Nanomechanical data on the approach of (a) μ masch sting ($R_{tip} \sim 30$ nm), silicon nitride cantilever tip on DPPC lipid bilayers (unclear yield threshold) on flat mica or flat mica with Tris buffer (0.01 M IS); (b) Plots of normalized ultimate forces of the DPPC bilayers (0.01 M IS) when the tip reaches the compliance regime of HRFS with DNP ($R_{tip} \sim 80$ nm), DNP-S ($R_{tip} \sim 50$ nm) and μ masch sting ($R_{tip} \sim 30$ nm) probe tips.

148

Figure 5-3 (a) Nanomechanical data on the approach of (a) μ masch sting ($R_{tip} \sim 30$ nm),

silicon nitride cantilever tip on DPPC lipid bilayers (unclear yield threshold) on flat mica or flat mica with Tris buffer (0.01 M IS); (b) Plots of normalized ultimate forces of the DPPC bilayers (0.01 M IS) when the tip reaches the compliance regime of HRFS with DNP ($R_{tip} \sim 80$ nm), DNP-S ($R_{tip} \sim 50$ nm) and μ masch sting ($R_{tip} \sim 30$ nm) probe tips.

150

Figure 5-4 (a) Force distribution (700 nm x 700 nm size); (b) AFM image (500 nm x 500 nm size); and (c) Threshold distribution (700 nm x 700 nm size) of HRFS data with DNP-S ($R_{tip} \sim 30$ nm) probe tip (0.01 M IS). Spacing in each HRFS experiment is 100 nm and the HRFS experiment was performed only one time in each position. The dark gray boxes indicate a clear yield threshold (well-packed DPPC layers), light gray boxes, an unclear yield threshold (less packed DPPC layers), and white boxes indicates no yield threshold (no DPPC layers).

151

Figure 5-5 (a) Force distribution (b) AFM image, and (c) Threshold distribution (1 μ m x 1 μ m size) of HRFS data with μ masch sting ($R_{tip} \sim 30$ nm) probe tip (0.1 M IS). Spacing in each HRFS experiment is 100 nm and the HRFS experiment was performed only one time in each position. The dark gray boxes indicate a clear yield threshold (well-packed DPPC layers), light gray boxes, an unclear yield threshold (less packed DPPC layers), and white boxes indicates no yield threshold (no DPPC layers).

152

Figure 5-6 Nanomechanical data on approach. (a) μ masch sting ($R_{tip} \sim 30$ nm), (b) DNP ($R_{tip} \sim 80$ nm) silicon nitride cantilever tip vs DPPC lipid bilayers on flat mica with Tris buffer (0.1 M IS).

156

Figure 5-7 (a) Plots of the normalized yield threshold forces of DPPC bilayers (0.1 M IS) with varying probe tips; DNP ($R_{tip} \sim 80$ nm) and μ masch sting ($R_{tip} \sim 30$ nm) in order, (b) Plots of the yield threshold distances of DPPC bilayers on 0.1 M IS with varying probe tips; DNP ($R_{tip} \sim 80$ nm), and μ masch sting ($R_{tip} \sim 30$ nm) in order. Only DNP probe tip has consistent two yield threshold forces.

157

Figure 5-8 (a) Force distribution, (b) AFM image, and (c) Threshold distribution ($1\mu\text{m} \times 1\mu\text{m}$ size) of HRFS Data with μmasch sting ($R_{\text{tip}} \sim 30\text{nm}$) probe tip (0.1M IS). Each space between HRFS experiment is 100nm and only one time HRFS experiment was performed per one position. Colors stand for dark gray: clear yield threshold (well packed DPPC layers), light gray: unclear yield threshold (less packed DPPC layers), white: no yield threshold (no DPPC layers). 159

Figure 6-1 Repulsive interaction mechanism of the HRFS experiment between protein functionalized or chemically terminated tip vs. C_3EO_5 SAM at 60-80% surface coverage. 160

Figure 6-2. Example of a graft copolymer. A & B are monomers. Structural Unit 1 is composed of A monomers and Structural Unit 2, of B monomers. 161

Figure A-1 (a) STM image ($6\text{nm} \times 6\text{nm}$) of Octanethiol on Au (111). The $(2\sqrt{3} \times 3)$ unit mesh and $c(4 \times 2)$ superlattice unit cell are outlined¹³¹. (b) Plot of cross-section B in (a) running in the Au nearest-neighbor (NN) direction. (C and D) Cross-sectional plots running in two of the Au next-nearest-neighbor (NNN) directions.¹³¹ (c) High-resolution STM image showing $c(4 \times 2)$ superstructure containing three different molecular states in a unit cell ($3.8 \text{ nm} \times 3.8 \text{ nm}$)¹³². (d) Schematic model describing the $c(4 \times 2)$ superstructure. White circles correspond to gold atoms and colored circles correspond to alkanethiol molecules.¹³² 166

LIST OF TABLES

Table 3-1. Theoretical calculation of the length of the lipid tail groups for DPPC, DMPC and POPC. 76

CHAPTER 1

General Introduction

1.1 Hydrated Organic Thin Films

1.1.1. Definition

In this study, hydrated organic thin films are biological or synthetic molecularly thin coatings that impart a particular functionality to underlying substrates and are associated with discrete water molecules.^{1,2} Self-assembled monolayers (SAMs), polyelectrolyte multilayers, lipid bilayers, and polymer brushes are examples of hydrated organic thin films. They can be either monolayers or multilayers ranging from a few nm to tens of μm in thickness.

1.1.2. Hydrated Organic Thin Films for Use as Protein Resistant Biomaterial Coatings

Implanted biomaterials such as vascular grafts, stents, pacemakers, sensors, catheters, joint replacements, and contact lenses³ are frequently coated or functionalized with a thin hydrated organic thin film to improve *in vivo* biocompatibility.^{4,5,6} These coatings function by reducing the nonspecific protein adsorption to the biomaterial surface, which, for blood-contacting devices for example, frequently leads to initiation of a coagulation cascade, thrombosis, inflammation, and infection. However, the coatings in use today are imperfect and protein adsorption invariably occurs with sufficient time *in vivo*.

The interaction potential energy, U , as a function of the protein-surface separation distance, D , (which is directly related to the intersurface force, $U(D) = -\int F(D)dD$) initially determines whether or not a protein will be absorbed into a

surface and at what rate. $U(D)$ is a superposition of numerous nonspecific repulsive components (e.g., electrostatic counterion double layer, steric, hydration) and attractive components (e.g., van der Waals, hydrophobic, H-bonding, ionic) that can lead to complicated functional forms that vary with the strength and range of the constituent interactions.^{7,8,9,10} Secondary stages of protein adsorption depend on biomolecular adhesive binding processes that occur when a protein is in close contact with a surface, the conformation, orientation, and mobility of the adsorbed proteins, the timescale of conformational changes, protein exchange and desorption, and interactions of adsorbed proteins with each other.^{11,12} While the initial stage of the protein adsorption process is expected to be affected by a larger spatial-length scale of averaged surface properties and correlate with these properties, such as wettability, average surface charge per unit area, etc. the secondary stages, when the proteins move into close contact with the surface, are expected to be more dependent on local nanoscale variations and heterogeneities.

There has been considerable effort to design "bioinert" surfaces^{4,5,6,11,12} i.e., surfaces that exhibit zero interaction with the biological environment and hence, resist nonspecific protein adsorption, thereby exhibiting a high degree of biocompatibility. The use of molecules with a net electrical neutral charge (e.g., poly(ethylene oxide) (PEO) and tri-ethylene glycol (EG₃)) is thought to be advantageous.¹¹ Maximum hydrophilicity is one effective method of imparting repulsion, i.e., via molecules capable of strong hydrogen bonding with water creating an enthalpic penalty to dehydration and disrupting the supramolecular structure imposed by incoming protein molecules. It is suspected that the orientation, bonding strength and structure of interfacial water in such systems is critical.¹³ Electroneutrality and hydrophilicity alone

can not guarantee bioinertness, as proteins can clearly undergo hydrogen bonding, specific biomolecular adhesive events, and other short-range attractive interactions in the secondary stages of the adsorption process. One possible way to address this problem is to create well-defined local nanoscale variations in composition and chemical functionality to prevent the formation of spatial regions large enough to enable local binding events.¹⁴

Based on the concepts described above, some of the most effective systems for biomaterial-coating applications have been self-assembled monolayers (SAMs) * functionalized with a variety of end groups,^{11,12, 15} phospholipid polymers,^{16, 17} poly(ethylene glycol) (PEG),^{18,19,20,21} poly(ethylene oxide) (PEO),²² and PEO-based polymers.^{23,24}

Considering these effective systems, two kinds of hydrated organic thin films were selected for study in this research. The first one is an oligo(ethylene) self-assembling monolayers (OEO-SAMs)^{15,19,20,21} and the second one is phosphorylcholine (PC) lipid layers.²⁵

1.1.4 Structure and Properties of Oligo(ethylene oxide) Self-Assembling Monolayers (OEO-SAMs)

Oligo(ethylene oxide) OEO has been proposed as an excellent candidate for the creation of bioinert surfaces.^{15,19,20,21} OEO has a subunit, (EO)_n ([OCH₂CH₂]_n), which is also called (EG)_n (Figure 1-1²⁶) and this (EO)_n unit plays a key role in protein resistance.

* For further information, see the appendix.

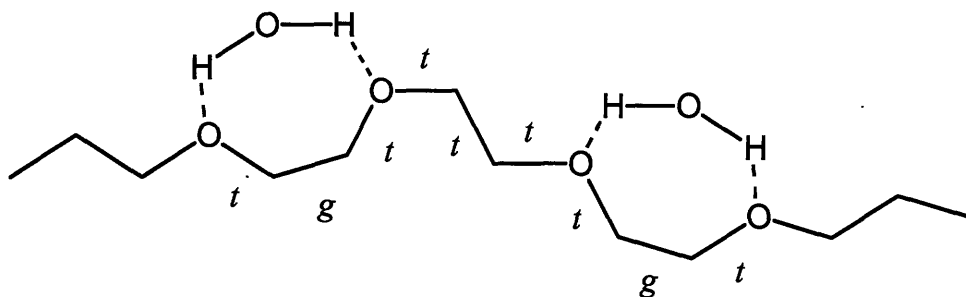


Figure 1-1 Possible confirmation of OEO in aqueous solution; OEO may take on a trans-trans-gauche (ttg) configuration where the ether oxygen atoms have hydrogen bonding.

In the initial study of OEO-SAMs²⁷ of OEO-SAMs, the protein resistance mechanism was explained by the steric repulsion of EO units that resisted the surface-attractive forces between the OEO-SAMs and the protein; the theory of steric repulsion is often used to explain the protein resistance of PEO.^{28,29} Its experiment using reflection-absorption infrared spectroscopy (RAIRS) and electrochemical impedance spectroscopy (EIS) shows that the helical or amorphous conformers of (EG)₃-SAMs on Au are protein resistant, but the *all-trans* conformers on Ag are not.²⁷ A recent study³⁰ of OEG-SAMs on both Au and Ag with varying numbers of EO subunits using X-ray photoelectron spectroscopy (XPS), infrared reflection absorption spectroscopy (IRRAS), and the ellipsometric technique, shows OEG-SAMs protein resistance on Au but not on Ag. This study was further investigated using *ab initio* calculations^{31, 32} that show that helical conformers of (EG)₃ on Au prefer to bind with water molecules more tightly than with the *all-trans* conformers on Ag because strong hydrogen bonds forms between the oxygen atoms on EG and the hydrogen atoms of the water molecules. Other recent molecular dynamics (MD) simulation studies also show the existence of hydrogen-bonded water layers.³³ The following study suggests that maximum hydrogen-bonded water layers are not created by the maximum density of PEO, which

can be made on the substrate but by the optimized density of PEO to maximize the hydrogen bonded water layers.³⁴ The less ordered, helical OEO-SAMs hold more water layers by hydrogen bonding than OH- and CH₃-terminated SAMs. These thicker water layers create a higher repulsive force under 2 nm distance when the protein (lysozyme) approaches the surface.³⁵

Recently, a study by Vanderah et al.³⁶ showed that less ordered SAMs of methyl 1-(3-mercaptopropyl) penta(ethylene oxide), (Au-S(CH₂)₃O (CH₂CH₂O)₅CH₃, (C₃EO₅)) (Figure 1-2 (a), (b)) with 60-80% surface coverage* (Figure 1-2³⁷ (c)) with controlled incubation time and a density of HS(CH₂)₃O(CH₂CH₂O)₅CH₃ is more protein resistant than highly ordered C₃EO₅-SAMs with 100% surface coverage and 7/2 helical conformation (approximately 2.11 nm in height)^{38,39} (Figure 1-2 (b), (d)). The protein adsorption at 60-80% coverage was 0 nm for bovine serum albumin and under 0.2 nm for fibrinogen, whereas at 100% coverage it was 0.5 nm and 2 nm respectively. This was explained by the increased flexibility of C₃EO₅-SAMs with a less ordered structure with a minimum length of C₃EO₅ covering the surface. This suggests that when the protein compresses the flexible C₃EO₅-SAMs with 60-80% surface coverage, the system's free energy (the free energy of surface layer + protein) increases and consequently induces the repulsive interaction (Figure 1-2 (c)). On the contrary, the fully ordered C₃EO₅-SAMs (7/2 helical conformation, 100% surface coverage) are too rigid to have free energy and repulsive forces (Figure 1-2 (d)).

* Here, the percentage of surface coverage is relatively predictable under the assumption that the 24 hr incubated surface coverage is 100%.

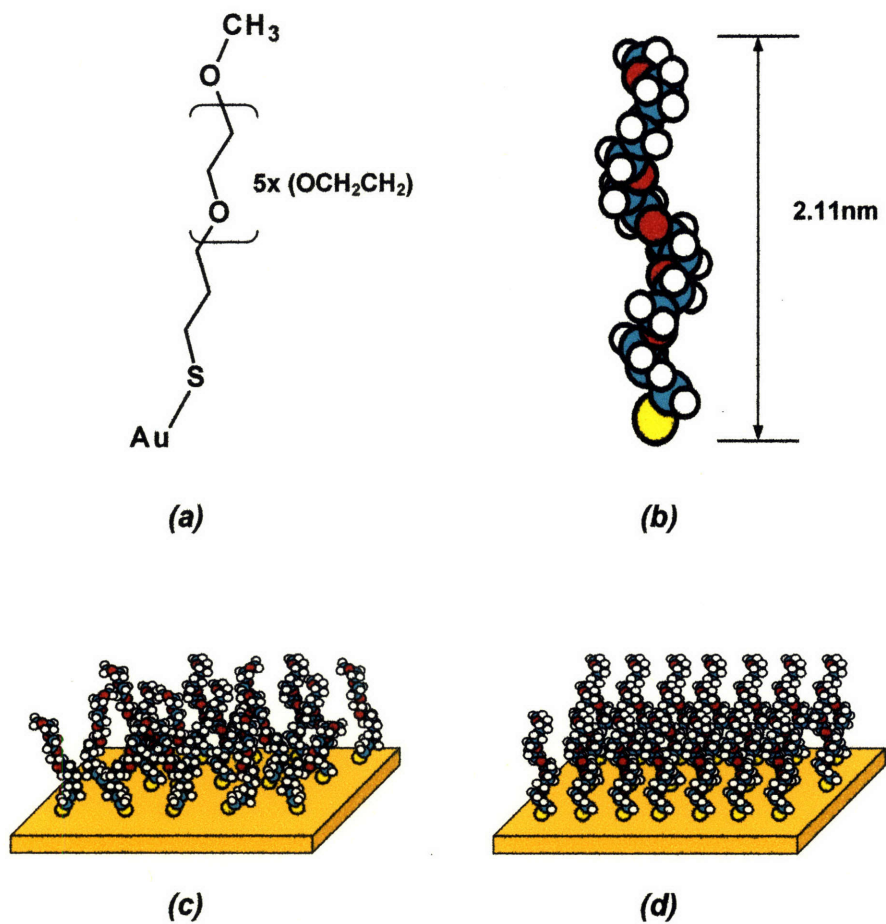


Figure 1-2. Chemical structure and self-assembled monolayers (SAMs) of C₃EO₅ on Au. (a) 2D all-trans form, (b) 3D 7/2 helical conformation, (c) 60-80% surface area coverage, (d) 100% coverage of surface.

To understand the molecular origin of this interaction mechanism, more detailed nanomechanical experiments than the surface plasma resonance (SPR) experiment are needed because SPR can only quantitatively explain how many proteins are attached to the targeted surface but cannot account for the detailed intermolecular interactions. In this current study, high resolution force spectroscopy (HRFS) is

performed on C₃EO₅-SAMs by approaching and retracting several types of chemically functionalized tips to understand the nanomechanical intermolecular force mechanism of this surface. Hydrophilic OH-terminated, hydrophobic CH₃-terminated, and negatively charged hydrophobic COOH-terminated tips were selected to represent one surface property due to their well-defined chemical functionality. A protein (human serum albumin)-functionalized tip was also selected to study the physiological interaction between protein and C₃EO₅-SAMs.

1.1.5 Structures and Properties of Phosphorylcholine (PC) Lipid Layers

The second model systems examined in this study is the polar zwitterionic phosphorylcholine (PC) lipid, which is the basic molecular unit of cell membranes. Among PCs, the 1-palmitoyl-2-oleoyl-sn-glycero-3-phosphocholine (POPC, unsaturated tail) and 1,2-dipalmitoyl-sn-glycero-3-phosphocholine (DPPC, saturated tail), were selected (Figure 1-3) because these two lipids provide a good comparison as they build a lipid bilayer in an aqueous environment during different phases at the same temperature (i.e., POPC is in a fluid phase and DPPC is in a gel phase in room temperature). The latter creates a stronger interaction between the lipids due to the strong hydrophobic interaction between saturated tails and because it is in a gel phase at room temperature. (The transition temperature from a gel to fluid is about 60°C.⁴⁰) In contrast, POPC is in a fluid phase at room temperature; the transition temperature to a fluid is -6°C.⁴¹

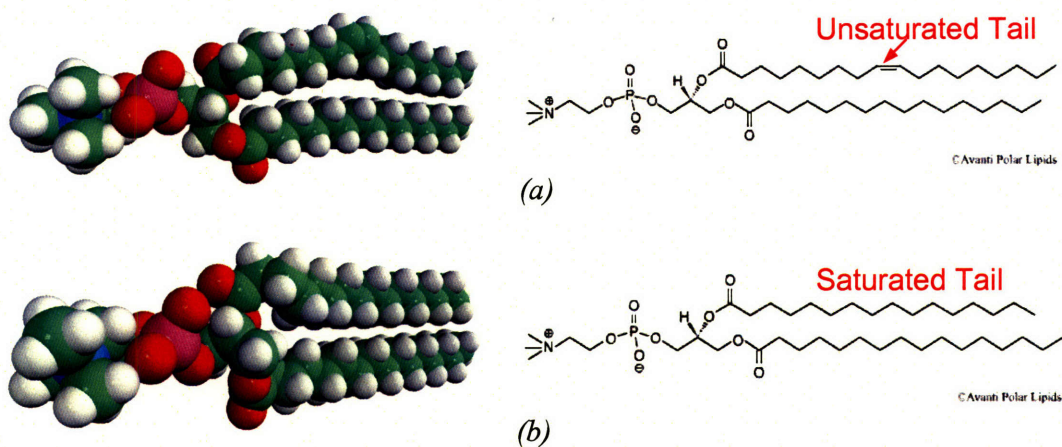


Figure 1-3. Chemical structure of phosphorylcholine (PC). (a) POPC, (b) DPPC, pictures by ©Avanti Polar Lipids.

These PCs form a planar bilayer on a hydrophilic surface such as mica (Figure 1-4) because PC is amphiphilic (the hydrophilic polar head group and hydrophobic tail group⁴²). PC can be deposited out to the substrate using several methods, such as the Langmuir Blodgett (LB) method⁴³ (Figure 1-5 (a)), the vesicle fusion technique⁴⁴ (Figure 1-5 (b)) and the direct deposit method.⁴⁵ In this research, the vesicle fusion technique is used for POPC (Ch. 3-4) and the direct deposit method is used for DPPC (Ch. 3-5).

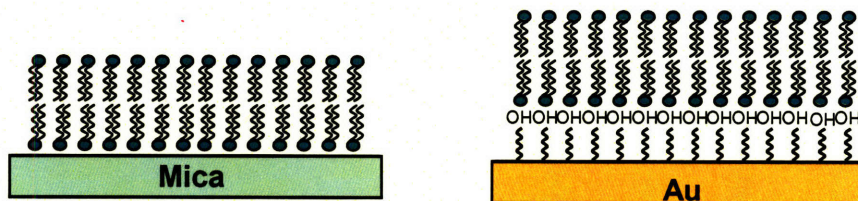


Figure 1-4. Lipid bilayers on the hydrophilic surface. (a) Lipid bilayers on mica, (b) Lipid bilayers on a hydrophilic OH-terminated SAM on bare Au; the hydrophilic head group of lipid is green dots and hydrophobic tail is two black chains.

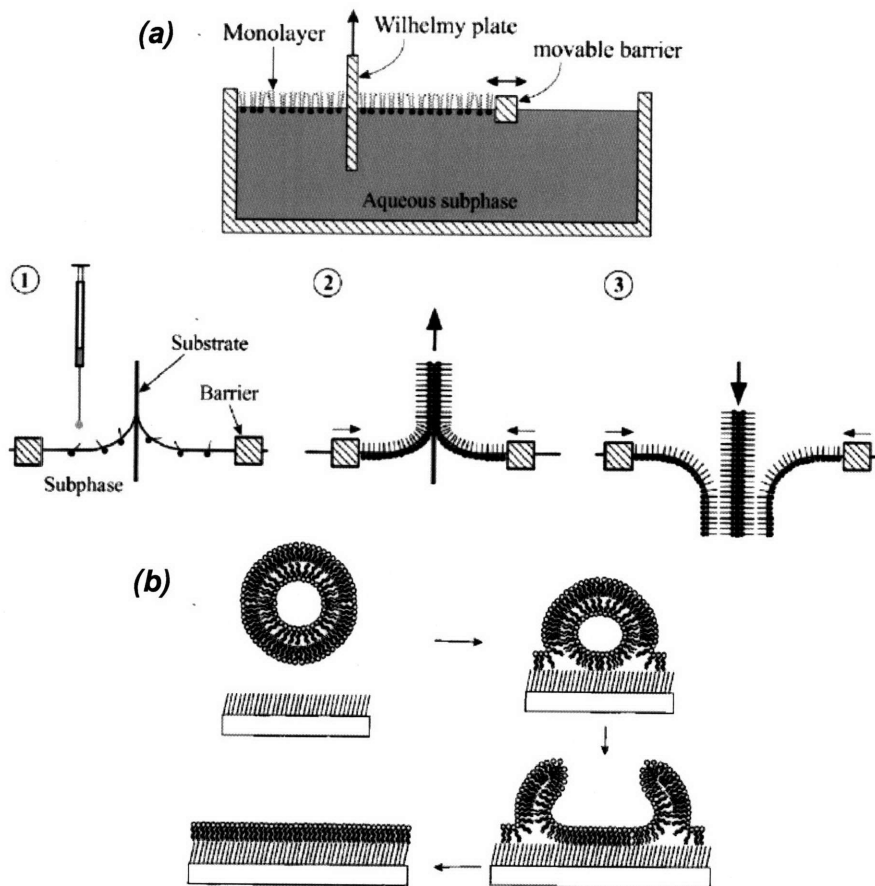


Figure 1-5 (a) three main steps in the Langmuir–Blodgett transfer of lipid monolayers from water onto a solid substrate.⁴³ (b) the vesicle fusion technique which is working on the lower diameter (under 100nm diameter) vesicle.⁴⁴

1.2 Nanomechanical Properties

1.2.1 Nanomechanical Experiments

In this research, nanomechanical forces based on distances are measured by using HRFS when the tip approach and retract from the surface; molecules can be functionalized on the tip or surface. These nanomechanical properties are associated with intermolecular and surface interactions in the (a) *noncontact interaction regime*: van der Waals (VDW), electrostatic, and hydrophobic forces, and in the (b) *contact*

interaction regime: steric, yielding, and fracture forces[†] of the hydrated thin film itself. Combined, these nanomechanical forces can result in a net repulsive or attractive force, depending on the distance between molecules and surfaces or a molecule and a surface. The nanomechanical properties can be illustrated by HRFS which is an outstanding tool to predict adsorption kinetics,^{46,47,48,49} evaluate and prescreen candidate biomaterials for which only extremely small quantities are available, and to assist in the chemical design of new hemocompatible biomaterials. In addition, HRFS combined with imaging can measure the molecular interaction force on the specially targeted area on the surface; this imaging of the targeted area also helps to evaluate the quality of the indented area.

HRFS experiments were performed in a near-physiological environment with a molecular force probe (MFP) by Asylum Research, Inc. (Santa Barbara, CA) (Figure 1-6) and PicoForce atomic force microscopy (AFM) by Veeco (Woodbury, NY) (Figure 1-7) to measure force, F (nN), vs. a probe tip-sample separation distance, D (nm). Both tools have a vertical force that measures the accuracy of piconewton scale. The PicoForce can perform good quality imaging and execute vertical, lateral and dynamic forces.

[†] Yielding and fracture force are classic mechanical properties in the macro-scale: the same concept is used for this nano-scale.

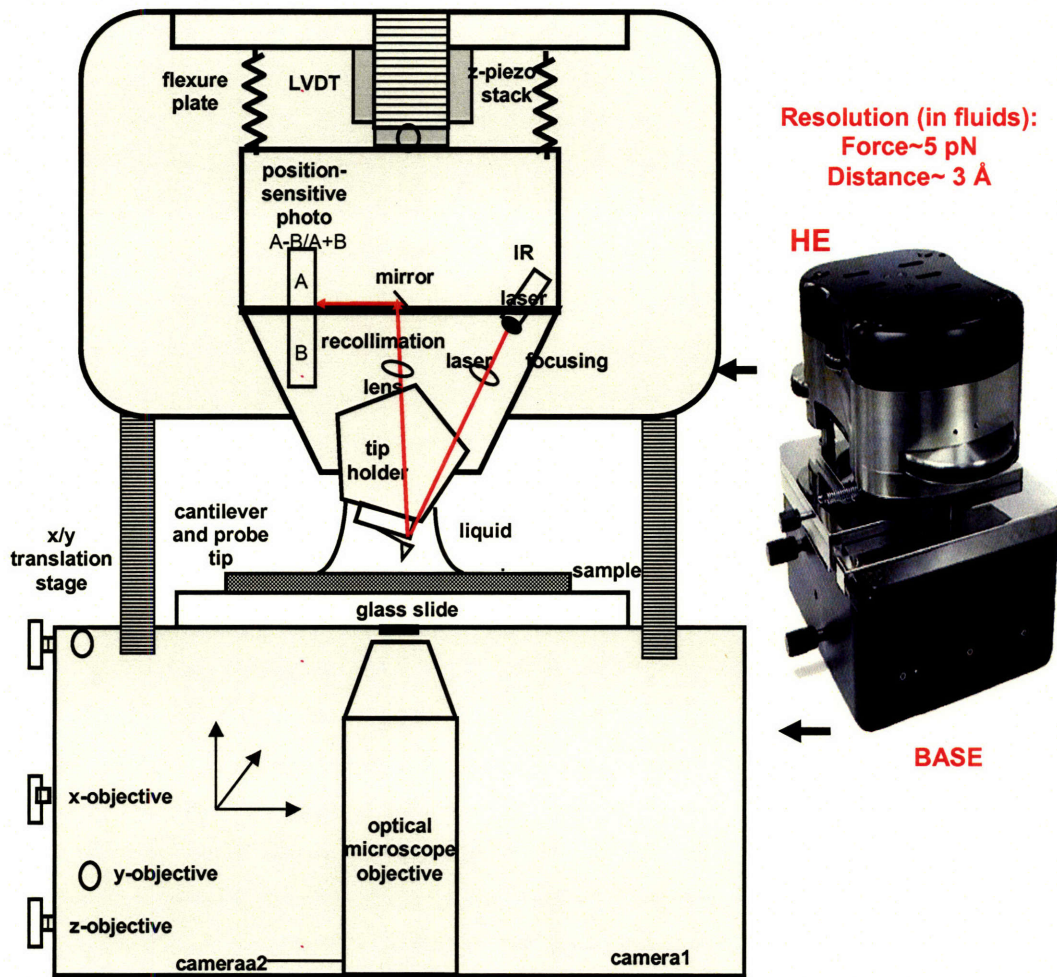


Figure 1-6. Molecular Force Probe (MFP) from Asylum Research.



Figure 1-7. PicoForce Atomic Force Microscopy (AFM) from Veeco.

1.2.2 Theoretical Approach

The basic theoretical approach to compare with HRFS experimental results for Force (F) with Separation Distance (D) is known as the Derjaguin- Landau-Verwey-Overbeek (DLVO) theory.^{50,51} According to the DLVO theory, the total interaction force is assumed to be linearly summed as follows (where force is a function of distance);

$$F_{tot}(D) = F_{VDW}(D) + F_{electr}(D) \quad (1)$$

$F_{VDW}(D)$ is an attractive van der Waals component and $F_{electr}(D)$ is a repulsive electrostatic component. $F_{VDW}(D)$ can be calculated by the “Derjaguin approximation” (valid for $R \gg D$)⁵² as shown an equation (2).

$$F_{VDW}(D) = -\frac{AR}{6D^2} \quad (2)$$

Here, R is assumed here to be same as the probe tip radius, R_{tip} , which can be measure by scanning electroscopic microscope (SEM).

$F_{electr}(D)$ can be modeled using constant surface charge approximation based on the numerical solution to the nonlinear Poisson-Boltzmann equation. The force is calculated from the electrostatic potential, Φ , using the free energy method.⁶² This long range (over 5 nm)[‡] numerical modeling is examined in Chapter 2 to estimate the

[‡] For the short range (under 5 nm), the DLVO theory could not be directly compared to HRFS data of this study because there would be more intermolecular forces not just the van der Waals force.

surface charge and the conformation of C₃EO₅. Once the tip penetrates the hydrated organic thin film, as shown in Chapter 3-5, the yielding and fracture mechanism should be considered because it will overcome the lateral confinement of the lipid layers. This will be discussed in Chapter 3-5.

1.3 Specific Aim and Nanomechanical Experiments

To better understand intermolecular forces, non-contact and contact nanomechanical properties such as electrostatic, steric, van der Waals and yielding forces are studied using HRFS with nano-scale imaging.

HRFS is performed with a molecular force probe (MFP) on the C₃EO₅-terminated SAM with various surface packing densities and different molecular conformations under 0.01 M, 0.1 M, and 1 M ionic strengths (IS). The main purpose of this research is to understand the type of nanomechanical intermolecular repulsive forces that are dominant in the long and short term between several types of functionalized tips and the C₃EO₅-terminated SAM. Another aim is to optimize protein resistance based on molecular conformation and surface packing density.

Atomic force microscopy (AFM) imaging and HRFS with high resolution pico-force AFM and MFP are performed using several different scale tips with lengths under 0.01 M, 0.1 M and .1 M ionic strengths (IS). Both tools are very helpful in understanding intermolecular forces, from long distance to contact, overlapping and penetrating distance between 'lipid monolayer and bilayer', 'lipid bilayer and bilayer',

to 'lipid bilayer to silicon nitride tip.** These experiments are key to the understanding the nanomechanical properties of the lipid membrane under pressure (for example, human arteries under high blood pressure, systolic: 15kPa, diastolic: 10kPa⁵³) and while interacting with proteins or cells with fusion, penetration, etc. HRFS on lipid bilayer is then performed using several tips with different tip-end radii and geometries because the effect of length scale and geometry on nanoscale surface interactions and the compressibility of supported lipid bilayers are not well understood.

From these nanomechanical experiments, the protein resistant mechanism of C₃EO₅-terminated SAM and the mechanical properties of PC layers are studied. This research will contribute to understand the protein resistance mechanism of hydrated organic thin films and help develop the bioinert surface coatings.

** The boundary condition of *in vivo* membranes are different from that of this experiment because the lipid layers in this research are supported by the rigid Au substrate or mica surface: the *in vivo* membrane is supported by the soft body of the cell.

CHAPTER 2

Molecular Origins of the Bioinert Properties of Methyl 1-(3-Mercaptopropyl) Penta(ethylene oxide) (C₃EO₅) Self-Assembled Monolayers (SAM).

2.1 Introduction

Oligo(ethylene oxide) OEO has been proposed as an excellent candidate to create bioinert surfaces; i.e., surfaces that resist nonspecific protein adsorption and exhibit a high degree of biocompatibility,^{15,19,20,21,27} for applications such as biosensors, biological implants, and marine antifouling coatings, among others.⁵⁴ OEO resists blood proteins⁵⁵ remarkably well, and may have better equilibrium prevention than PEO for long term use such as coating artificial arteries.⁵⁶ OEO has a subunit, (EO)_n ([OCH₂CH₂]_n), also called (EG)_n (Figure 1-3) and it plays a key role in protein resistance.

In the initial study of OEO-SAMs²⁷ of OEO-SAMs, the protein resistance mechanism was explained by the steric repulsion of EO units that resisted the surface-attractive forces between the OEO-SAMs and the protein; the theory of steric repulsion is often used to explain the protein resistance of PEO.^{28,29} This steric repulsion has been explained by the elastic compression of EO (or EG) units and the osmotic component caused by the loss of hydration. Its experiment by using reflection-absorption infrared spectroscopy (RAIRS) and Electrochemical impedance spectroscopy (EIS) shows that the helical or amorphous conformers of (EG)₃-SAMs on Au are protein resistant, but the *all-trans* conformers on Ag are not.²⁷ A recent study on OEG-SAMs on both Au and Ag with varying numbers of EO subunits using X-ray photoelectron spectroscopy

(XPS), infrared reflection-adsorption spectroscopy (IRRAS), and the ellipsometric technique shows protein resistance of OEG-SAMs on Au but not on Ag.⁵⁷ It suggests that protein resistance increases as the conformation becomes amorphous and less oriented and the surface-packing density decreases under 100% surface coverage of different OEO-SAMs.⁵⁷ From IRRAS experiments, it was found that OEO-SAM with EO₆ subunits has a crystalline helical conformation on Ag but is amorphous and has a less oriented conformation on Au. This study was further investigated using *ab initio* calculations^{31,32} that show that helical conformers of (EG)₃ on Au substrate tend to bind the water molecules more tightly than the *all-trans* conformers on Ag because strong hydrogen bonds form between the oxygen atoms on EG and the hydrogen atoms of the water molecules. Other recent molecular dynamics (MD) simulation studies also show the existence of hydrogen-bonded water layers.³³ This study suggests that maximum hydrogen bonded water layers are not made by the maximum density of PEO which can be made on the substrate but by the optimized density of PEO to maximize the hydrogen bonded water layers.³⁴

Another study using scanning force microscopy (SFM) suggests that the repulsive interaction between proteins and OEO-SAMs may be caused by the electrostatic interactions between the charged surface of proteins and the effective charge of OEO-SAMs that derive from the moment dipole of EO units.²¹ The continuing research of the quantum mechanical study and MD simulation for OEO and OEG in water supports its hypothesis²¹ that the dipole moment and polarizability of EO units in helical conformation^{58, 59, 60} are adequate enough to make the electrostatic interaction effective. In addition, several possible conformers with and without water molecules were recently studied by molecular dynamics (MD) simulation (Figure 2-1),

and show that the non-uniform gauche rotations are most stable in water.⁵⁸ The less ordered, helical OEO-SAMs were found to hold more water layers due to hydrogen bonding than OH- and CH₃-terminated SAMs. These The greater number of water layers create higher repulsive forces under 2 nm distance when the protein (lysozyme) approaches the surface.³⁵

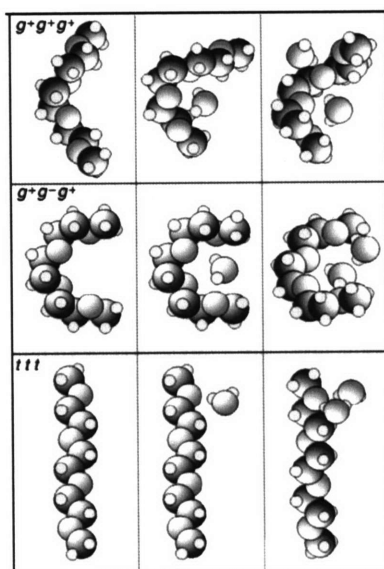


Figure 2-1 Several types of conformers of (EG)₃ without water molecules (left column), with one water molecule (center column), and with two water molecules⁵⁸.

Recently, a study by Vanderah et al.³⁶ showed that less ordered self-assembled monolayers (SAMs) of methyl 1-(3-Mercaptopropyl) Penta(ethylene oxide), (Au-S(CH₂)₃O (CH₂CH₂O)₅CH₃, (C₃EO₅)) with 60-80% surface coverage^{††} (Figure 2-2³⁷ (b)) with controlled incubation times and density of HS(CH₂)₃O (CH₂CH₂O)₅CH₃ is more protein resistant than the highly ordered C₃EO₅-SAMs with 100% surface coverage and 7/2 helical conformation (about 2.11 nm in height)^{38,39} (Figure 2-2 (a),

^{††} Here, the percentage of surface coverage is decided based on the assumption that the fully incubated surface coverage is 100%, achieved by controlling incubation time.

(c)). The protein adsorption at 60-80% coverage was 0 nm for bovine serum albumin and under 0.2 nm for fibrinogen whereas at 100% coverage it was 0.5 nm and 2 nm respectively. Vanderah et al. explained this was caused by the increased flexibility of C₃EO₅-SAMs of the less ordered structure with the minimum length of C₃EO₅ to cover the surface. This suggests that when the protein compresses the flexible C₃EO₅-SAMs with 60-80% surface coverage, the free energy of the system (the free energy of surface layer + protein) increases and it then induces the repulsive interaction (Figure 2-2 (b)). On the contrary, the fully ordered C₃EO₅-SAMs (7/2 helical conformation, 100% surface coverage) is too rigid to have repulsive forces (Figure 2-2 (c)).

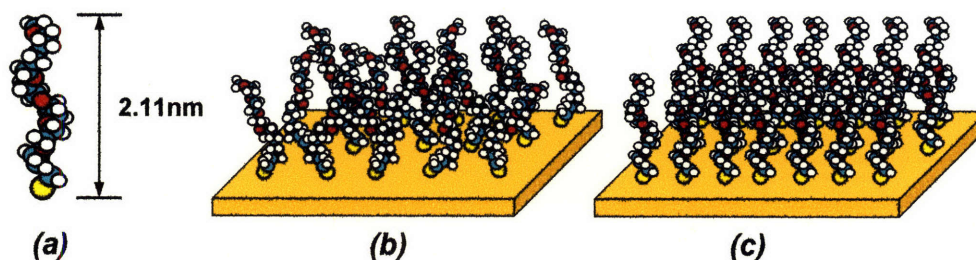


Figure 2-2 Self-assembled monolayers (SAMs) of C₃EO₅ on Au (a) 7/2 helical conformation, (b) 60~80% coverage of surface area, (c) 100% coverage of surface.

To understand the molecular origin of this interaction mechanism, nanomechanical experiments more detailed than the SPR experiment are needed because SPR can only quantitatively explain how many proteins are attached to the targeted surface and cannot explain the detailed intermolecular interactions. In this study, high resolution force spectroscopy (HRFS) is performed on C₃EO₅-SAMs by approaching and retracting several kinds of chemically functionalized tips in order to understand the nanomechanical intermolecular forces mechanism of this surface. Hydrophilic OH-terminated, hydrophobic CH₃-terminated, and negatively charged

hydrophobic COOH-terminated tips were selected due to their well-defined chemical functionality to represent one surface property. A protein (human serum albumin)-functionalized tip was also selected to study the physiological interaction between protein and C₃EO₅-SAMs.

Based on the results from these previous studies, a new hypothesis was formulated: the superior protein resistance of 60-80% surface-covered C₃EO₅-SAMs results from the repulsive interactions between the dipole moment of C₃EO₅-SAMs helical or amorphous conformers and the charged protein (*noncontact interaction regime*, long range), and the hydrogen bonded water layers on EO groups (*noncontact interaction regime*, short range). These EO groups are more exposed to the surface with 60-80% coverage than with 100% coverage, and the less ordered helical or amorphous C₃EO₅-SAMs (*contact interaction regime*) are more flexible than the ordered 7/2 helical conformation on 100% surface coverage.

2.2 Material Preparation

2.2.1 Materials

All the chemicals used in this study except C₃EO₅ were purchased from Sigma Aldrich Co. including 11-mercapto-1undecanol 97% (HS-(CH₂)₁₀-CO₂H, 44752-8), 11-mercaptoundecanoic acid (HS-(CH₂)₁₁-OH, 45056-1), 1-dodecanethiol (HS-(CH₂)₁₁-CH₃, 47135-4).

2.2.2 SAM Preparation

HS(CH₂)₃O(CH₂CH₂O)₅CH₃ solution (0.5 mM) was prepared using 95% ethanol solvent. C₃EO₅-SAMs were produced by incubating gold substrates in the solution at varying time increments to create a range of ethylene oxide coverage. To ensure a clean

surface, all gold substrates were Piranha treated (volume ratio, 1:3, H₂O₂:H₂SO₄) for under 5 minutes and then rinsed first by ethanol followed by DI water. The gold substrate was dried thoroughly by nitrogen. This process was performed immediately before functionalization.

The wettability was characterized by contact angle measurement, using a contact-angle goniometer (Rame' Hart, Inc., Mountain Lakes, NJ). Advancing, static, and receding angles were recorded for the gold substrates incubated in C₃EO₅ -SAMs for 5 seconds, 3, 6, 24, 27, 30 hours, and 3 days. The gold substrate was dipped in and out of HS(CH₂)₃O(CH₂CH₂O)₅CH₃ solution (0.5 mM) for 5 seconds for incubation and the gold surface was rinsed first with ethanol and then pure deionized water. Between 1-5 seconds, there was no statistically significant difference in the contact angle. In addition, Vanderah et al.'s previous study showed a consistent molecular-level structure and arrangement during a short time scale: 5 seconds to 30 minutes.

A 5 second incubation produced a sample of the less ordered structure (60-80% surface coverage) and 24 hours incubation produced the fully ordered structure (100% surface coverage). These incubation times were chosen in order to replicate the surface packing densities of Vanderah et al.'s.³⁶ A 3 days incubation was carried out to discover if a difference would result between 24 hours and 3 days incubation.

2.2.3 Choices and Preparation of Functionalized Tips

As mentioned in the introduction, hydrophilic OH-terminated, hydrophobic CH₃-terminated, and negatively charged hydrophobic COOH-terminated and protein-functionalized tips were selected to better understand the mechanism of nanomechanical intermolecular forces of C₃EO₅-SAMs.

Using 0.0255 g of 11-mercapto-undecanol, 30 μL of 1-dodecanethiol and 0.023 g of mercapto-1 undecanol in ethanol, 25 mL of 5 mM OH, CH₃, and COOH solutions were prepared. Gold-coated Digital Instruments 0.06 N/m (Santa Barbara, CA) cantilever tips were CH₃-, OH-, and COOH- terminated by incubating them in 1-dodecanethiol, poly(2-hydroxyethyl)methacrylate, and 11-mercaptoundecanoic acid solutions for 24 hours. To ensure a clean surface, all tips, as well as the gold substrates, were Piranha treated (1:3 H₂O₂:H₂SO₄) for 5 minutes immediately before functionalization. Protein (Human Serum Albumin)-functionalized tips were purchased from Novascan (spring constant, 0.06 N/m).

2.2.4 Choices of Ionic Strengths

Three different ionic strengths (IS) 0.01 M, 0.1 M and 1 M of 10 mM tris (hydroxymethyl) aminomethane buffer with NaCl (pH 7.8) were selected. Out of these three ISs, 0.1 M and 1 M IS were selected because they provide a similar IS condition to blood (0.15 M) and seawater (about 0.7 M⁶¹). Other multivalent ions exist in the blood stream and in seawater, but because Na⁺ and Cl⁻ are the main ions in both, they were selected to simplify the experimental environment.

2.3 Experimental Method

Force vs. distance measurements for both approach and retract were taken in fluid using 1-D Molecular Force Probe (MFP) (Asylum Research, Inc). It is important to measure not only force vs. distance when the tip approaches the C₃EO₅-SAM surface but also when the tip retracts from the C₃EO₅-SAM surface. This is because *in vivo*, proteins in blood can contact the surface under high blood pressure; in the U.S. standard

blood pressure on systolic is less than 120 mmHg (2.32 psi or 15 kPa)^{62,63} which can be over 140 mmHg with risky hypertension⁶⁴. Data was recorded for C₃EO₅-SAMs that were incubated at 5 seconds, 24 hours, and 3 days versus a protein-functionalized, OH-, CH₃-, COOH- and C₃EO₅-terminated SAM tips in Tris buffer (titrated to pH 7.8) as a function of ionic strength (IS = 0.01 M, 0.1 M and 1 M). The ionic strength was adjusted by adding NaCl. At least 30 curves were recorded over a minimum of three locations on each sample. All experiments were performed at room temperature. The bin size of the histogram was decided from the Sturges' rule.⁶⁵

2.4 Experimental Results

2.4.1 Contact Angle Measurement

Contact angle measurements clearly show the formation of SAMs at all incubation times and the conformational change of C₃EO₅ molecules (Figure 2-3). Compared to the hydrophobic Au substrate, 5 seconds incubated C₃EO₅ is hydrophilic and clearly shows the formation of C₃EO₅-SAMs. As SAMs reach a molecular equilibrium state after 6 hours, they become relatively hydrophobic (advanced contact angles are all near 70°) compared to the 5 seconds advancing contact angle $57.04 \pm 0.46^\circ$. Between 1 second and 5 seconds of incubation time resulted in no significant differences in contact angles.

2.4.2 Hydrophilic OH-Terminated Probe Tip vs C₃EO₅ SAM Planar Surface

Figure 2-4 shows the average HRFS of force- versus distance-curves on approach and retract states for C₃EO₅-SAMs prepared with three incubation times; 5 s (60-80% surface coverage), 24 hr (100% surface coverage), and 3 days (longer

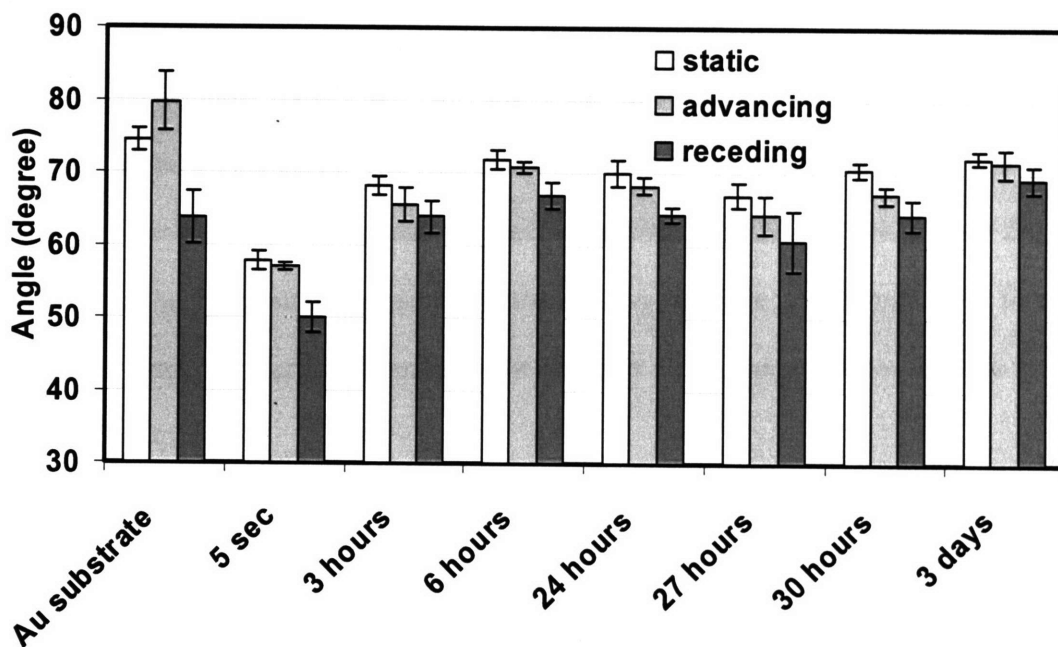


Figure 2-3. Static-, advancing- and receding-deionized water-contact angle measurement of unfunctionalized Au substrate and C_3EO_5 self-assembling monolayer from 95% ethanol solution (0.5 mM) at room temperature 25°C. Each bar represents the mean of 4 locations on one sample. The Hi-Lo bars show the standard deviation. The difference of contact angle between Au (0% surface coverage) and 5 seconds (60-80% coverage) or 5 seconds (60-80% coverage) and 3 hours (near to 100%) is statistically significant.

incubation time than that of 100% surface coverage) using a single hydrophilic OH-terminated SAM probe tip. For the low surface coverage samples (5 s incubation time, Fig. 2-4 (a), (b)), a purely repulsive monotonic interaction was observed on both approach and retract curves in which the range was approximately 10 nm with minimal hysteresis. A jump-to-contact (tip jump to the surface of the C_3EO_5 -SAM layer), or a breakthrough to the underlying substrate was not observed. For the full surface coverage samples (24 hr incubation time, Fig. 2-4 (c), (d)), the approach curves have less repulsive (0.01 M IS) and attractive (0.1 M, 1 M ISs) forces compared to the 5 s incubation time (Figure 2-4 (c)). The retract curve shows higher adhesive forces as the IS increases (Figure 2-4 (d)). For the C_3EO_5 -SAM of 3 days incubation (over 100% of

the ordered sample), both approach and retract curves show adhesive forces at 0.1 M and 1 M ISs (Figure 2-4 (e), (f)). As incubation time increases, the pull-off distance increases in the retract curve. The pull-off distances of 1 M IS 24 hr and 3 days on the retract curves are over 10 nm and the forces are over 0.2 nN ~ 1 nN (Figure 2-5). Overall, as the ionic strength increases, the starting distance of the repulsive force decreases. Here, the starting distance is the distance where the repulsive force is first observed on approach.

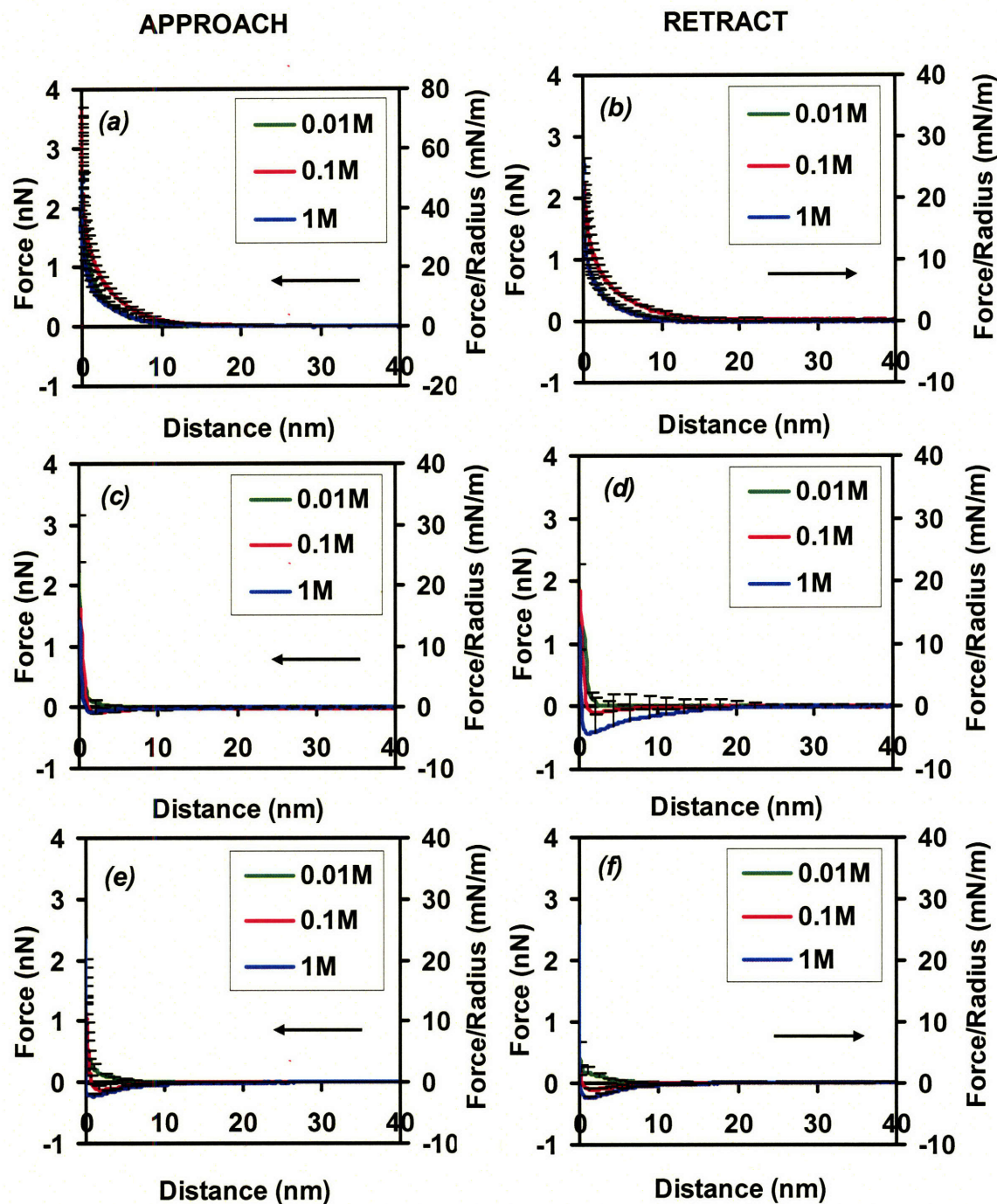


Figure 2-4. Nanomechanical data for OH-terminated self-assembling monolayer (SAM)-coated cantilever tip vs C_3EO_5 SAMs on flat Au as a function of incubation time in the C_3EO_5 solution (95% ethanol, 0.5 mM) and ionic strength of the aqueous media during the approach and retract. Graphs (a), (c), and (e) are the approach curves for incubation times of 5 seconds, 24 hours, and 3 days, respectively. Graphs (b), (d), and (f) are the corresponding retract curves. A Veeco Au-coated Digital Instruments cantilever tip was used (spring constant: 0.06 N/m, probe tip end radius: 100 nm, displacement rate = $1\mu\text{m}/\text{sec}$). All experiments were carried out with a single probe tip.

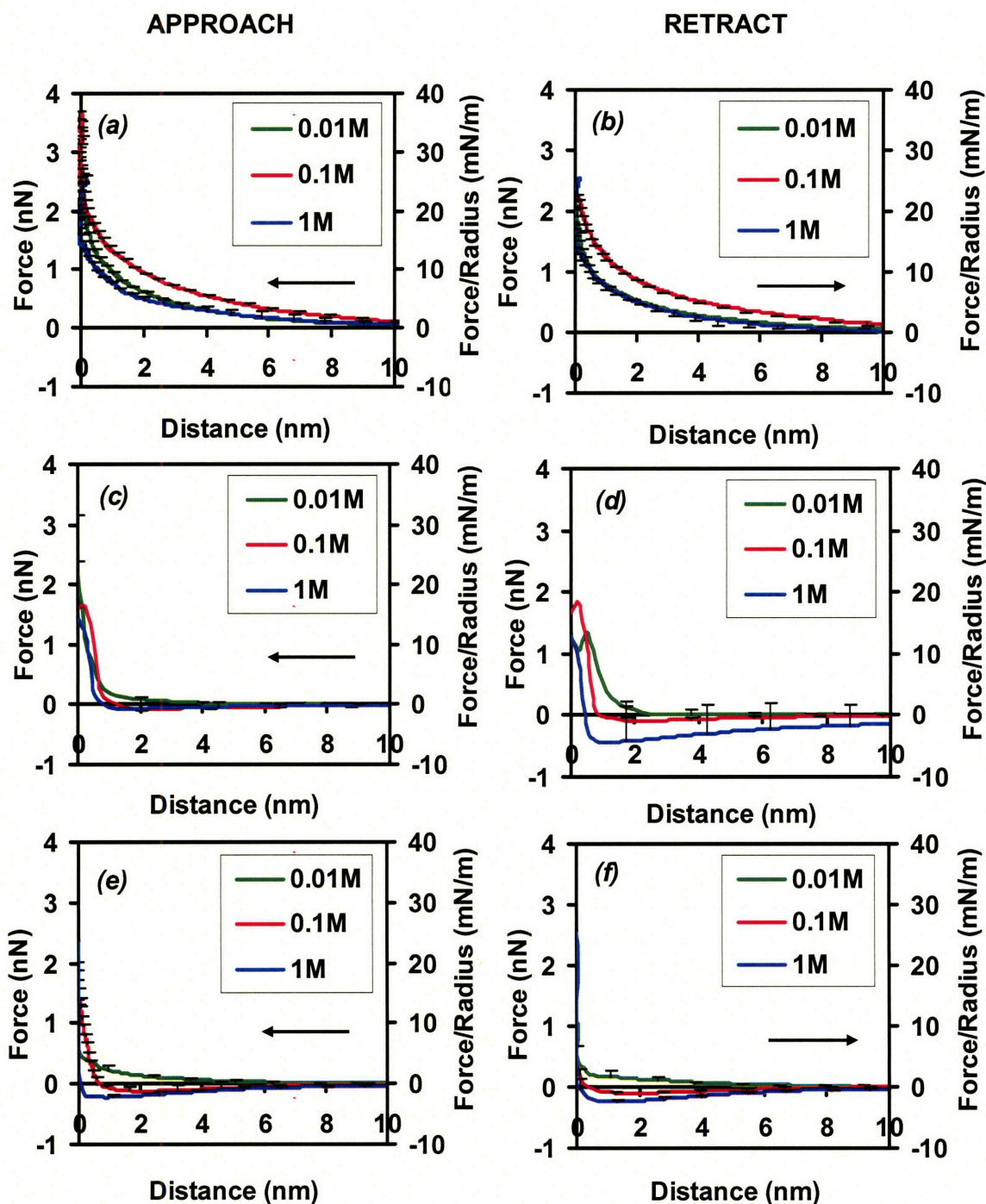


Figure 2-4A (Magnified from Figure 2-4). Nanomechanical data for OH-terminated self assembling monolayer (SAM)-coated cantilever tip vs C_3EO_5 SAMs on flat Au as a function of incubation time in the C_3EO_5 solution (95% ethanol, 0.5 mM) and ionic strength of the aqueous media during approach and retract. Graphs (a), (c), and (e) are the approach curves for incubation times of 5 seconds, 24 hours, and 3 days, respectively. Graphs (b), (d), and (f) are the corresponding retract curves. A *Veeco* Au-coated Digital Instruments cantilever tip was used (spring constant: 0.06 N/m, probe tip end radius: 100 nm, displacement rate = $1\mu\text{m}/\text{sec}$). All experiments were carried out with a single probe tip.

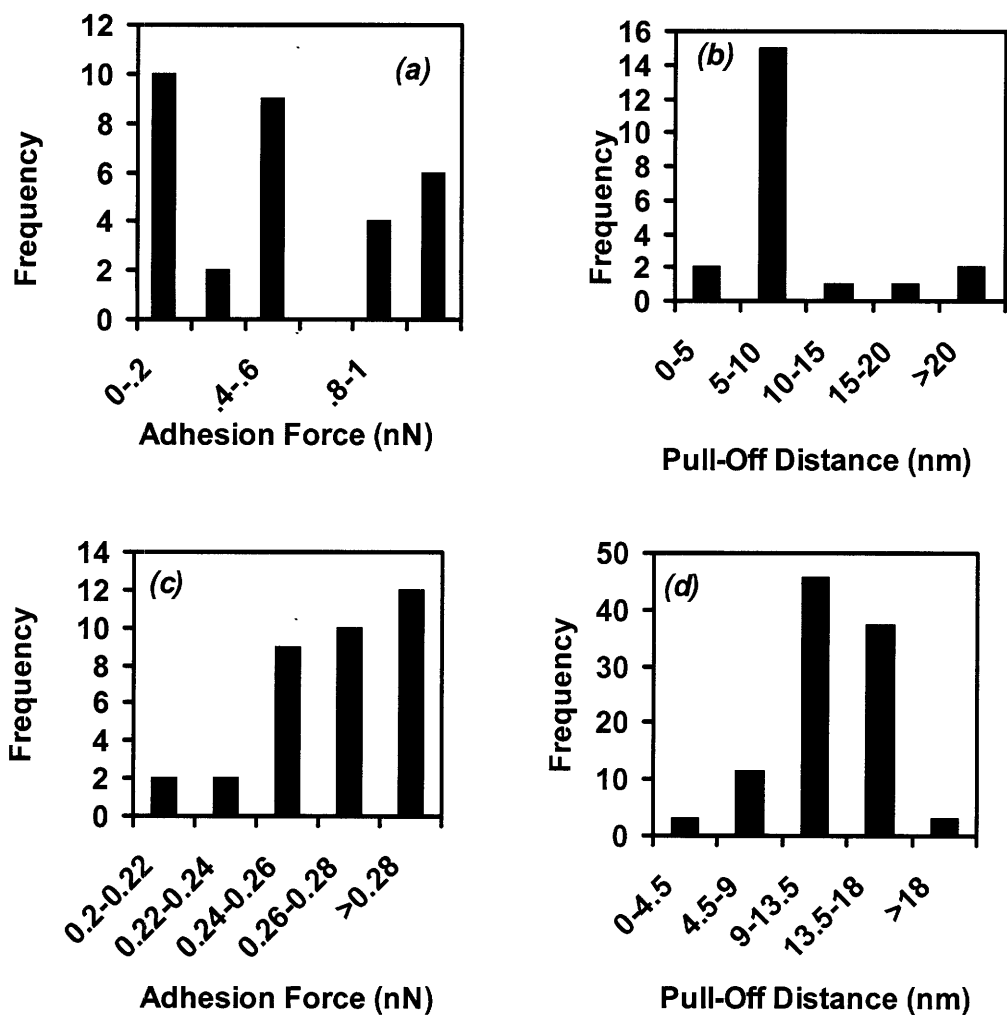


Figure 2-5. (a) Adhesion force and (b) pull-off frequency histogram plots of the retract curves for the OH-terminated self-assembling monolayer (SAM)-coated cantilever tip vs C_3EO_5 SAMs on flat Au (incubation time = 24 hr; 1M ionic strength); (c) and (d) are analogous plots of retract curves for C_3EO_5 SAMs (incubation time = 3 days; 1 M ionic strength).

2.4.3 Hydrophobic CH₃-Terminated Probe Tip vs C₃EO₅ SAM Planar Surface

Both approach and retract curves from the C₃EO₅-SAM versus the hydrophobic CH₃-terminated SAM tip show similar trends for ionic strength and incubation time as the OH-SAM tip versus the C₃EO₅-SAM (Figure 2-4 & 2-6). Compared to curves of the OH-terminated SAM tip versus the C₃EO₅-SAM, the repulsive force is less at the same incubation times and IS conditions (Figure 2-4 & 2-6). A jump-to-contact was observed on all approach curves except for that of the low-surface coverage sample (60-80%).

2.4.4 Hydrophilic and Negatively Charged COOH-Terminated Tip vs C₃EO₅ SAM Planar Surface

Under the prepared 10 mM tris buffer solution as described in the experimental method, the carboxylic acid group is ionized and negatively charged. The pKa is expected to be 6.4 at 0.013 M IS,⁶⁶ 5.7 ± 0.2 at 0.10 M IS and 4.4 ± 0.2 at 1.0 M IS.⁶⁷ This is due to the fact that interfacial potentials at the monolayer surface, such as the diffuse double-layer potential, decrease as the IS of the solution increases.^{††66} As for the CH₃-terminated SAM tip or the OH-terminated SAM tip vs the C₃EO₅-SAM, all approach curves for the negatively charged COOH-terminated tip vs C₃EO₅-SAM show a repulsive force, while the retract curves show more adhesive force as the incubation time increases. The results show that the 5 s incubated C₃EO₅-SAM has a repulsive interaction with the hydrophilic and negatively charged COOH-terminated SAM (negatively charged in this Tris buffer solution such as COO⁻). One noticeable difference in this experiment using OH and CH₃-terminated SAM tip is that, for the full-surface coverage samples (24 hr incubation time), the repulsive force on approach at 1

†† It means that the coulombic attraction between the hydrogen cations in the solution and the carboxylate anions on the surface decreases as the IS decreases. Therefore the moiety of the carboxylic acid becomes a stronger acid when the IS of the solution increases.

M IS is higher than others on 0.01 M and 0.1 M ISs, while that of the repulsive force at 0.01 M and 0.1 M ISs is comparable (Figure 2-8).

2.4.5 C₃EO₅-SAM probe tip versus C₃EO₅-SAM planar surface

For the above two experiments using hydrophilic (OH-terminated) and hydrophobic (CH₃-terminated) tips, the adhesion forces on the retract curves increase with increased incubation time. On the contrary, the HRFS graph on retract for C₃EO₅-SAM vs C₃EO₅-SAM tip shows that the minor nanoscale adhesive force (<-0.3 nN) is higher in the 5 seconds-incubated sample than the others (Figure 2-9 (b), (d), and (f)). However, all approach curves consistently show the repulsive forces (Figure 2-9 (a), (c) & (e)).

2.4.6 Protein (HSA) Functionalized Tip vs C₃EO₅-SAM

The result of the protein-functionalized tip vs the 5 s incubated C₃EO₅-SAM clearly shows the repulsive protein interaction on all approach and retract curves (Figure 2-10 (a) and (b)). At 0.01 M IS of the 5 s incubated C₃EO₅-SAM, long range repulsive forces are observed. As incubation time and IS increase, the adhesion forces rapidly increase. For the 3 days incubated C₃EO₅-SAM, the long range of the pull-off distances from over 40 nm to 160 nm during the retract stage suggest mechanical denaturation of proteins caused by the attractive force between proteins and C₃EO₅-SAM (Figure 2-10 (f)). The interaction forces between the HSA functionalized tip vs the mica, COOH-terminated SAM, CH₃-terminated SAM, and OH-terminated SAM all show adhesive forces during the retract stage (Figure 2-11). Among these interactions, the negatively charged COOH-terminated SAM vs the HSA functionalized tip is less adhesive during retract and more repulsive on approach (Figure 2-11).

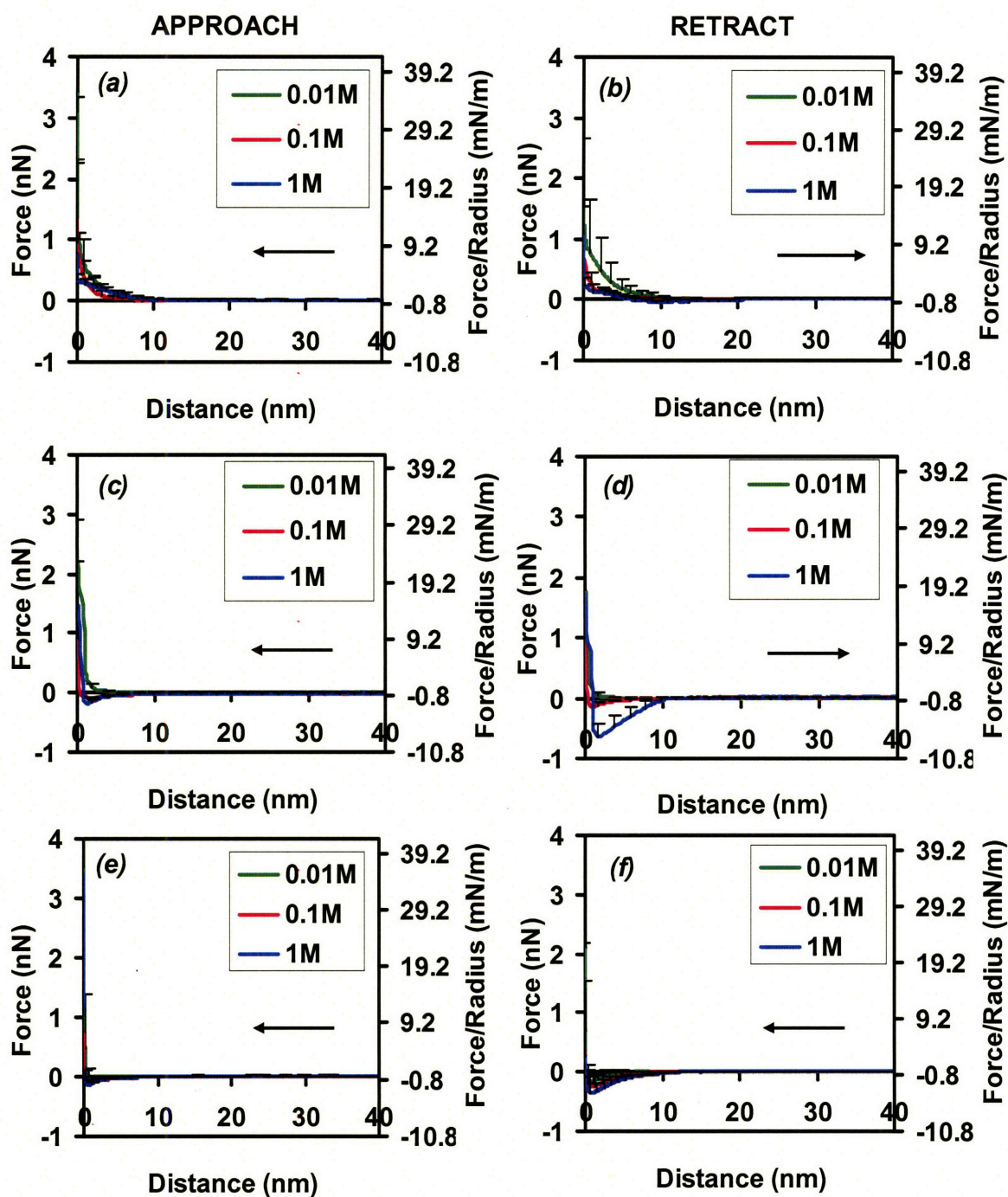


Figure 2-6. Nanomechanical data for CH_3 -terminated self assembling monolayer (SAM)-coated cantilever tip vs C_3EO_5 SAMs on flat Au as a function of incubation time in the C_3EO_5 solution (95% ethanol, 0.5 mM) and the ionic strength of the aqueous media during approach and retract. Graphs (a), (c), and (e) are the approach curves for incubation times of 5 seconds, 24 hours, and 3 days, respectively. Graphs (b), (d), and (f) are the corresponding retract curves. A Veeco Au-coated Digital Instruments cantilever tip was used (spring constant: 0.06 N/m, probe tip end radius: 96 nm, displacement rate = $1\mu\text{m}/\text{sec}$). All experiments were carried out with a single probe tip.

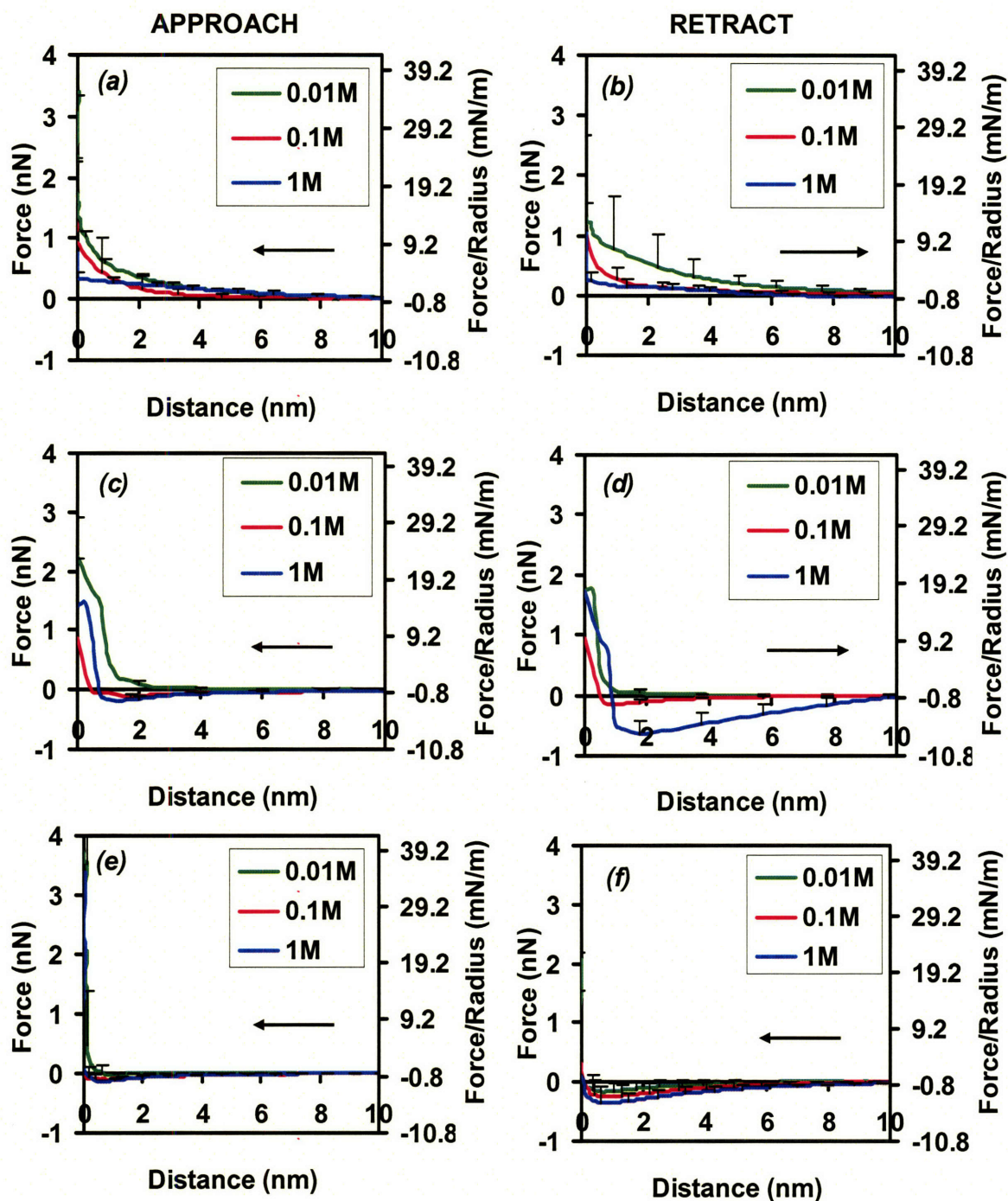


Figure 2-6A (Magnified from Figure 2-6). Nanomechanical data for CH₃-terminated self assembling monolayer (SAM)-coated cantilever tip vs C₃EO₅ SAMs on on flat Au as a function of incubation time in the C₃EO₅ solution (95% ethanol, 0.5 mM) and ionic strength of the aqueous media during approach and retract. Graphs (a), (c), and (e) are the approach curves for incubation times of 5 seconds, 24 hours, and 3 days, respectively. Graphs (b), (d), and (f) are the corresponding retract curves. A *Veeco* Au-coated Digital Instruments cantilever tip was used (spring constant: 0.06 N/m, probe tip end radius: 100 nm, displacement rate = 1 μ m/sec). All experiments were carried out with a single probe tip.

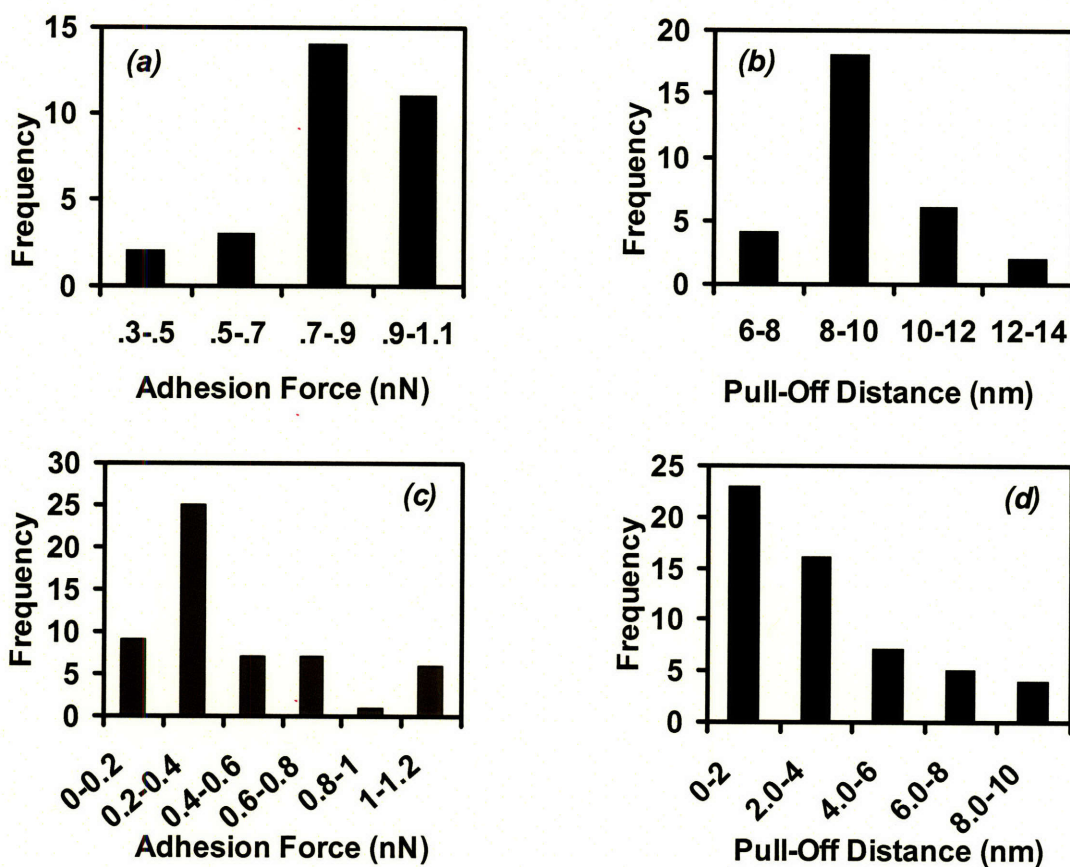


Figure 2-7. (a) Adhesion force and (b) pull off frequency histogram plots of retract curves for the CH₃-terminated self assembling monolayer (SAM)-coated cantilever tip vs C₃EO₅ SAMs on flat Au (incubation time = 24 hr; 1 M ionic strength). (c) and (d) Analogous plots of retract curves for C₃EO₅ SAMs (incubation time = 3 days; 1 M ionic strength). There appears to be a regular distribution similar to that found in Figure 2-5.

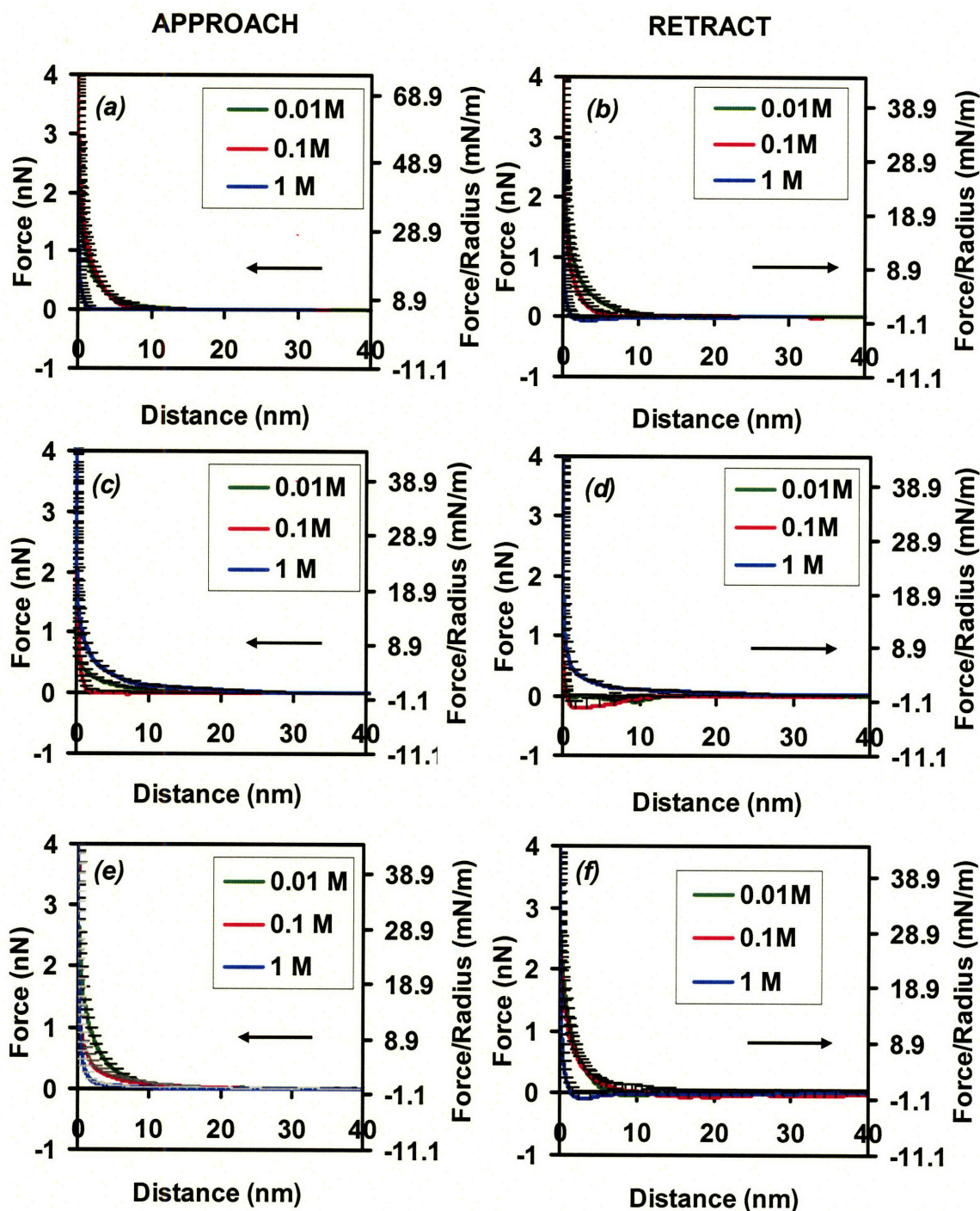


Figure 2-8. Nanomechanical data for COOH-terminated self assembling monolayer (SAM)-coated cantilever tip vs C_3EO_5 SAMs on flat Au as a function of incubation time in the C_3EO_5 solution (95 approach and retract. % ethanol, 0.5 mM) and ionic strength of the aqueous media during Graphs (a), (c), and (e) are the approach curves for incubation times of 5 seconds, 24 hours, and 3 days, respectively. Graphs (b), (d), and (f) are the corresponding retract curves. A Veeco Au-coated Digital Instruments cantilever tip was used (spring constant: 0.06 N/m, probe tip end radius: 100 nm, displacement rate = $1\mu\text{m}/\text{sec}$). All experiments were carried out with a single probe tip.

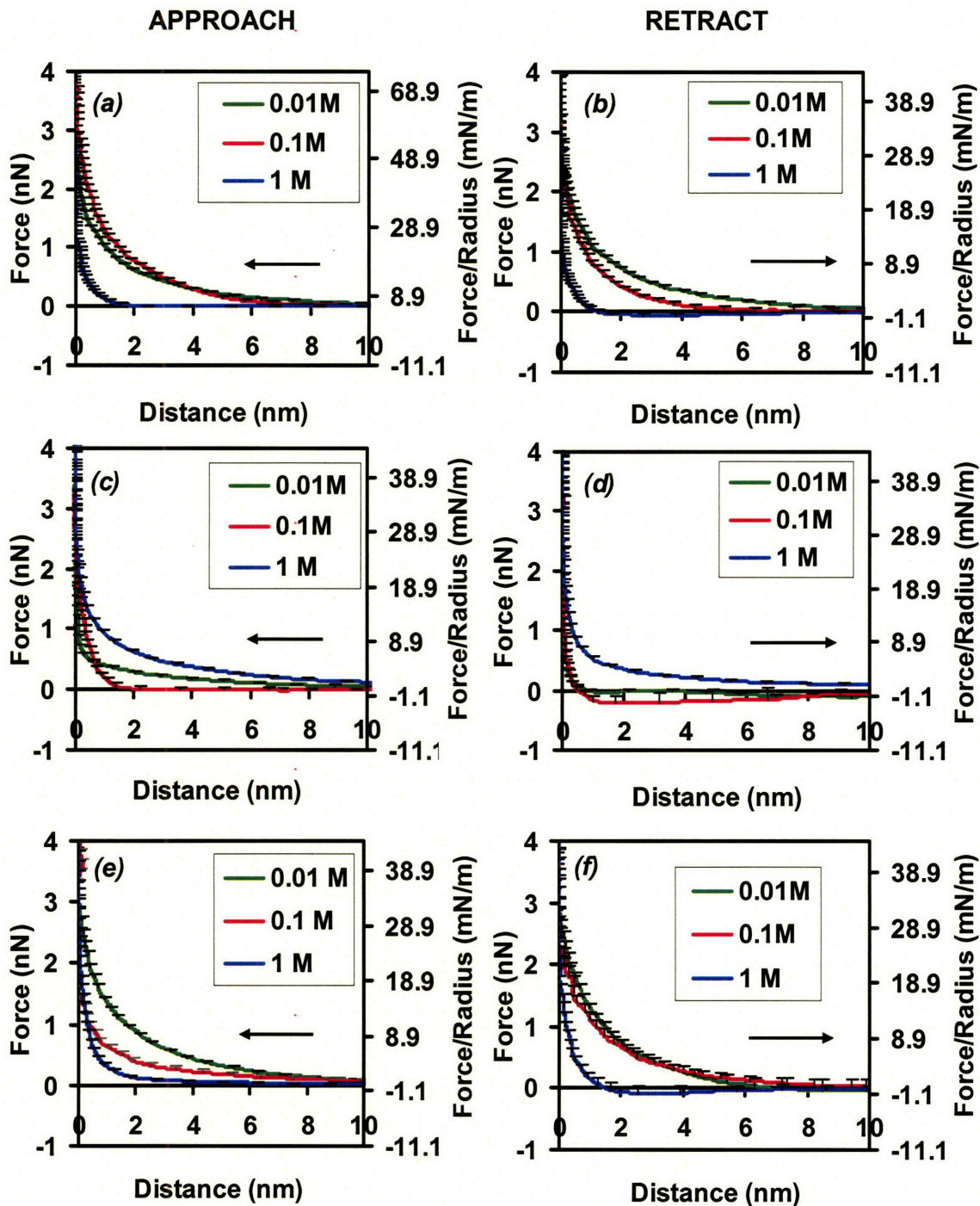


Figure 2-8A (magnified from Figure 2-8). Nanomechanical data for COOH-terminated self assembling monolayer (SAM)-coated cantilever tip vs C_3EO_5 SAMs on on flat Au as a function of incubation time in the C_3EO_5 solution (95% ethanol, 0.5 mM) and ionic strength of the aqueous media during approach and retract. Graphs (a), (c), and (e) are the approach curves for incubation times of 5 seconds, 24 hours, and 3 days, respectively. Graphs (b), (d), and (f) are the corresponding retract curves. A *Veeco* Au-coated Digital Instruments cantilever tip was used (spring constant: 0.06 N/m, probe tip end radius: 100 nm, displacement rate = $1\mu\text{m}/\text{sec}$). All experiments were carried out with a single probe tip.

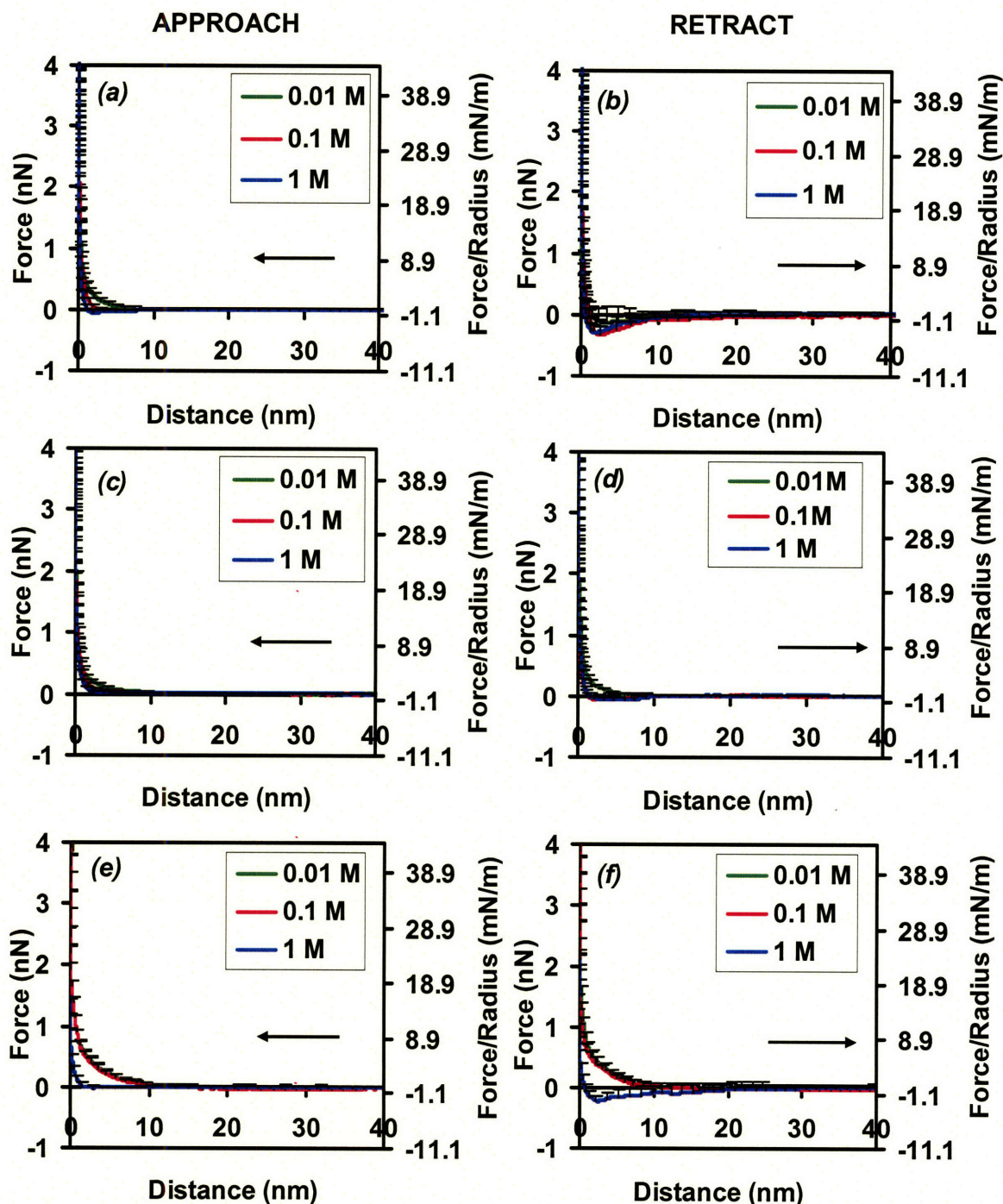


Figure 2-9. Nanomechanical data for C_3EO_5 -terminated self assembling monolayer (SAM)-coated cantilever tip vs C_3EO_5 SAMs on on flat Au as a function of incubation time in the C_3EO_5 solution (95% ethanol, 0.5 mM) and ionic strength of the aqueous media during approach and retract. Graphs (a), (c), and (e) are the approach curves for incubation times of 5 seconds, 24 hours, and 3 days, respectively. Graphs (b), (d), and (f) are the corresponding retract curves. A *Veeco* Au-coated Digital Instruments cantilever tip was used (spring constant: 0.06 N/m, probe tip end radius: 100 nm, displacement rate = $1\mu\text{m}/\text{sec}$). All experiments were carried out with a single probe tip.

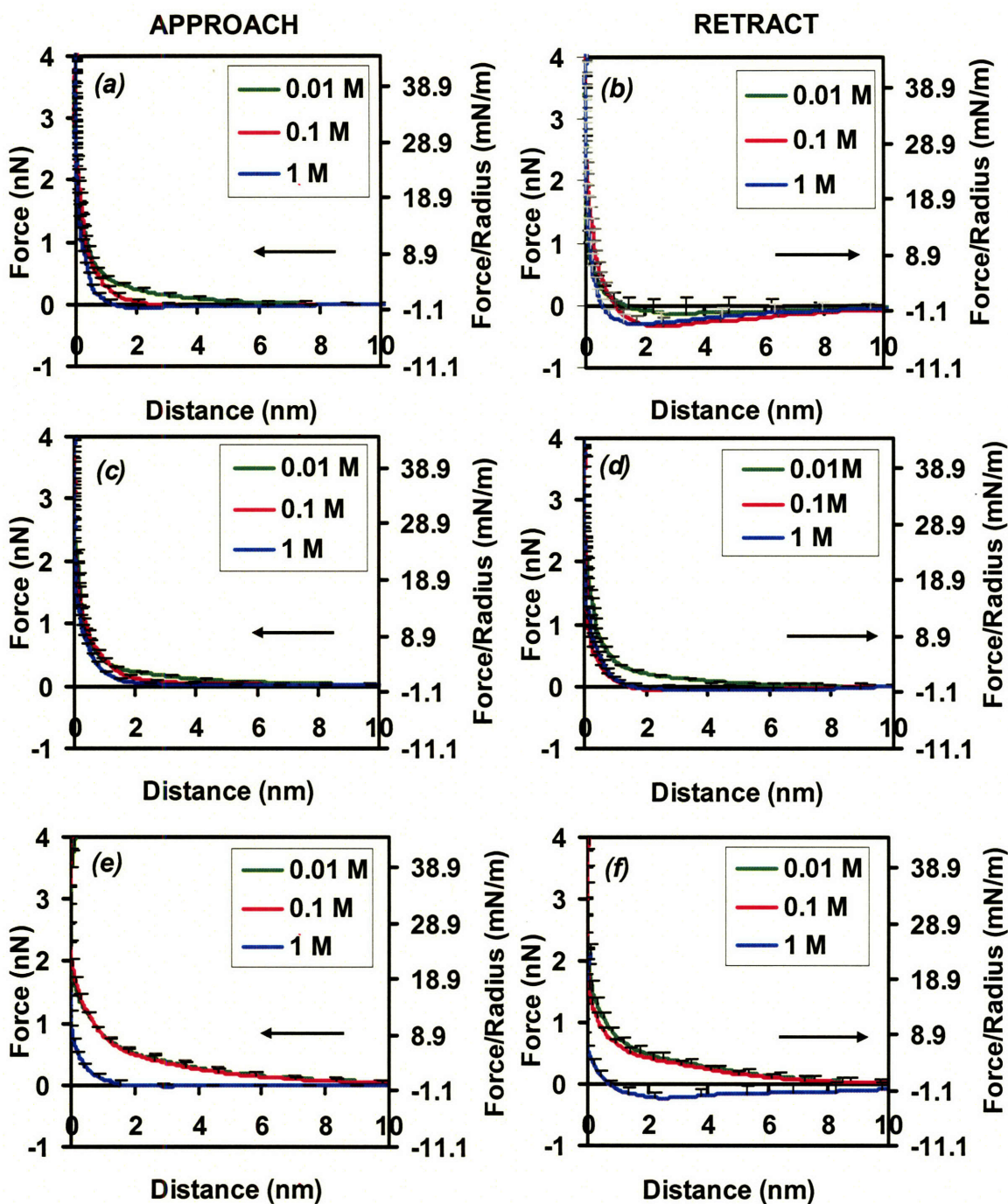


Figure 2-9A (magnified from 2-9). Nanomechanical data for C_3EO_5 -terminated self assembling monolayer (SAM)-coated cantilever tip vs C_3EO_5 SAMs on flat Au as a function of incubation time in the C_3EO_5 solution (95% ethanol, 0.5 mM) and ionic strength of the aqueous media during approach and retract. Graphs (a), (c), and (e) are the approach curves for incubation times of 5 seconds, 24 hours, and 3 days, respectively. Graphs (b), (d), and (f) are the corresponding retract curves. A *Veeco* Au-coated Digital Instruments cantilever tip was used (spring constant: 0.06 N/m, probe tip end radius: 100 nm, displacement rate = $1\mu\text{m}/\text{sec}$). All experiments were carried out with a single probe tip.

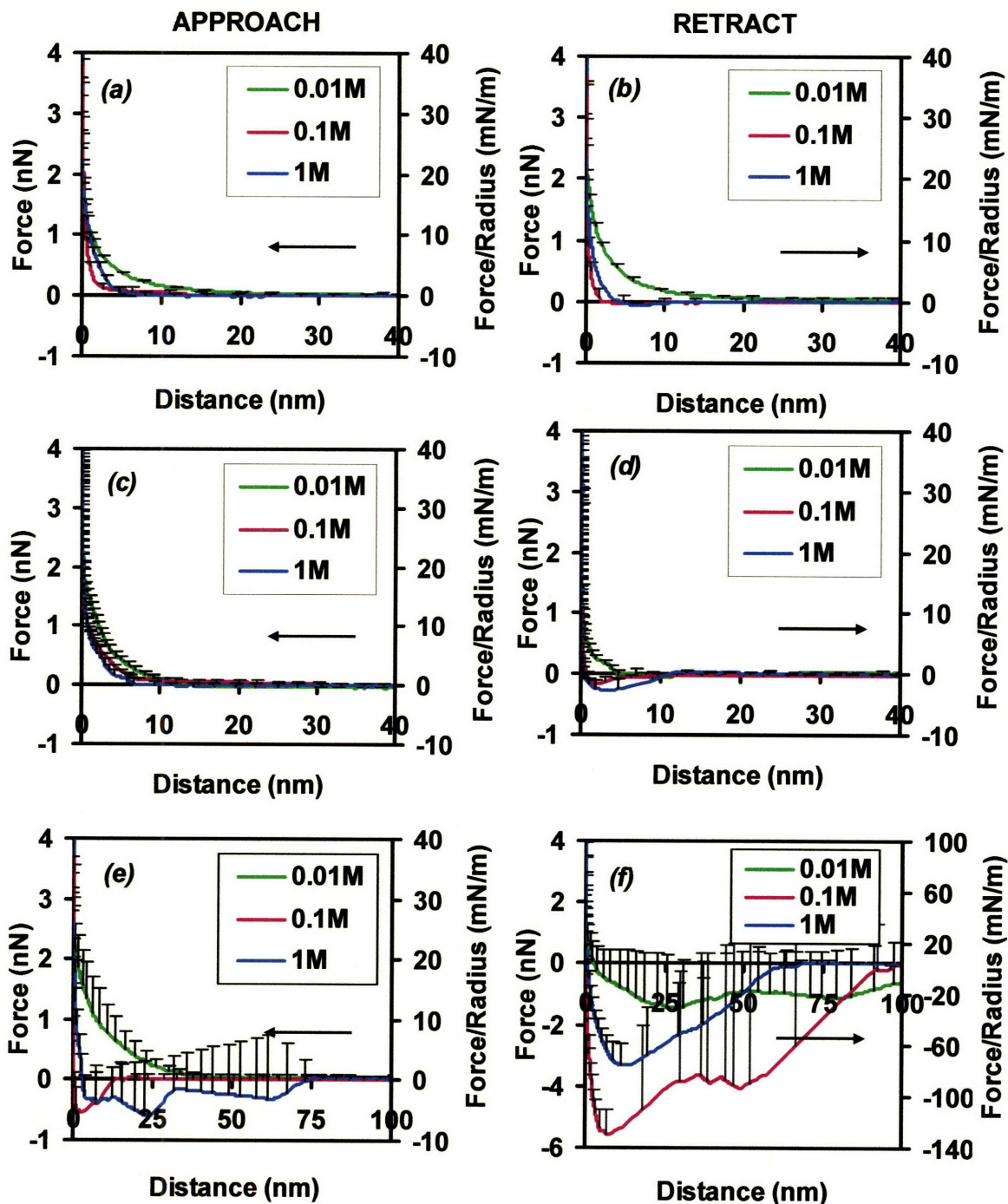


Figure 2-10. Nanomechanical data for Protein (Human Serum Albumin)-functionalized cantilever tip vs C_3EO_5 self assembling monolayers (SAMs) on flat Au as a function of incubation time in the C_3EO_5 solution (95% ethanol, 0.5 mM) and ionic strength of the aqueous media during approach and retract. Graphs (a), (c), and (e) are the approach curves for incubation times of 5 seconds, 24 hours, and 3 days, respectively. Graphs (b), (d), and (f) are the corresponding retract curves. A *Veeco* Au-coated Digital Instruments cantilever tip was used (spring constant: 0.06 N/m, probe tip end radius: 100 nm, displacement rate = $1\mu\text{m}/\text{sec}$). All experiments were carried out with a single probe tip.

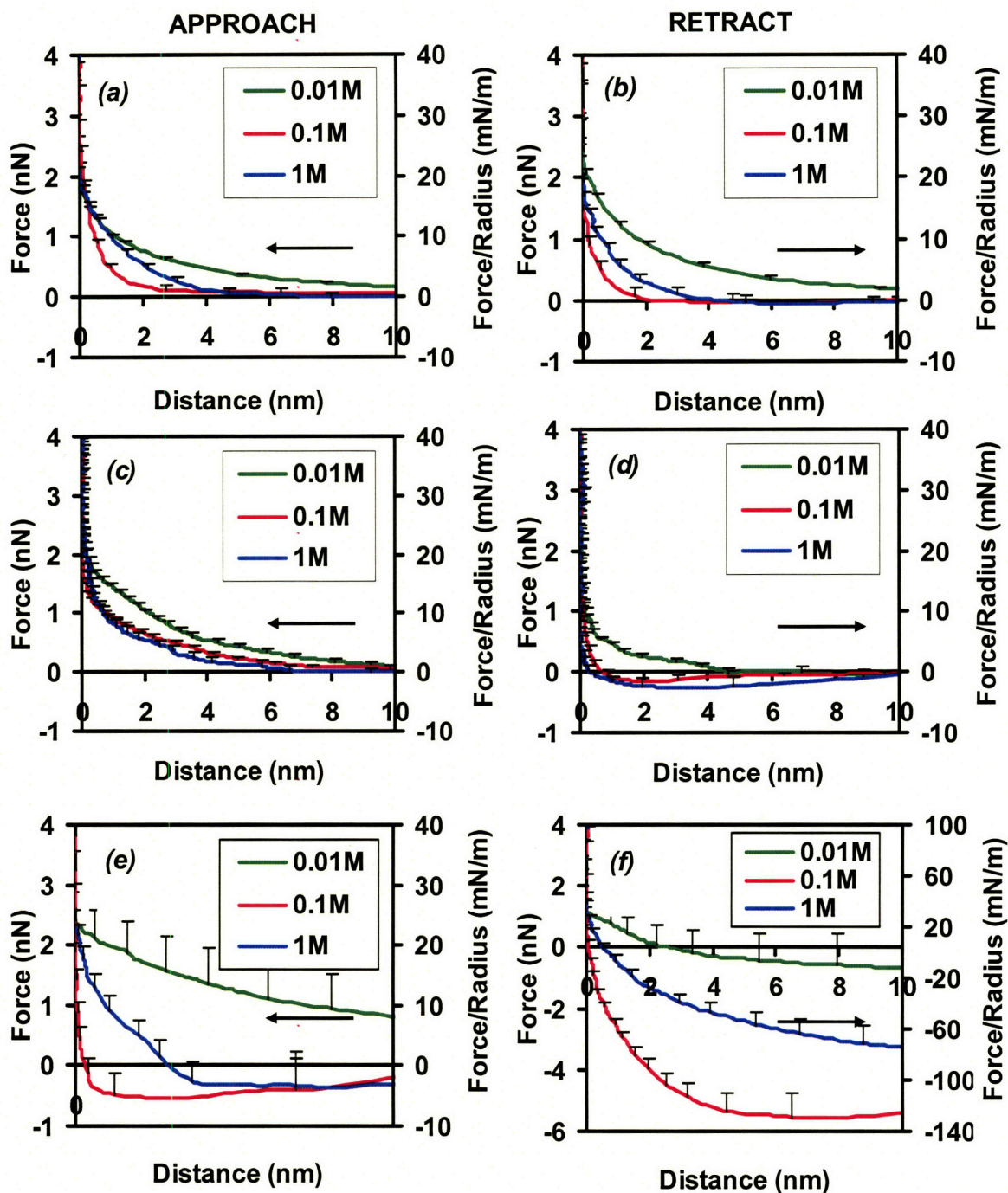


Figure 2-10A (magnified from Figure 2-10). Nanomechanical data for Protein (Human Serum Albumin)-functionalized cantilever tip vs C_3EO_5 self assembling monolayers (SAMs) on flat Au as a function of incubation time in the C_3EO_5 solution (95% ethanol, 0.5 mM) and ionic strength of the aqueous media during approach and retract. Graphs (a), (c), and (e) are the approach curves for incubation times of 5 seconds, 24 hours, and 3 days, respectively. Graphs (b), (d), and (f) are the corresponding retract curves. A *Veeco* Au-coated Digital Instruments cantilever tip was used (spring constant: 0.06 N/m, probe tip end radius: 100 nm, displacement rate = $1\mu\text{m}/\text{sec}$). All experiments were carried out with a single probe tip.

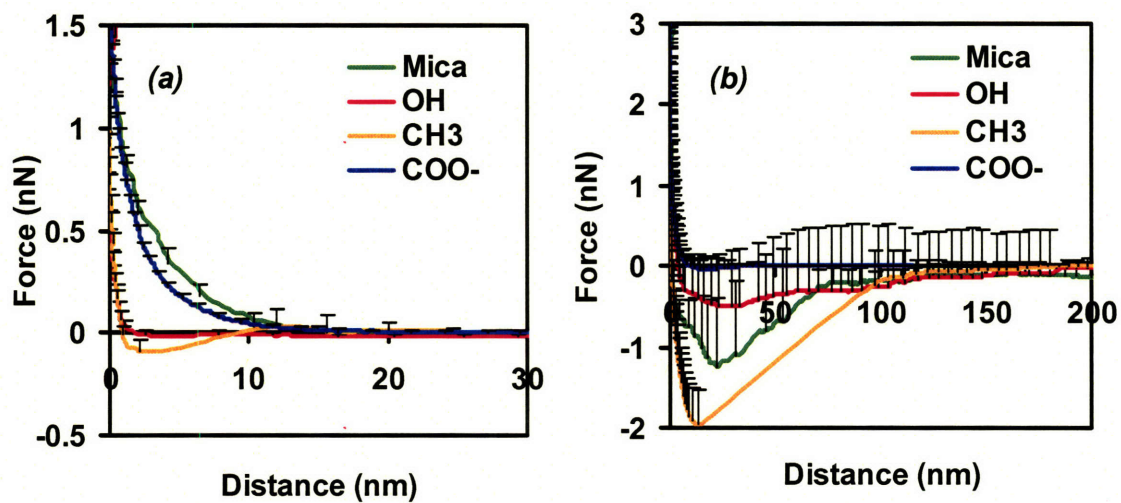


Figure 2-11. Nanomechanical data for CH₃, mica, OH, and COOH SAM on AU vs. an HSA protein tip. (a) approach curves and (b) retract curves. An Au-coated Digital Instruments cantilever tip was used (spring constant: 0.06 N/m, displacement rate = 1 $\mu\text{m}/\text{sec}$).

2.5 Discussion

To understand OEO-SAM's protein resistance mechanism, nanomechanical HRFS tests were employed to study the intermolecular and surface forces between C₃EO₅-SAM structures and chemically terminated or HAS-functionalized probe tips, with regard to various surface coverages and conformation. The results show that the 5 s incubated C₃EO₅-SAMs (60%-70% surface coverage) have higher resistance to HAS-functionalized tips and other types of terminated tips including the hydrophilic, hydrophobic and negatively charged tips (Figure 2-12).

The analysis of intermolecular forces was divided into two regions according to the distance between molecules: non-contact and contact regimes. The height of C₃EO₅-SAM was estimated at about 2.11 nm across 100% of the surface, which has a 7/2 helical conformation (Figure 2-2). From this, a jump to the surface of the C₃EO₅-SAM layer was observed only at 24 hr incubation with hydrophobic C₃EO₅-SAM vs OH- or hydrophilic CH₃-terminated SAMs (Figures 2-4A (c) and 2-6A (c)). This was not observed in any other experiment.

From this result, it is expected that the tip would penetrate the hydrogen-bonded water layer (about 1-2 nm⁹⁴) to reach the rigid surface of C₃EO₅-SAM (100% surface coverage), which is assumed to have no deformation. The flexible surfaces of C₃EO₅-SAMs (60-80% surface coverage) still had water layers because the C₃EO₅ conformers are deformable until they are fully compressed. Therefore, it is assumed that the tip does not penetrate the C₃EO₅-SAM but only compresses the C₃EO₅ molecules when it touches the surface of the C₃EO₅-SAM. Under this assumption, we can expect that the compression regime of the C₃EO₅-SAM on 60%-80% surface coverage will not be greater than the height of C₃EO₅-SAM, 2.11 nm. Therefore, considering 60% surface

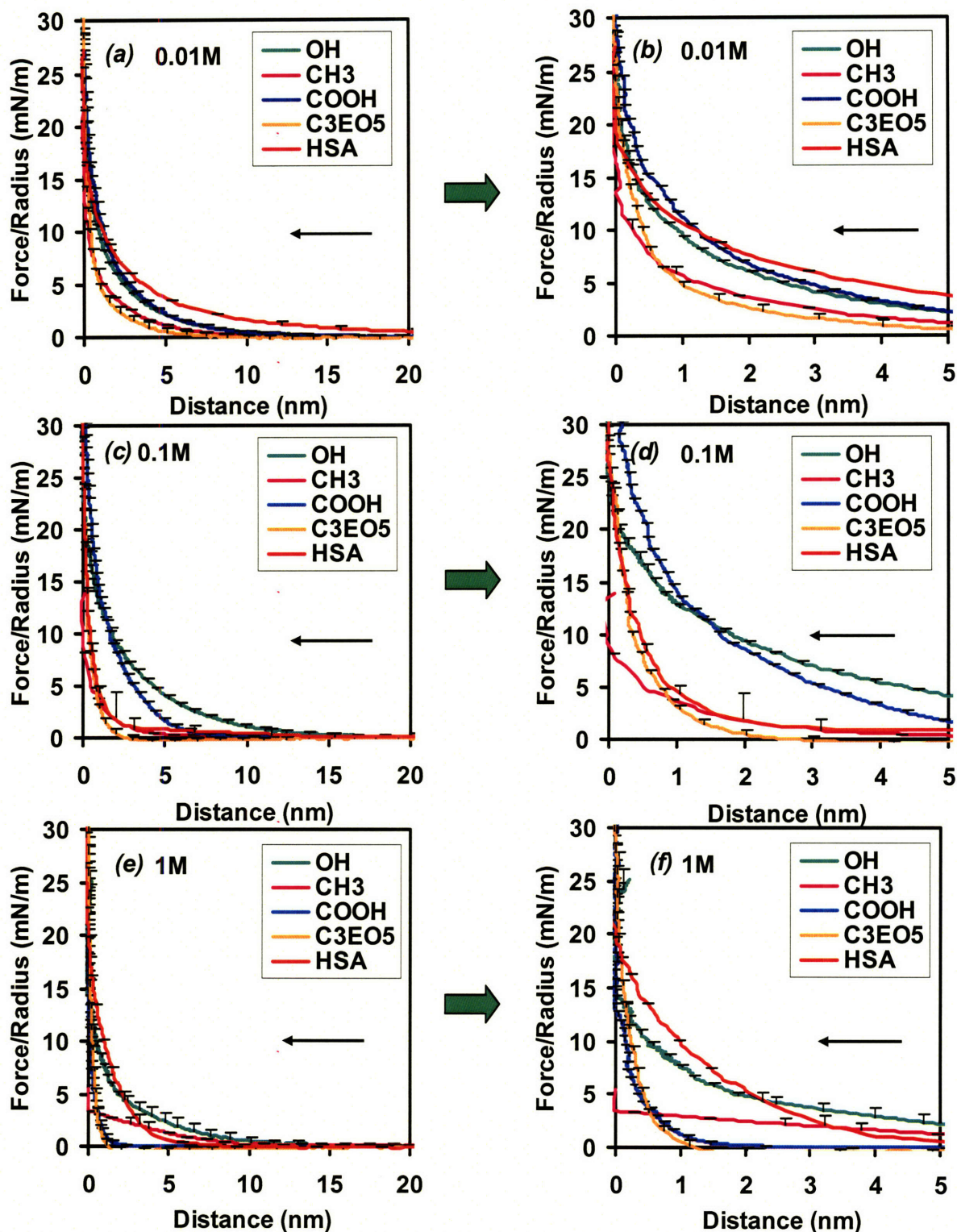


Figure 2-12. Nanomechanical data for all types of cantilever tips vs 5 second incubated C_3EO_5 SAMs on flat Au in the C_3EO_5 solution (95% Ethanol, 0.5 mM) with different ionic strengths of the aqueous media during approach. Graphs (a), (c) & (e) are on 0.01 M, 0.1 M & 1 M ISs of aqueous media consecutively. Graphs (b), (d) & (f) are magnified from (a), (c) & (e) consecutively. Veeco Au-coated Digital Instruments cantilever tips were used (spring constant: 0.06 N/m, displacement rate = 1 μ m/sec).

coverage, an approximate 2 nm compression will be the maximum compression distance of the contact regime. This compression distance may be greater at 100% helical conformation because it is densely packed. The chemically terminated SAMs on the tip are assumed to be more rigid than the C₃EO₅-SAMs since they are shorter in length and transform on densely packed 100% surface coverage. The maximum deformation of the chemically terminated SAMs are assumed to be under 1 nm with a 1 nm height of the chemically terminated SAMs. These SAMs are different from the C₃EO₅-SAMs because they have a 7/2 helical molecular conformation, even at 100% surface coverage.

When the tip is at the non-contact regime, where $D > \text{height}$, two possible origins of repulsive intermolecular forces exist: electrostatic interaction and hydration from templated water layers. First, we consider the electrostatic force as a potential contribution to the net repulsive interaction at a long range, over 4~5 nm, the range at which repulsion is expected to begin at 5 times the electrical Debye length from the surface. The Debye length, κ^{-1} , can be calculated from the equation, $1/\kappa = 0.304/\sqrt{[\text{NaCl}]}$ ⁶⁸ (only NaCl was considered, even though the ionic strength was calculated with both NaCl and a tris buffer. For the NaCl solution, $5' \kappa^{-1} = 5' 3.1\text{nm} = 15.5\text{ nm}$ at 0.01M IS, $5' 0.96\text{ nm} = 4.8\text{ nm}$ at 0.1M IS, and $5' 0.3\text{nm} = 1.5\text{ nm}$ at IS 1M. This explains why, as IS increases, the repulsive forces are reduced on both approach and retract curves of 5 seconds incubated C₃EO₅-SAM versus all other types of tips with a few exceptions such as the conversion of the repulsive force and a regime at 1M IS for COOH-terminated SAM and similar repulsive forces at all ISs of the 5 s incubated C₃EO₅-SAM tip vs the OH-terminated SAM tip (Figure 2-4, to be explained upon later in this chapter). This trend occurs on all incubation times even if

adhesive forces exist on retract curves with a 24 hr and 3 days incubated C₃EO₅-SAM.

By assuming there are no effects on HRFS data from the formation of gold oxide, Au₂O₃, after treatment with piranha and deprotonation of the mercaptan, the electrostatic interaction can also be explained theoretically by the effective surface charge equation from the dipole moment. Even if the C₃EO₅-SAM does not have a direct charge on the surface, it has the effective charge²¹ from a portion of the dipole moment. And because C₃EO₅-SAM is helical or amorphous³⁶, it can easily be “hydrated” (accommodating water molecules), which results in hydrogen-bonded water layers.^{33, 34, 35} This “soft” permeable phenomena²¹ with polar groups provides an effective surface charge, σ_{eff} , with dipole density, ν , and surface charge density, σ ^{69,70}.

$$\sigma_{eff} = [\sigma \cosh(\kappa l) + \nu \kappa \sinh(\kappa l)]e^{-\kappa d} \quad (1)$$

where l is the “soft” polar region. Because the effective surface charge, σ_{eff} can be numerically calculated using the DLVO theory^{69,70} from the HRFS data of 5 seconds incubated C₃EO₅-SAM vs 5 seconds incubated C₃EO₅-SAM (60-80% surface coverage, 0.01M IS) assuming the Hamaker constant, D is 0.33×10^{-20} J which is calculated from the following equation⁷¹.

$$D_{jump-to-contact} = \left[\frac{AR_{tip}}{3k} \right]^{1/3} \quad (2)$$

where k is a spring constant. From this numerical calculation (Figure 2-13), the effective surface charge, σ_{eff} of the C₃EO₅-SAM was estimated as -0.0069 C/m². For over 5 nm distance, there is almost no effect from van der Waals (VDW) force. Therefore, even if the Hamaker constant, D , is assumed to be 0, the numerical

calculation for the effective surface charge is almost the same. Because at 0.1M IS, $5 \kappa^{-1} = 4.8 \text{ nm}$, it is hard to assume the Hamaker constant, D , is 0 in this regime; the electrostatic interaction regime overlaps with the van Der Waals interaction regime. Alternatively, the effective surface charge, σ_{eff} , of the C₃EO₅-SAM can be numerically calculated from the HRFS curve of C₃EO₅-SAM vs COOH-terminated SAM because the surface charge density of the COOH-terminated SAM is known as $0.017^{72} \sim 0.021^{73} \text{ C/m}$.

By using $\sigma_{eff} = -0.0069 \text{ C/m}^2$, $l = 2 \text{ nm}$, $\kappa^{-1} = 3 \text{ nm}$ at 0.01 M, the dipole density, $\nu = 5.62 \cdot 10^{-11} \text{ C}\cdot\text{m}/\text{m}^2$ is calculated. With the dipole density and 80% of the 100% molecular packing density $4 \cdot 10^{-2} \text{ molecule}/\text{nm}^2$ ³¹, the dipole moment, 5.27 (the value that was divided by 1D (debye) $\gg 3.33564 \cdot 10^{-30} \text{ C}\cdot\text{m}$) was calculated. This result is similar to values from another experiment²¹ and a quantum mechanical study of OEO⁵⁸ for helical conformer. Interestingly, the longer and higher range repulsive forces on approach of HRFS were observed in the charged tips (COOH-terminated SAM tip or HSA-functionalized tip) vs C₃EO₅-SAM at 0.01 M IS than those of other tips vs C₃EO₅-SAM curves. However, as the ionic strength increases, the charged tips' repulsive forces vs those of the C₃EO₅-SAM decrease more than others (Figure 2-12). This agrees with the Debye lengths of electrostatic forces of different ionic strengths; the result shows that the electrostatic interaction more effectively relates to the repulsive forces of the charged tips.

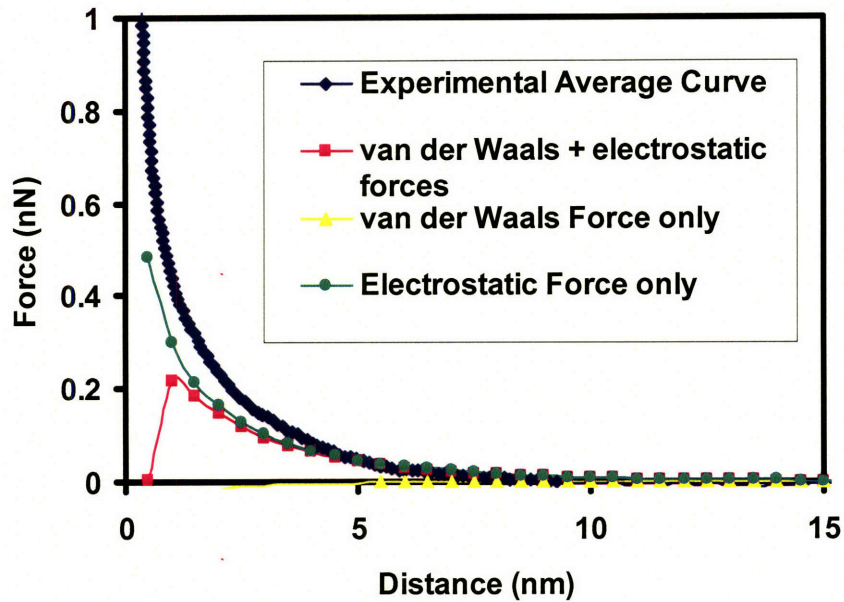


Figure 2-13. Numerical calculation of the average force (nN) versus distance, D (nm). The experimental C_3EO_5 -terminated self assembling monolayer (SAM)-coated cantilever tip vs C_3EO_5 SAMs on flat Au approach curve (blue) is compared to the DLVO electrostatic surface charge model (electrostatic force + van der Waals force, pink), the only van der Waals force model (yellow), and the only electrostatic force mode model (green), $\kappa^{-1} = 3$ nm, $IS = 0.01$ M, Hamaker constant, $D = 0.33 \times 10^{-20}$ J, fitting range: 5 ~ 15 nm. σ_{eff} of the C_3EO_5 -SAM was numerically calculated as -0.0069 C/m².

The OH-terminated SAM tip vs the C₃EO₅-SAM had almost the same amount of highly repulsive forces within a 10 nm range on all 0.01 M, 0.1 M and 1 M ISs. Hydrophilic OH-terminated SAM tips should also have water layers as C₃EO₅-SAM, and this hydrophilic repulsive interaction is expected to prevail on other interface forces on all ISs. The shorter repulsive force of the hydrophobic CH₃-terminated tip (no hydrogen-bonded water layer) vs C₃EO₅-SAM (about 5 nm at 0.01 M 5 in the second incubation is about two times less than that of the OH-terminated SAM tip vs C₃EO₅-SAM) supports this idea (Figure 2-12). From these results, we can expect that the short-range repulsion on the non-contact regime is caused by the hydrogen-bonded water layers. This was also supported by the MD simulation and wettability experiment.⁷⁴ In addition, the hydration of the C₃EO₅-SAM in water results in the excluded-volume effect and directly relates to the steric repulsion theory^{75, 28, 29}

When the tip contacts the surface (contact regime), the molecular mobility (flexibility) increases on the 60%-80% surface coverage case over the 100% surface coverage case with 7/2 helical conformers, and gives the repulsive mobility as Vanderah et al. suggested. The jump-to-surface or penetration to the surface was not observed in the 5-second incubated C₃EO₅-SAM, which can be explained as this: when the tip approaches the surface, the flexible C₃EO₅-SAM works as a spring to prevent the jump force. The hydrogen-bonded water-layers are still alive in the contact regime because of this flexible behavior of C₃EO₅-SAM.

2.6 Conclusion

The HRFS results clearly show a repulsive interaction between the C₃EO₅ SAM at 60-80% surface coverage and the protein (human serum albumin)-functionalized tip,

as well as all hydrophilic, hydrophobic, or negatively charged tip surfaces. The overall results support the theory that the protein resistance of the less ordered C₃EO₅-SAM (60%~80%) results from a combination of electrostatic interaction (non-contact regime, long-range) between the hydrogen-bonded water layer (non-contact regime, short range and possible contact regime) and mobility (flexibility) of the C₃EO₅-SAM (contact regime). A detailed drawing of this protein resistant scenario and a suggestion for a protein-resistant design are discussed in Chapter 6.

CHAPTER 3

High Resolution Atomic Force Microscopy Imaging of Supported Lipid Bilayers

3.1 Introduction

Lipid bilayers attached to solid supports provide a versatile cell-membrane (Figure 3-1) mimetic model system for use in applications such as biosensors, biological arrays, and biomedical devices. They also serve as an excellent platform to quantify and study the mechanisms of cellular processes such as adhesion, fusion, migration, and exo- and endocytosis.⁷⁶ For this purpose, biologically relevant synthetic lipids such as phosphorylcholine (PC) have been studied.^{77,78,79,80,81,82,83,84,85,86} In addition, recent research shows that the zwitterionic PC moiety creates a protein-resistant property that is more dominant on the fluid PC lipid layers.^{87,88,89,90,91}

Lipids are amphiphilic molecules that have a hydrophilic head group and hydrophobic tail. Lipids form bilayers when the value of the dimensionless shape factor, v/a_0l_c , is near to 1⁹² (v : the volume of the tail group (hydrocarbon), a_0 : optimal head group area, l_c : critical chain length, which is smaller than a fully-extended hydrocarbon chain length, l_{max} , a_0l_c : the maximum volume of the tail group). If the shape factor is under 0.5, which means v is much smaller than a_0l_c , lipids form a micelle instead of a planar lipid bilayer. This criteria means that if the head group of lipid is too small or the tail (hydrocarbon chains) is too bulky, lipids form bilayers instead of micellar structures.

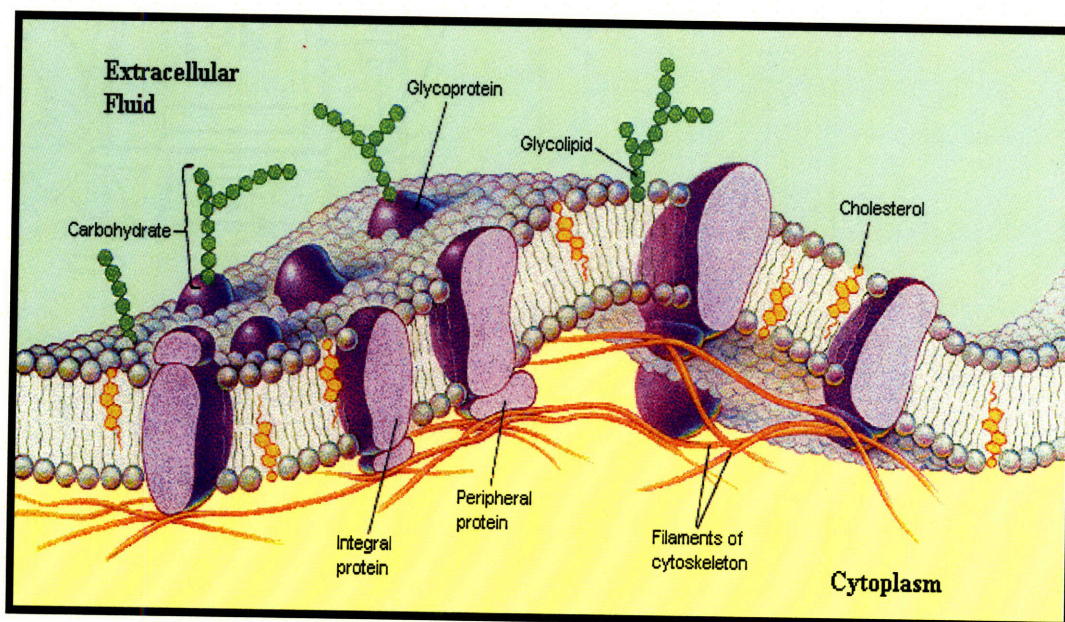


Figure 3-1. Schematic of endothelium cell membrane.⁹³

The purpose of this chapter is to optimize the incubation methods to achieve a well-prepared phospholipid monolayer and bilayer and to characterize the surface of these layers by using several types of AFM tips as the environment changes such as when ionic strength and incubation time are changed. These layers will be used later for the nanomechanical tests discussed in Chapter 4 and 5. At the start of this research project, 1-palmitoyl-2-oleoyl-sn-glycero-3-phosphocholine (POPC, unsaturated tail, Figure 3-2 (a))^{94, 95, 96} was studied and later 1,2-dipalmitoyl-sn-glycero-3-phosphocholine (DPPC, saturated tail, Figure 3-2 (b)) was studied. The latter creates a stronger interaction between the lipids due to the strong hydrophobic interaction between saturated tails and because it has a gel phase at room temperature (the transition temperature from a gel to fluid is about 60°C ⁹⁸). In contrast, POPC is in a fluid phase at room temperature; the transition temperature to a fluid phase is -6°C .⁹⁷ DPPC has been studied with other lipids to see how the gel phase and saturated tail

affect the lipid plane's profile, characteristics of a lipid surface, and its interaction with other molecules such as proteins.^{98,99,100,101}

AFM imaging has been used to prove that only one lipid bilayer exists¹⁰² and to observe the phase change of the lipid bilayer under different conditions such as various ionic strengths¹⁰³ and temperatures.¹⁰⁴ In this test as the temperature reached the phase transition point from the solid to the fluid phase, holes in lipid bilayer disappeared and formed a planar surface.^{98,104} This observation shows that lipids have more flexibility and that they bind to each other loosely in the fluid phase.

Recently, Jarvis et al. succeeded in obtaining an AFM image of hydrated water layers that cover the DPPC bilayer by using frequency modulation atomic force microscopy (FM-AFM).^{98,105} A detailed analysis shows a 0.28 nm thickness of two hydrated water layers, which are strong and stable enough to serve as energy barriers.^{98,105}

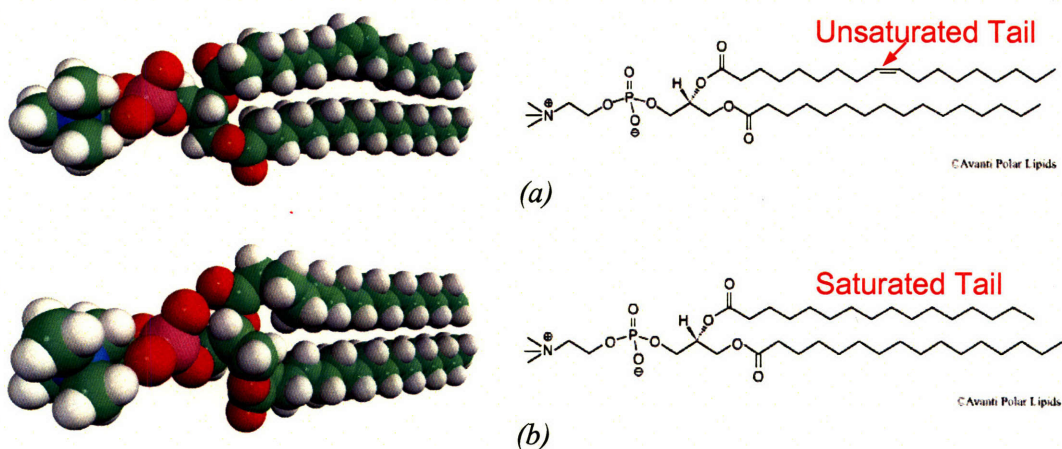


Figure 3-2. Chemical structure of phosphorylcholine (PC) (a) POPC, (b) DPPC, pictures by ©Avanti Polar Lipids.

3.1.1 Theoretical Calculation of the Height of Phosphorylcholine (PC) in an

Aqueous Solution

The formation of phosphorylcholine (PC) lipids in an aqueous solution does not result in a trans-form (Figure 3-2) but a tilted form (Figure 3-3, the head group is tilted to the tail). The hydrogen bonded water molecules on the phosphate phosphorus and nitrogen choline of the head group were observed in a molecular dynamics (MD) study¹⁰⁶ and an AFM experiment using a nanotube tip.⁹⁸ Therefore, the main distribution of the lipid layers' height stems from the tail length and hydrogen bonded water layers on the phosphate phosphorus. If just the tail group lengths from the end of the tail to the phosphate head group are calculated (assuming that the tail is perpendicular to the substrate), the height of one lipid layer of PCs is expected to be 1.9 nm (DPPC) and 2.1 nm (POPC) (Table 3-1). The water layer can be placed in the middle of the lipid bilayer; the thickness and distribution of water layer depends on the particular type of lipid and environment.¹⁰⁷ Therefore, the gap between the two lipid layers and the hydrogen bonded water can be destroyed if the tip makes strong contact (at a higher set point) during AFM scanning; the total height of the lipid bilayer is expected to be approximately 4~5 nm (Figure 3-4).

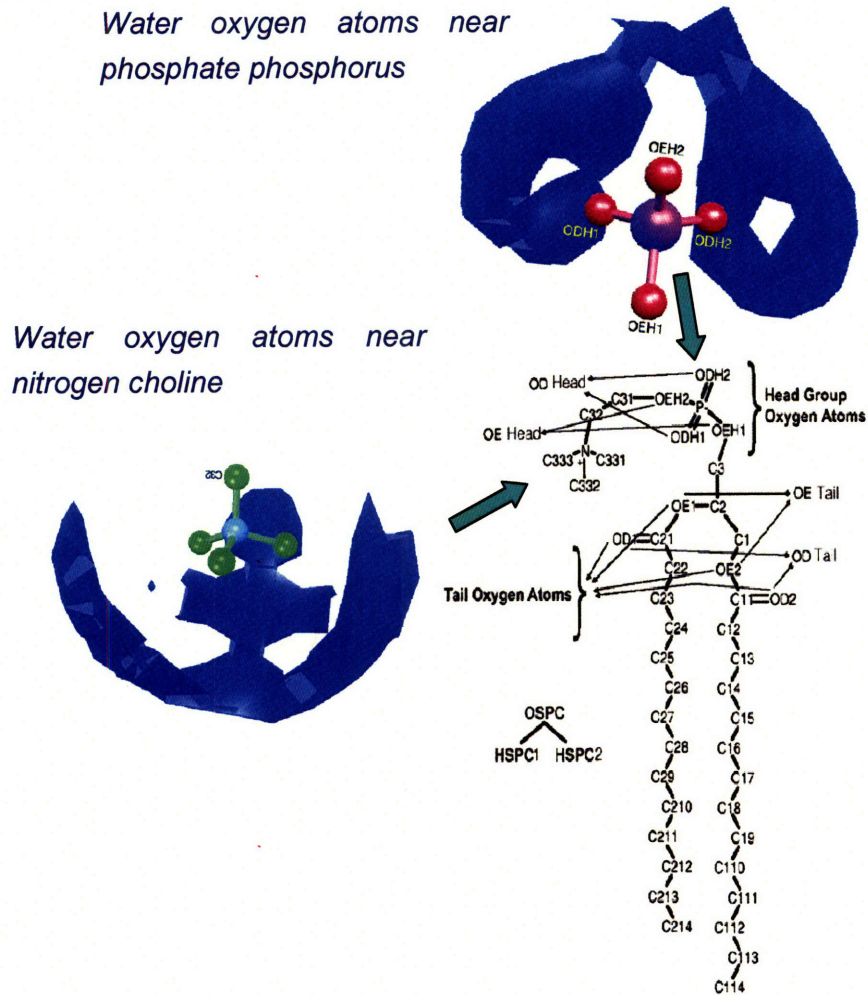


Figure 3-3. DMPC structure in fluid- and hydrogen-bonded oxygen atoms on the head group near phosphate phosphorus and nitrogen chloride. Adapted from reference.¹⁰⁶

DPPC

Bond	Unit Bond Length (pm)	Number of Bonds / Lipid	A=Bond Angle (degree)	cos (A/2)	Total Bond Length (pm)
C-C	154	17	109	0.58	1518.44
C-O	143	3	109	0.58	248.82
C-N	143	0	109	0.58	0
O-P	163	1	109	0.58	94.54
C-H	107	1	109	0.58	62.06
		Tail total			1923.86

POPC

Bond	Unit Bond Length (pm)	Number of Bonds / Lipid	A=Bond Angle (degree)	cos (A/2)	Total Bond Length (pm)
C-C	154	17	109	0.58	1518.44
C-O	143	3	109	0.58	248.82
C-N	143	0	109	0.58	0
O-P	163	1	109	0.58	94.54
C-H	107	1	109	0.58	62.06
C:C	133	1	0	1	133
		Tail total			2056.86

Table 3-1. Theoretical calculation of the length of the lipid tail groups for DPPC, DMPC and POPC.

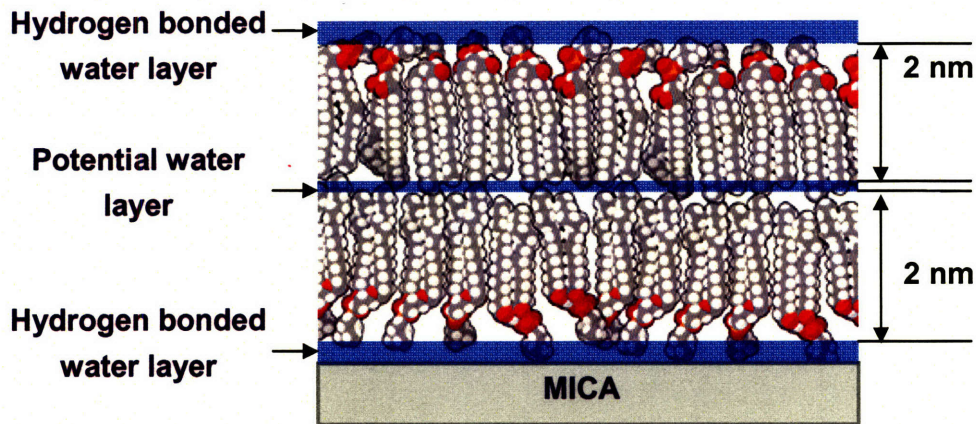


Figure 3-4. Typical structure of the phosphorylcoline lipid bilayer on a flat mica substrate. Lipid bilayer picture from Wikipedia (http://en.wikipedia.org/wiki/Lipid_bilayer).

3.2 1-Palmitoyl-2-Oleoyl-*sn*-Glycero-3-Phosphocholine (POPC)

3.2.1 Sample Preparation

Vesicle fusion technique

POPC (Avanti Polar Lipids Inc., Alabaster, AL) lipid bilayers were prepared according to the vesicle fusion technique in a similar manner as were the lipid monolayers discussed in Chapter 1.⁴⁵ The lipid bilayer formed on the hydrophilic surface via the processes of vesicle adsorption, rupture and fusion, etc.^{108,109,110,111,112, 113, 114,115} The driving force of vesicle rupture and fusion derives from the surface adhesion energy.^{116,117}

The preparation of POPC vesicles is detailed as follows. The 0.6 mL POPC in chloroform was dissolved in 10 mg/mL 9:1 chloroform/methanol solution. This POPC solution was gently dried out by nitrogen. The 6 mg POPC in the chamber was lyophilized for 8 hours. This lyophilized POPC was rediscover in 2 mL of 10 mM degassed Tris buffer (150 mM NaCl, pH8), which was sonicated for 30 minutes and

centrifuged at 6000 rpm in 5 mL tubes (344057 from Beckman) with a 50.1 Ti swinging rotor. Finally, the centrifuged solution was diluted to 2 mM with the Tris buffer.

After centrifuging, the POPC vesicles were characterized by a particle-size analyzer (90 Plus particle size analyzer, Brookhaven Instruments Corporation) and found to have a mean hydrodynamic diameter of 33.3 ± 0.08 nm (Figure 3-5).

The solution with POPC vesicles was incubated on the CH₃- and OH-terminated SAMs and rinsed after various incubation times to create the lipid monolayer or bilayer.

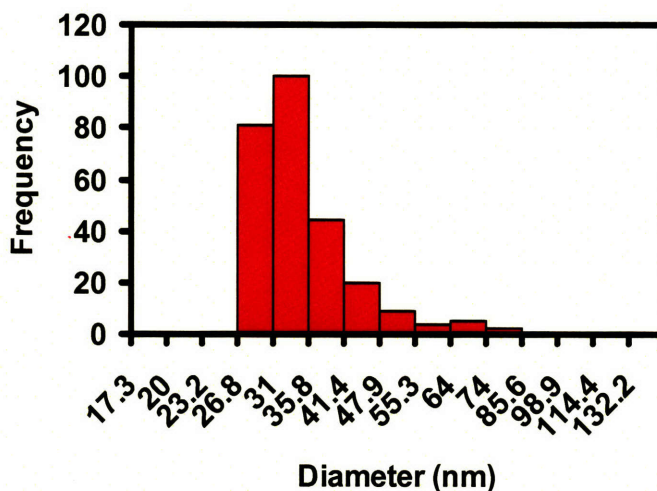


Figure 3-5. Distribution of POPC vesicle size by a particle size analyzer (90 Plus Particle Size Analyzer, Brookhaven Instruments Corporation).

Choices and Preparation of Terminated Au Substrate and Tips

To form self-assembled monolayer (SAM) substrates and tips, the gold-coated substrates and gold-coated Veeco pyramidal DNP silicon nitride tip (spring constant: 0.06N/m) were incubated for 24 hours in 25 mL of 5 mM solution which was prepared using 0.0255 g of 11-mercapto-undecanol (HS-(CH₂)₁₁-OH, 45056-1) and 30 μ L of 1-dodecanethiol (HS-(CH₂)₁₁-CH₃, 47135-4) in an ethanol solvent. The pictures of both

the CH₃- and OH- terminated tips were taken by scanning electronic microscope (SEM) after all POPC experiments in Chapter 3 and 4 (Figure 3-6). Both the 11-mercaptoundecanoic acid and 1-dodecanethiol were purchased from Sigma Aldrich. To ensure a clean surface, all gold-coated tips, as well as the gold substrates, were Piranha treated (1:3 H₂O₂:H₂SO₄) for 3 seconds on the tips and 5 minutes on the Au substrates immediately before all functionalization. The vesicle fusion technique was used to functionalize the lipid layers.

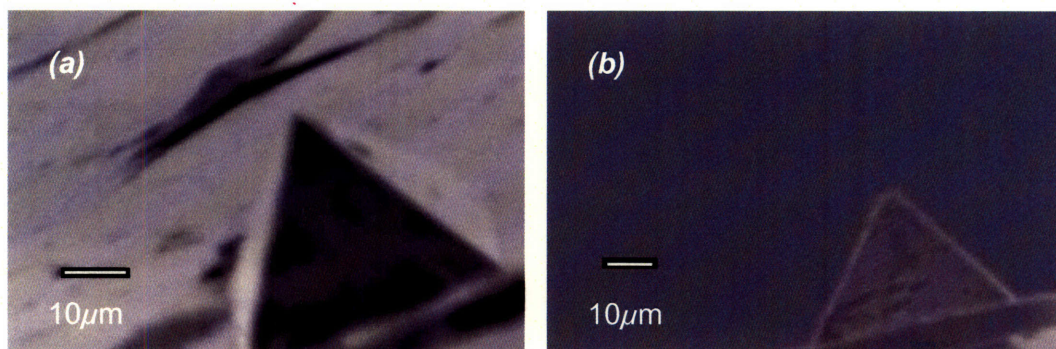


Figure 3-6. Tip images from scanning electronic microscope (SEM) (a) CH₃-terminated tip, and (b) OH-terminated tip. Gold-coated Veeco pyramidal DNP silicon nitride tips (spring constant: 0.06N/m) were incubated in 5mM solution of 11-Mercapto-undecanol (HS-(CH₂)₁₁-OH) and 30 μL of 1-dodecanethiol (HS-(CH₂)₁₁-CH₃) in an ethanol solvent.

Microcontact-Printing Procedure

Microcontact-printing (μ CP) was used to prepare the planar surfaces with two or more different chemically functionalized patterned areas. This technique use patterned PDMS stamps (in this case, a hexagon or line pattern) to chemically functionalize one pattern where the stamp first make contact with the surface. Then, the sample is incubated in the second solution to functionalize outside of the pattern. In this

case, hydrophobic (1-dodecanethiol) and hydrophilic (11-mercapto-undecanol) alkanethiol SAMs were functionalized in order, respectively, on the same gold surface. The procedure was as follows (Figure 3-7). PDMS stamp was soaked in 0.3 mM 11-mercapto-undecanol solution for SAM outside the hexagons for 1 hour. The Au substrate was cleaned with Piranha (98% sulfuric acid + 33% hydrogen peroxide in 3:1 ratio) for 5 minutes. The soaked stamp was turned over and applied to the cleaned Au surface for 30 seconds. The Au and stamped surface was placed in the solution so that SAM can form inside the hexagons for 24 hours.

The POPC vesicles solution was incubated on a microcontact-printed substrate and rinsed after the incubation in order to make the POPC monolayer and bilayer on the same substrate. On the hydrophilic OH-terminated SAM, lipid bilayers formed because the hydrophilic head group were first adsorbed to the hydrophilic surface and the hydrophobic tails then met other hydrophobic tails (Figure 3-4). In contrast, only the POPC monolayer formed on the hydrophobic CH₃-terminated SAM because the hydrophobic tails were adsorbed to the hydrophobic surface.

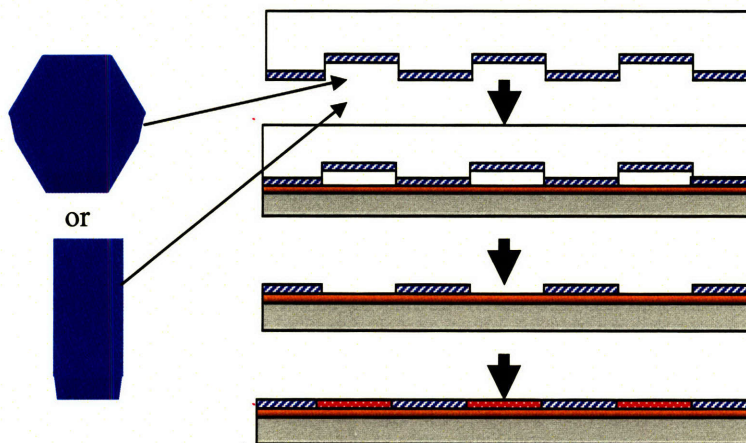


Figure 3-7. The Microcontact-Printing procedure.

In the SPR experiments, 0.2 mM POPC vesicles (size < 50 nm) in 10mM Tris buffer (150 mM NaCl, pH 7.8) were flowed onto a hydrophobic, CH₃-terminated SAM (AuS-(CH₂)₁₁-CH₃) on the Au substrate to create the POPC monolayer on the surface (association kinetics on Figure 3-8). After 28 min, the surface was rinsed by only Tris buffer (dissociation kinetics on Figure 3-8) to clean the physically observed lipids. After 2050 seconds, the SPR data showed the equilibrium formation of a full monolayer (1380 RU, Figure 3-8). This result clearly shows the formation of a monolayer on a hydrophobic surface. This preliminary SPR experiment confirmed the formation of the lipid monolayer from the prepared solution of POPC vesicles.

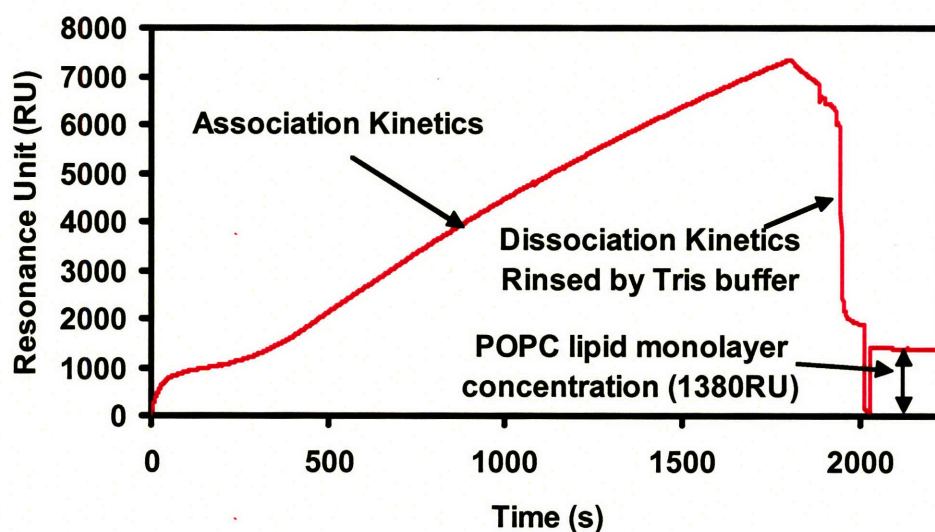


Figure 3-8. SPR result: a flowing POPC vesicle on the CH₃-terminated SAM. 0.2 mM POPC vesicles (size < 50 nm) in 10 mM Tris buffer (150 mM NaCl, pH 7.8).

3.2.2 Experimental Method

Atomic force microscopy (AFM) was used primarily in the contact mode or tapping mode with a Veeco DNP AFM probe tip to scan the lipid monolayers and bilayers (Figure 3-9). The set point was minimized so as to minimize the pressure from

the tip to the surface of the lipid layers. Based on the AFM images, a section analysis was performed to check the height of the lipid layers; to prove that the formation of the lipid bilayer or monolayer was not a multilayer, a square test was performed by scanning the middle of the AFM image with high pressure scanning. After the high pressure scanning, a larger AFM image was taken again to check if the height differed between the image's inside and outside. To support the liquid environment, the Veeco liquid cell was set up and the solution was then changed without disturbing the setup. This enabled scanning of the same position even after changing the solution's ionic strength.

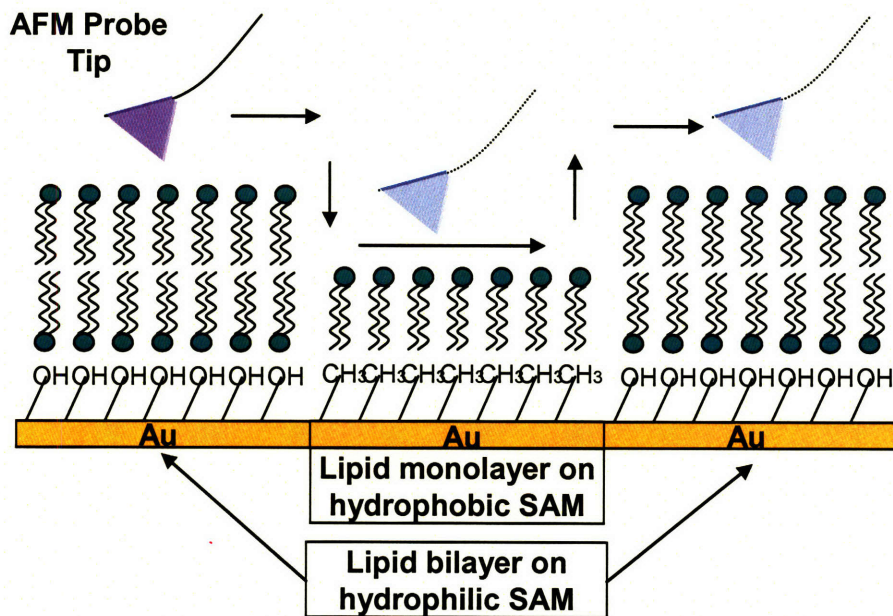


Figure 3-9. Schematic view of an AFM scan on the lipid bilayer and monolayer which is on the surface of hydrophilic OH-terminated SAM and hydrophobic CH₃-terminated SAM (not drawn to scale).

3.2.3 POPC AFM Imaging Result & Discussion

The goals of the AFM imaging experiment were to verify the formation of a lipid monolayer or bilayer, and to characterize the extent of formation and uniformity at various ionic strengths.

AFM height, friction, and phase images were taken in contact and tapping modes in 10 mM Tris buffer solution (10 mM NaCl, pH 7.8) with the PicoForce Digital Instrument AFM and a standard Si₃N₄ probe tip, which is negatively charged at this pH. These experiments showed the formation of POPC lipid mono- and bilayers on CH₃- and OH-terminated SAMs, respectively, by comparing the experimentally measured height difference between mono- and bilayers to the theoretical estimated values (Section 3.1.1). Theoretical calculation of the height difference between the CH₃- and OH-terminated SAM is 0.364 nm (OH-SAM is higher) and the height of one POPC lipid monolayer is approximately 2.1 nm as discussed in Section 3.1.1.

Before POPC incubation, μ CP AFM images of CH₃- and OH-terminated SAMs in 10 mM Tris buffer solution (10 mM NaCl, pH 7.8) showed no statistically significant difference between the heights outside and inside of the hexagon. However, the boundary between the CH₃- and OH-terminated SAMs was still recognizable because there was a discernable shallow gap between them (Figure 3-10 (a)). After 15 minutes of POPC incubation, the section profile from the AFM image on the contact mode showed the rough surface on the outside of the hexagon, which was supposed to be a POPC bilayer (Figure 3-10 (c)) even if the height difference between the inside and the outside of hexagon was still clear (Figure 3-10 (b)). In order to minimize the pressure from the tip and obtain the accurate value of the height difference, a height analysis was performed for the overall AFM images, which were scanned continuously in tapping

mode at the same position; each AFM image was taken for each scan. Figure 3-11 shows that the height difference was consistently about 1.9 nm between the POPC bilayer on the CH₃-terminated SAM and the POPC monolayer on the OH-terminated SAM for all AFM tapping mode images. The standard deviation of the height difference decreased as the number of scans increased. This result clearly shows the formation of the POPC mono- and bilayers. It is expected that the POPC incubation time should be over 15 minutes in order to obtain well ordered POPC bilayer; the effect of the incubation time on the formation of lipid layers is examined more later in this chapter.

Before performing the POPC incubation, friction images clearly show a difference in friction between CH₃- and OH-terminated SAMs (Figure 3-12 (a)). After the POPC incubation, however, there was no clear difference of friction between the POPC bilayer on the CH₃- terminated SAM and monolayer on the OH-terminated SAM (Figure 3-12 (b)). This proves that the head groups of POPC are on the surface of both the monolayer and bilayer.

The inversion of the phase image was observed after the incubation of POPC vesicles (Figure 3-13). The outside of hexagon was brighter than inside before the incubation of POPC vesicles (Figure 3-13 (a)). This is expected to indicate that the difference between hydrophilic and hydrophobic surfaces. However, after the incubation of POPC vesicles (Figure 3-13 (b)), the inside of hexagon was brighter than the outside. This inversion of the phase image in Figure 3-13 (b) is expected to indicate the differences in height and elasticity between lipid bilayers and monolayers.

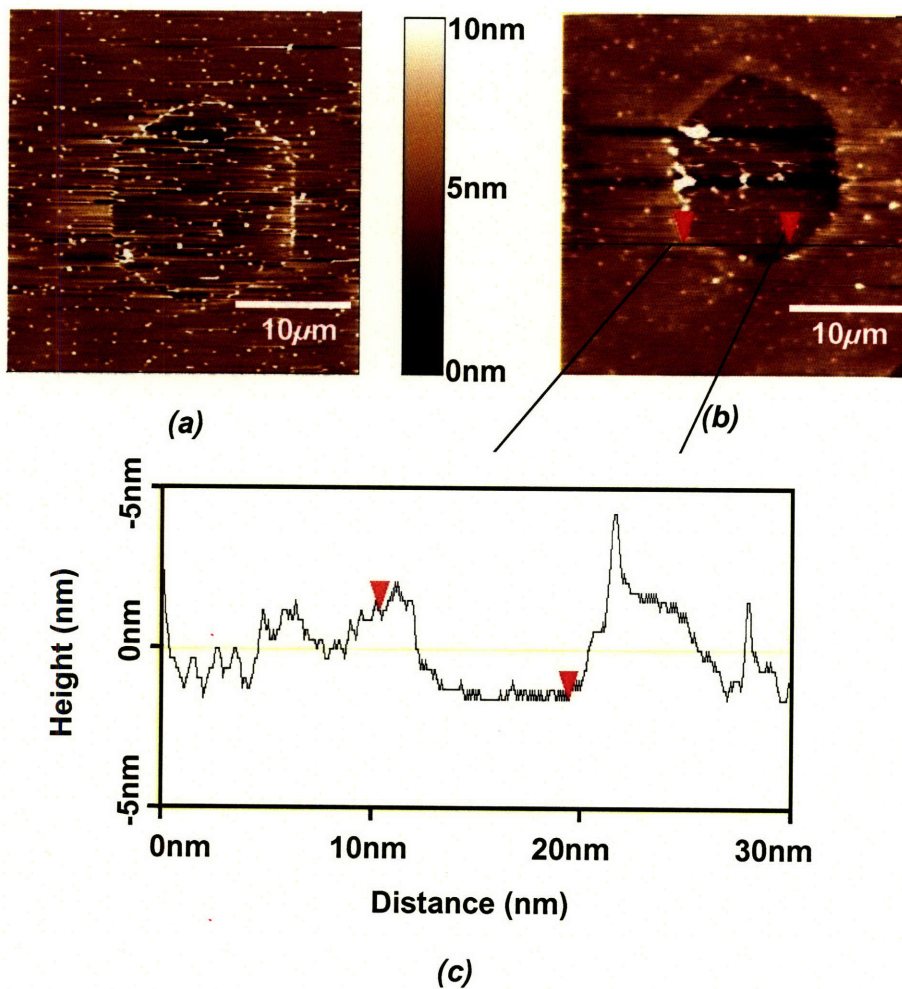


Figure 3-10. Height images and section analysis on contact mode (a) μ CP AFM images of CH_3 - and OH - terminated SAMs in deionized water before POPC incubation (control samples), (b) μ CP AFM images of SAM functionalized samples in Tris buffer after POPC incubation, (c) cross-sectional analysis of the selected line from the image of (b).

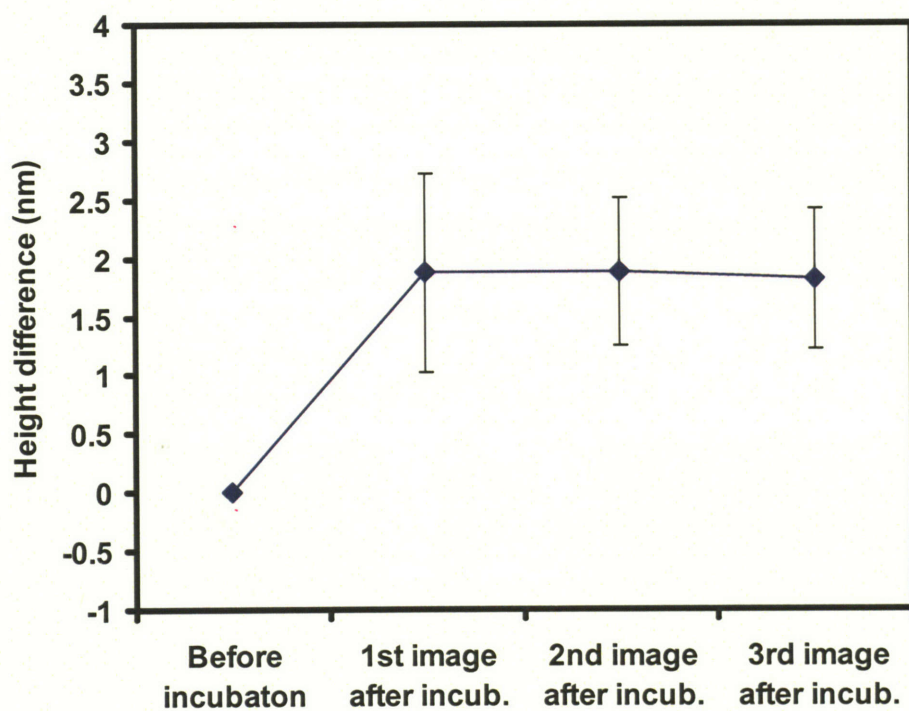


Figure 3-11. Average height difference between hydroxyl and methyl SAMs before and after POPC incubation measured in tapping mode. Three images were scanned continuously on the same position.

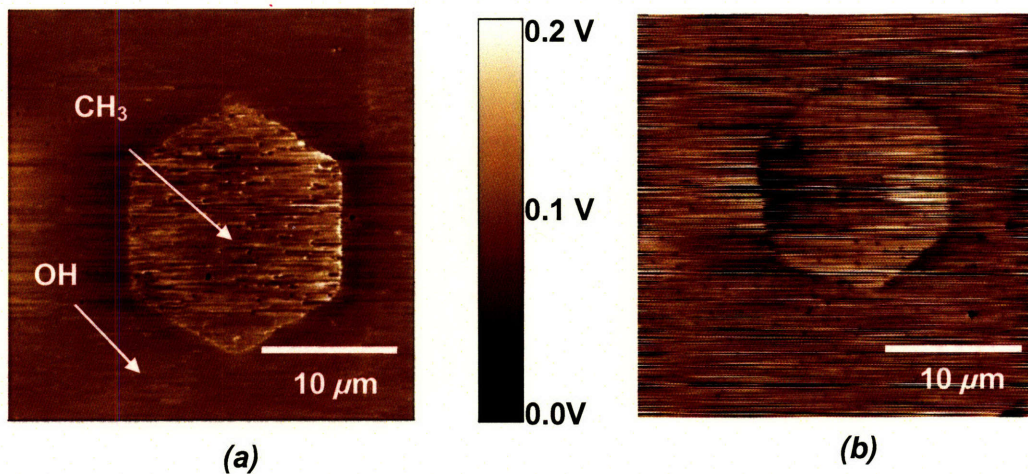


Fig 3-12. Friction images on contact mode (a) μ CP AFM images of CH_3 - and OH -terminated SAMs in deionized water before POPC incubation (control samples), (b) μ CP AFM images of the SAM functionalized samples in Tris buffer after POPC incubation.

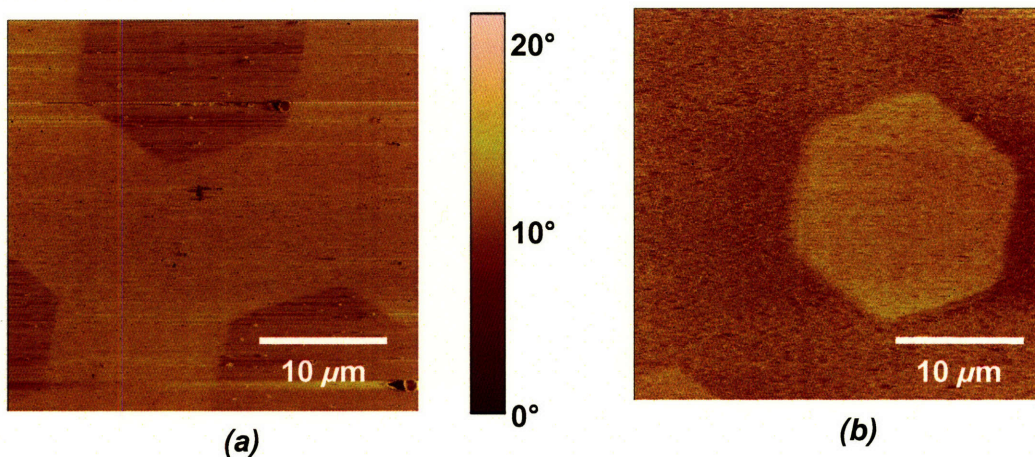


Figure 3-13. Phase images in tapping mode (a) μ CP AFM images of CH_3 - and OH -terminated SAMs in deionized water before POPC incubation (control samples), (b) μ CP AFM images of the SAM functionalized samples in Tris buffer after POPC incubation.

The hexagon patterns worked well for qualitative analysis, but they were less ideal for quantitative analysis. Because of the multidirectional boundaries, there is greater chance that these boundaries are irregular than simpler patterns. In order to obtain quantitatively better analysis, line patterns were used. Using these line patterns, another set of AFM height, deflection, and friction images were taken in contact modes in 10mM Tris buffer (150 mM NaCl, pH 7.8) with Pico Force DI AFM. The ionic strength and pH of this environment are close to the *in vivo* condition where the lipid layer faces the blood stream. Every AFM image was taken after gently replacing Tris buffer in the enclosed fluid cell by injecting the new Tris buffer through the input pipe and ejecting the existing tris buffer ejected through the output pipe in order to clean the residue of POPC which did not form bilayers on the surface.

As expected from the previous hexagon μ CP experiment, the AFM image clearly showed the formation of POPC lipid mono- and bilayers on CH₃- and OH-terminated SAM. The difference in height between these two SAMs was under 0.3 nm (Figure 3-14 (a)). However after 15 minutes incubation, the height difference increased as shown in Figure 3-14 (b). After 3 hours of POPC incubation, a more defined height difference, approximately 2 nm (Figure 3-14 (c)) was observed. This suggests that the incubation of POPC vesicle needs a long incubation time (3 hours) to stabilize the POPC layers and to lay all vesicles in the solution down on the surface.

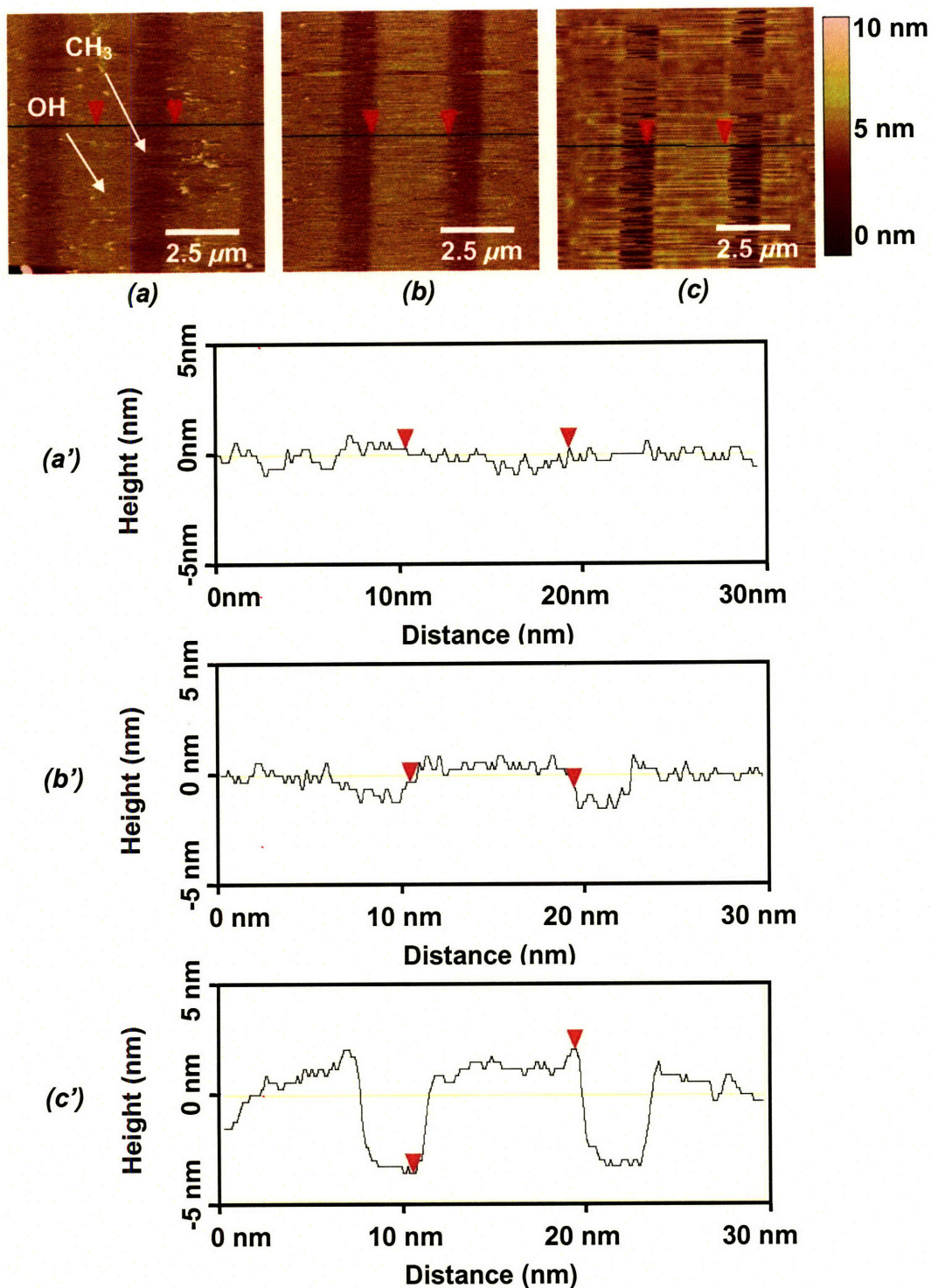


Figure 3-14. AFM height images and section analysis from POPC vesicle incubation (a) & (a') μ -printed OH- (light outside) and CH₃- terminated SAM (dark line), (b) & (b') after 15 min. POPC incubation, lipid bilayer on OH-SAM and monolayer on CH₃-SAM, (c) & (c') after 3 hours POPC incubation.

The 1 μm x 1 μm AFM images of height, deflection and friction were taken using a OH-terminated SAM tip on the POPC incubated OH-terminated SAM in contact mode in 10 mM Tris buffer solution (0.01 M IS, later 0.1 M and 1 M ISs, pH 7.8) with the Pico Force DI AFM (Figure 3-15). In this experiment, 3 hours incubation, which incubation time is similar to Silin's study⁸⁰, was consistently performed to ensure that all the lipids stayed on the surface and the system reached an equilibrium condition. The first image was taken before incubating POPC vesicles. It showed a rougher surface than the POPC incubated images, but was clearly different from the bare gold surface¹¹⁸. After 15 minutes incubation, it showed the stabilized POPC layered surface. However, it is expected that there were some POPC vesicles that had not yet spread out on the surface; on the 15 minutes incubation image, the interference from some residues of lipids in the liquid was observed on the AFM image (Figure 3-15). The AFM image after 3 hours incubation showed some residues of lipids and an irregular surface, but no interference on the AFM image. In order to remove these residues, the same Tris buffer (0.01 M IS) was used to wash the surface and another 3 hours was given to equilibrate the surface again. Lipid bilayer became more homogeneous than before. As the IS increased with 3 hours time intervals for the equilibrium condition, the surface appeared to be more homogenized (figure 3-15). It is assumed that monovalent Na^+ and Cl^- ions played an important role in promoting attraction between the zwitterionic head groups with the higher ionic strength. This result is consistent with that of the high resolution force spectroscopy (HRFS) which will be discussed in more detail in Chapters 4 and 5. The 200 nm x 200 nm AFM images taken with the same condition as above showed clearer difference between the lower ionic strength (0.01 M) and the higher ionic strengths (0.1 M and 1 M) (Figure 3-16). There was no critical height change on the

higher ionic strengths. Even if the POPC layered surface seemed rougher on the 0.01 M IS, it showed homogeneous surface as the scanning size of AFM image decreased (Figure 3-17). This shows that the representative elementary area of the homogeneous lipid layered surface can be changed as the ionic strength increases. This will be discussed later in Chapter 5.

In order to verify that POPC lipids build bilayers not multilayers, a “square test” was performed. Before scanning this 50 x 50 μm AFM image in the 10 mM Tris buffer IS = 1 M, a 10 x 10 μm size AFM image was scanned in the center at a high set point in order to press and broke through the lipid layers. Figure 3-15 shows the square shape left from the 10 x 10 μm scanning, as well as the expected height difference (over 4 nm) for POPC lipid bilayers between the inside and outside of the square. This result is similar to that of Steinem’s study¹⁰². After scanning the 50 x 50 μm area several times, the darkness of foot print, which corresponds to no lipid bilayer, was getting lighter and it disappeared. This result shows “brushing effect” from the AFM probe tip, which helps regularize and clean the surface of the lipid bilayer.

Overall, the AFM images of POPC clearly showed the formation of the POPC lipid bilayers. However, because POPC was in a fluid state at room temperature, POPC bilayer or monolayer image was less homogeneous at lower ionic strengths⁹⁸.

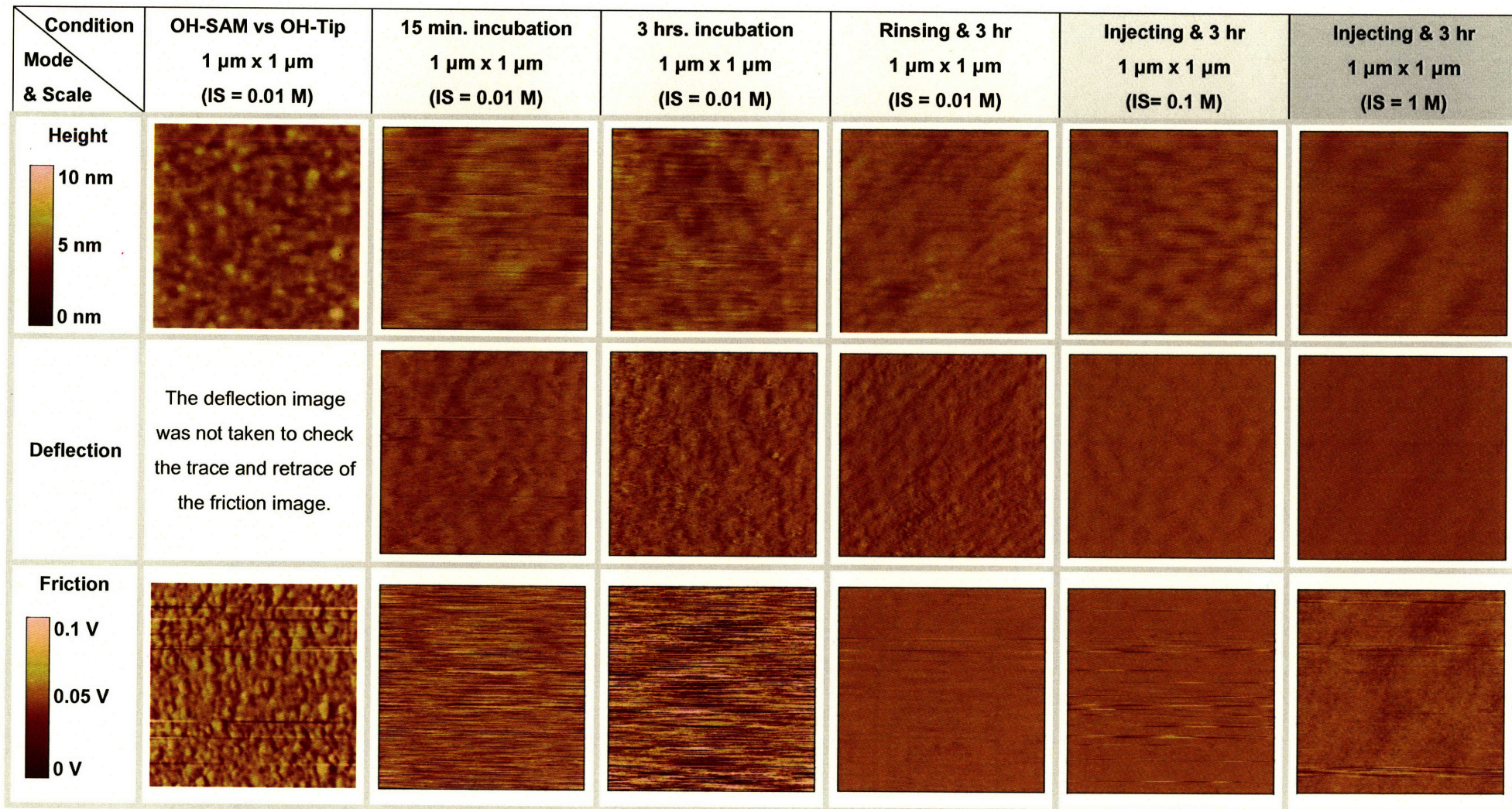


Figure 3-15. 1 μm x 1 μm AFM images for the POPC incubating time intervals (no POPC, 15 minutes, every 3 hr for incubating, rinsing and changing ionic strength) by using OH-terminated tip and OH-terminated SAM.

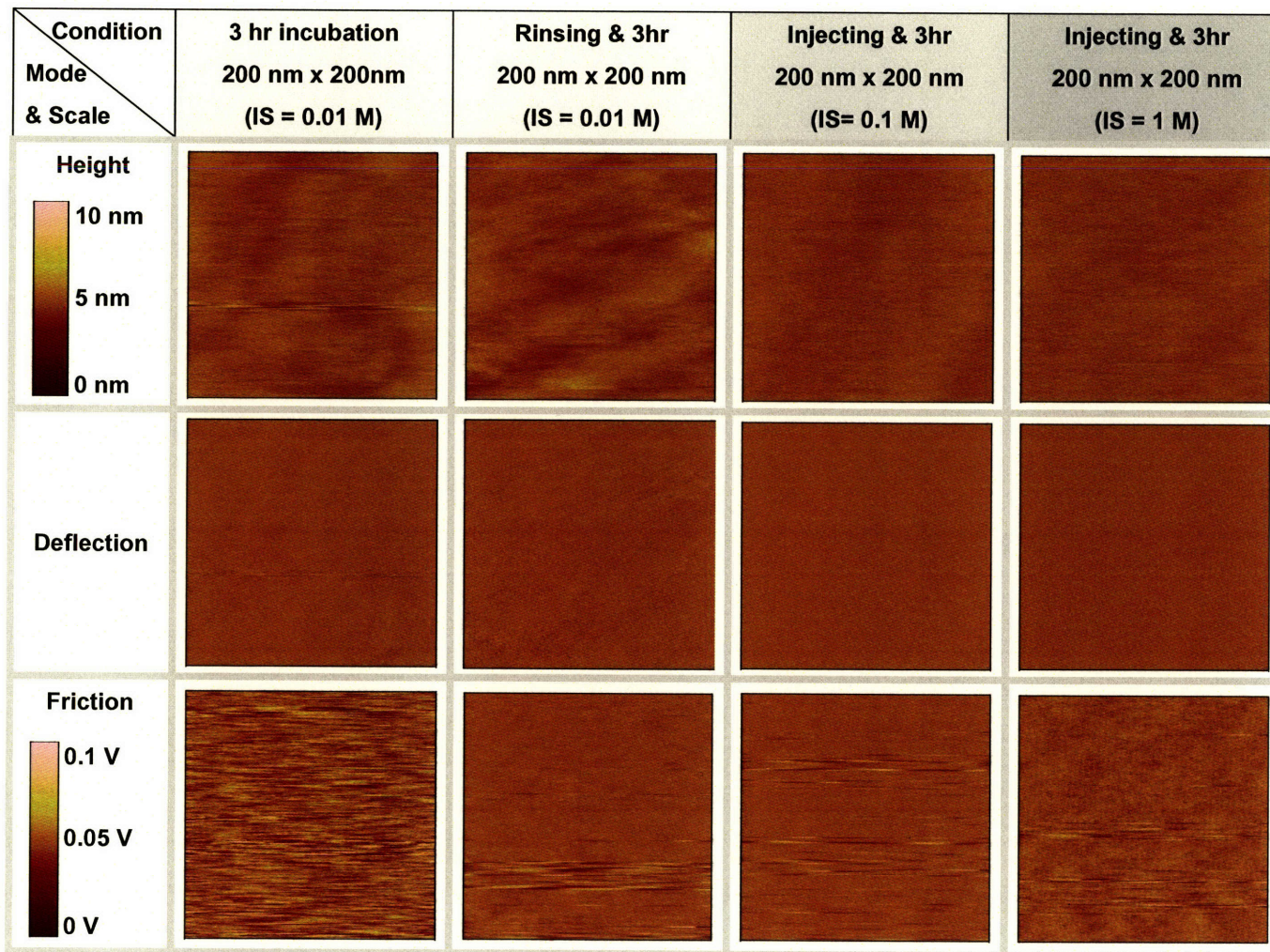


Figure 3-16. 200 nm x 200 nm AFM images for the intervals of the POPC incubating time (every 3 hr for incubating, rinsing and changing ionic strength) by using OH-terminated tip and OH-terminated SAM.

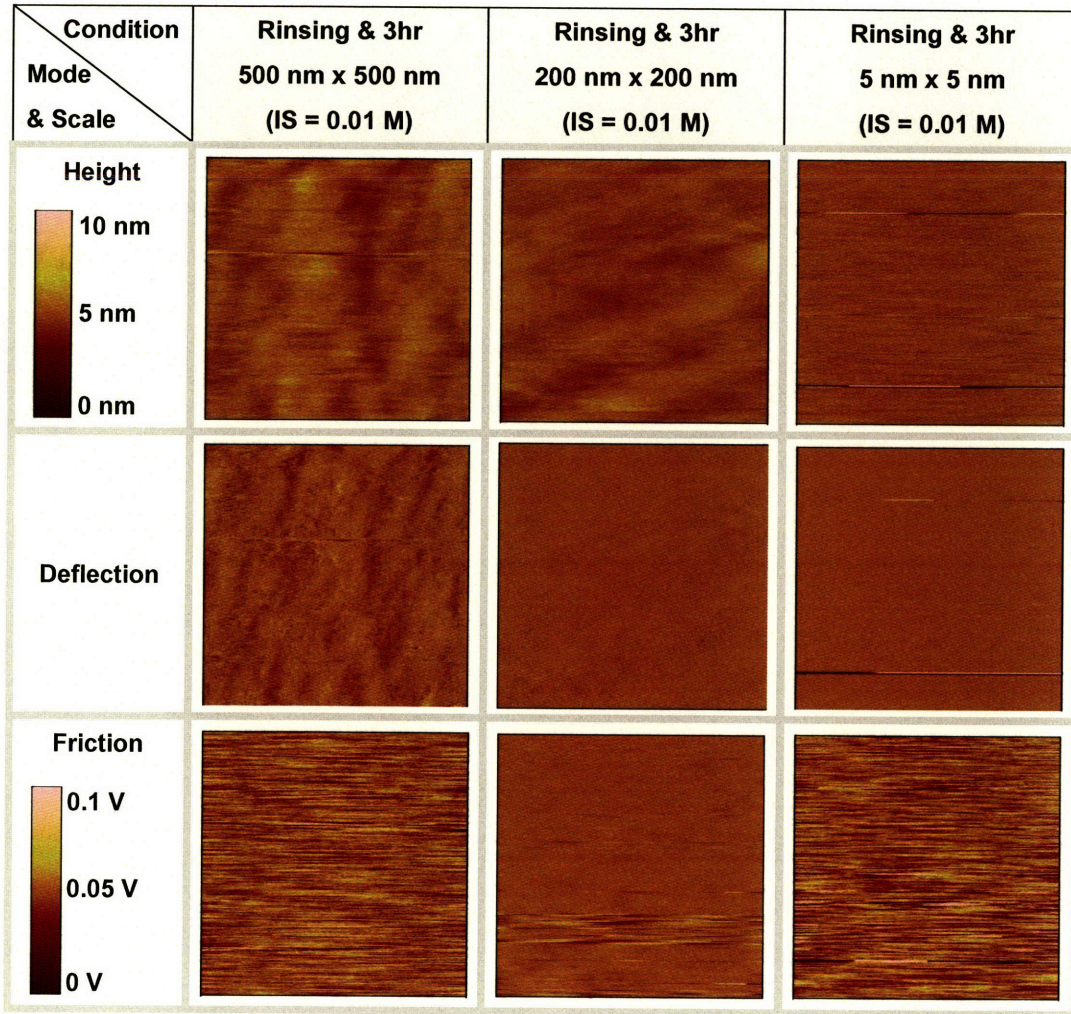


Figure 3-17. Several sizes of images after 3 hr incubation & 3 hr rinsing

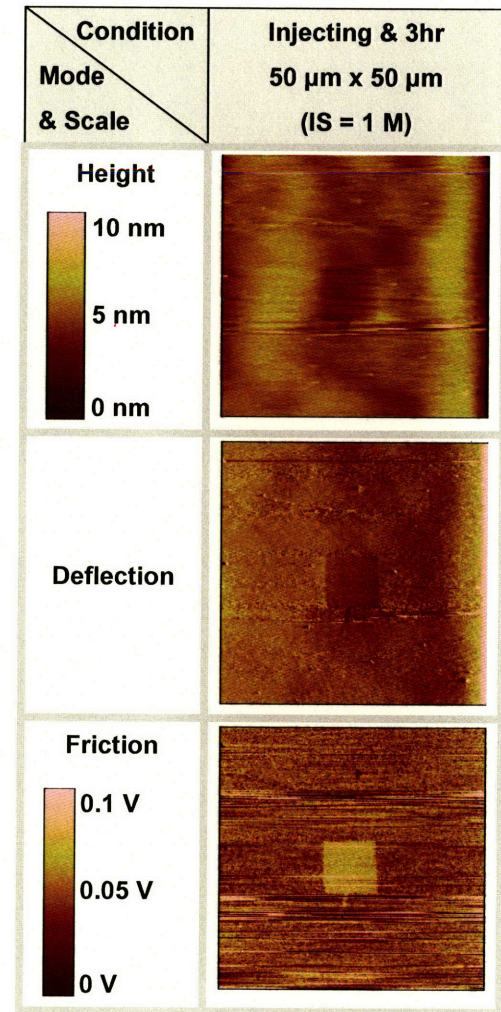


Figure 3-18. AFM images after square test on 1 M IS

After completing the POPC experiments, a DPPC lipid bilayer on mica with DI standard SiN₄ tip was selected as a finalized and simplified model for three reasons. First, DPPC was in gel state at room temperature with a saturated tail, which helps the solid AFM imaging and HRFS experiment. Second, the mica has flatter surface than Au. Third, SiN₄ tips are less likely to have lipids on the surface because the upgrade direct deposit method is used.⁴⁵ This method does not incubate the lipid on the surface with the tip and the surface together and it will not allow lipids to incubate on the tip's surface.

3.3 1,2-Dipalmitoyl-sn-Glycero-3-Phosphocholine (DPPC)

3.3.1 Sample Preparation

In order to prevent the formation of the lipid layer on the tip and create a flat surface on the targeted area, an “upgraded direct deposit method,” an improved form of the old direct deposit method⁹⁸, was attempted and successfully optimized for achieving a homogeneous DPPC bilayer region. This method ensured a consistent deposition and distribution of lipids on the targeted area, with a consistent amount of DPPC solution because the same amount of droplets (7μl / droplet) were spread across the targeted area (Figure 3-19). The sizes of the targeted areas were the same and had no markings or walls because the thin layered mica was naturally fixed to the plastic surface by adding small amount DI water drops between them (Figure 3-19 (a)); this plastic surface had equally spaced holes of equal size. These drops were spread out not only to fix the mica on the plastic surface for over one day but also to make slight physical barriers between the inside and the outside of holes (Figure 3-19 (b)). When the DPPC solution dropped down to each position of the mica, with a hole on the plastic, this hole could be seen

because the mica is transparent. This drop did not move beyond the hole area because the inside of the hole did not have any support from the plastic surface. In addition, the mica inside the hole slightly deflected until the solution dried out (Figure 3-19 (c)). This slight deflection disappeared quickly because the ethanol + chloroform (1:1) dried out quickly and during this time, the sonicated vesicle lipids were adjusted to bilayer form to bilayer forms under the proper density per area (Figure 3-19 (d)). This new procedure was developed for this study.

The summary of the procedure is as follows. 100 $\mu\text{g/ml}$ of DPPC (ethanol + chloroform 1:1) solution was prepared and sonicated for 10 minutes (3 times) with extensive stirring between sonicating intervals. DPPC solution (about $7\mu\text{l}$ per drop) was dropped onto the mica surface. The solution was allowed to evaporate for over 16 hr in the hood. This dried sample was gently cleaned with 500 μl deionized water (3 times) and left in the AFM stage for 1 hour with solution.

One interesting observation of the direct deposit method is that, at higher concentrations of DPPC solution, over 100 $\mu\text{g/ml}$, the lipid bilayer could also be observed in some regions even if multi-layers were observed in other regions. This means that at higher concentrations of DPPC solution, the well-ordered lipid bilayer confined by multi-layers on the boundary can be made via the direct deposit method. This is different from the island of the lipid bilayer found at lower concentrations and similar to *in vivo* conditions in which homogenized confinement exists in all directions.

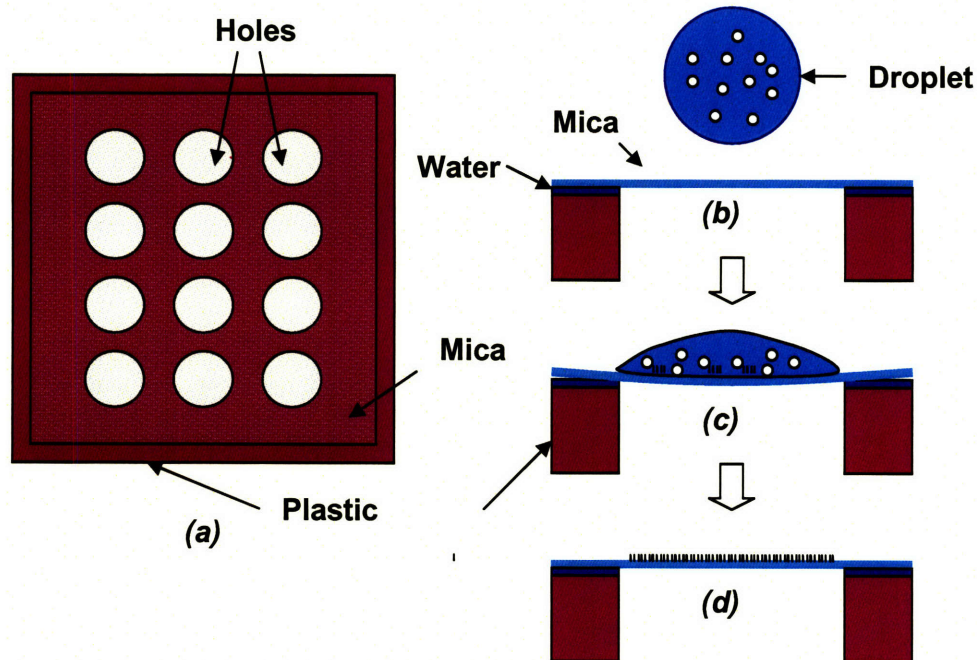


Figure 3-19. Setup and procedure of direct deposit method (a) setup, (b) before dropping, (c) immediately after dropping, (d) after drying out.

3.3.2 Selection of AFM probe tips

Several types of AFM probe tips such as Veeco DNP (spring constant: 0.06 N/m), Veeco DNP-S (sharpened) (spring constant: 0.06 N/m), μ masch sting tip (spring constant: 0.12 N/m), and Vista (spring constant: 0.06 N/m) were used to obtain finer AFM images (Figure 3-20). Among these tips, the DNP tip, DNP-S tip and μ masch sting tip were continuously used for overall experiments reported in Chapters 3, 4, and 5.

3.3.3 Experimental Method

Atomic force microscopy (AFM) was used primarily in the contact mode with all kinds of tips listed in section 3.3.2. All experimental methods and setups for DPPC were the same as those used for POPC as described in section 3.2.2.

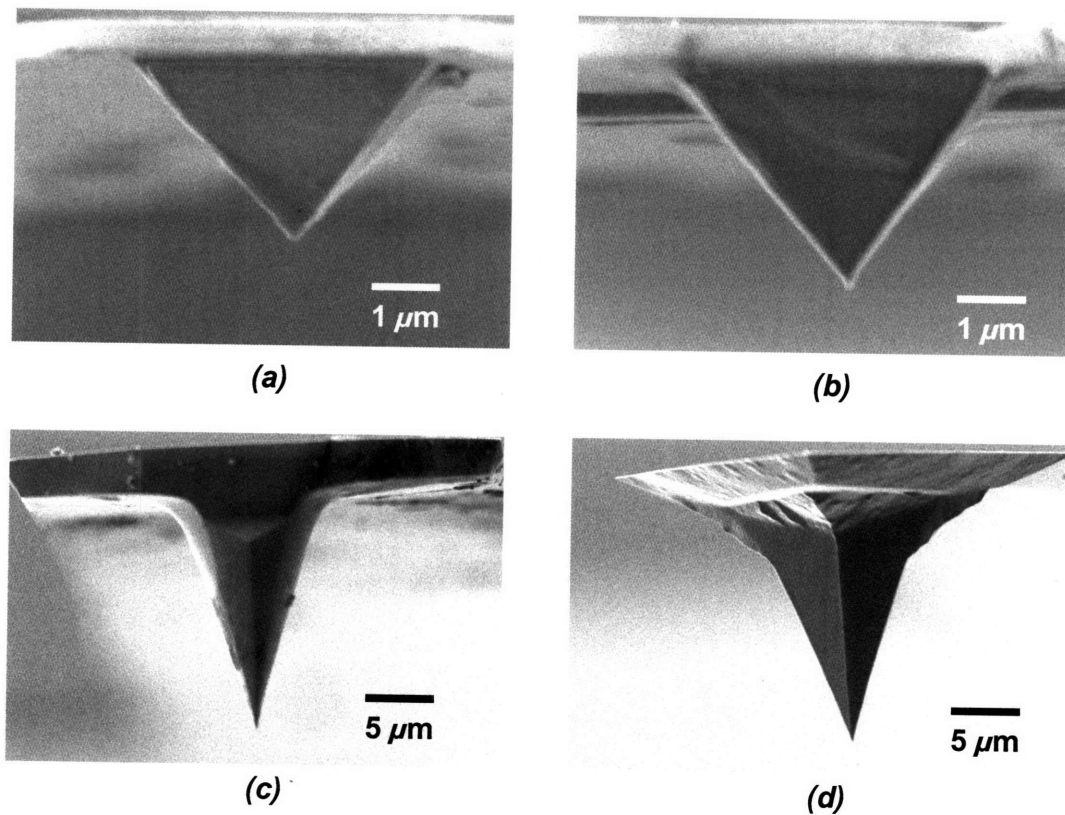


Figure 3-20. Tip images from scanning electronic microscope (SEM). (a) Veeco DNP tip, (b) Veeco DNP-S (sharpened) tip (spring constant: 0.06N/m), (c) μ masch sting tip, and (d) Vista tip.

3.3.4 AFM Imaging Results and Discussion

The upgraded direct deposit method was more effective than the vesicle fusion technique in creating well-distributed, planar lipid bilayer surfaces on the targeted area (Figure 3-21). Interestingly, the DPPC lipid monolayer can be observed clearly on the boundary of the lipid bilayers. This is a unique observation, one that has never been reported before. The images (Figure 3-21) and section analyses (Figure 3-22) clearly show the formation of a lipid monolayer. The height differences between the mica and the DPPC lipid monolayer are about 2.4 ± 0.3 nm, while between the mica and the DPPC lipid bilayer, the difference is about 4.5 ± 0.3 nm (Figure 3-22). One more

interesting observation from this analysis is that for all section profiles on the surfaces of DPPC layers in Figure 22, the height difference, ± 0.3 nm, on the surface of the lipid bilayer is consistent. In the beginning of this imaging experiment, the height difference was expected to be the periodic error from AFM but the error was not periodic for all section profiles. Another possible interpretation [of what?] is that this height difference was caused from the variation in the number of water layers on each lipid bilayer's region. A recent AFM image by Fukuma et al.¹⁰⁵ shows the frequent height changes (the difference, 0.29 ± 0.03 nm) on one domain of the lipid bilayer; this represents a jump from one lipid bilayer region, with just one water layer, to another lipid bilayer region with two water layers.

For the major imaging experiments, a Veeco DNP-S (sharpened) probe tip, which is pyramidal with an end radii of $R_{tip} \sim 10$ nm (normal) – 40 nm (maximum) was used (Figures 3-21 & 22). It is assumed that this well-defined tip facilitated the observation of the lipid monolayer at the boundary of the lipid bilayer, along with a lower scan rate; this result was not observed when the DNP probe tip, which is pyramidal $R_{tip} \sim 20$ nm (normal) – 60 nm (maximum), was used. The rigid gel state of the DPPC lipid layers at room temperature, which is different from the fluid state of the POPC lipid layers at room temperature, may also have enabled this observation. In addition, the upgraded direct deposit method raises the possibility of a lipid monolayer on the boundary of the lipid bilayer rather than resulting from the vesicle fusion method. In vesicle fusion, the lipid bilayer exists when it is a vesicle. Therefore when the vesicles rupture and fuse to the flat mica surface, a lipid bilayer consistently forms. However, in the direct deposit method, the boundary of the lipids bilayers will be affected when the solution (1:1 chloroform and ethanol) dries out and forms the lipid

again after adding Tris buffer (As discussed in Chapter 3.3.1); It is expected that the DPPC forms lipid bilayers when the bilayer vesicle solution (1:1 chloroform and ethanol) stays on the mica surface before drying out.

In order to verify if there are other layers, the square test was performed in the middle of the image (Figure 3-21 (a) & 22 (a)) with a high set-point on the AFM. One interesting result not observed for POPC is that a DPPC lipid bilayer, which was eliminated by the square test, partially recovered (Figure 3-21 (a) & 22 (a)); at some region of the square, lipid bilayers fully recovered but not in other regions of the square. This result was consistent for all DPPC imaging experiments, even if the sample and tip types were changed. When the DNP-S probe tip was changed to a μ masch sting probe tip, which is conical with a smaller end radii ~ 5 nm, more DPPC bilayers were recovered than when the DNP-S probe tip was used (Figure 3-22 (c)). Because of these recoveries from the square tests by the DNP-S and μ masch sting probe tip, we know that recovery of the lipid bilayer is fast enough to perform high resolution force spectroscopy (HRFS) on the same position of the lipid bilayer many times, which will be discussed in Chapters 4 and 5. This recovery was also observed in other experiments of HRFS⁹⁸ and AFM images¹¹⁹. After several square tests and HRFS discussed in Chapters 4 and 5, the end radii of all tips were measured by a scanning electronic microscope (SEM). All the tips were worn out to a certain degree but the surface was smooth enough to perform AFM imaging and HRFS. The maximum radii of DNP, DNP-S and μ masch sting probe tips were $R_{tip} \sim 80$ nm, $R_{tip} \sim 50$ nm, $R_{tip} \sim 30$ nm respectively. These tips were used for the high resolution force spectroscopy (HRFS) experiment described in Chapters 4 and 5.

Another AFM image was taken using a Vista tip, which is conical with the end

radii, $R_{tip} \sim 10$ nm also showed the clear formation of the DPPC lipid bilayer (Figure 3-23 (c)). At a higher IS (0.1 M), the AFM image by DNP-S tip clearly shows the formation of the DPPC bilayer. Clearer bilayer images are observed more on the larger area at higher ionic strengths than at lower ionic strengths (Figure 3-23 (a) & 3-24). When the Tris buffer was changed from 0.01 M to 0.1 M, some debris was observed (Figure 3-23 (a)), but disappeared after several scans.

It was very clear that the upgraded direct deposit method played a critical role in obtaining the homogeneous DPPC lipid bilayers even if there were some holes in the lipid bilayers. This area is large enough to perform high resolution force spectroscopy (HRFS) at several positions without considering the boundary effect from holes and deformation effect from other positions of the HRFS experiment. Some holes on the overall area of lipid bilayers in the 0.01 M IS were also observed by others¹⁰⁴.

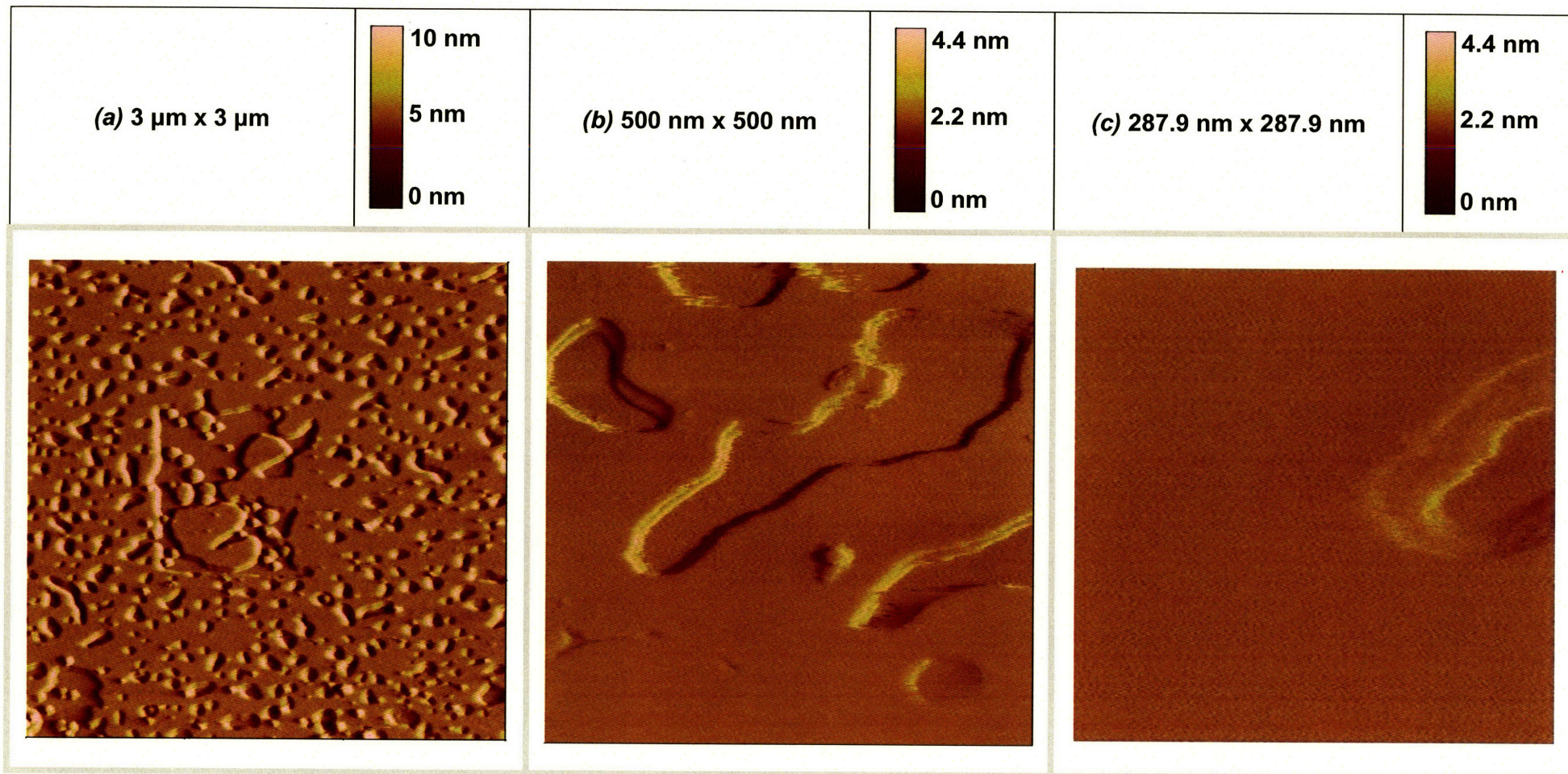


Figure 3-21. AFM deflection images of DPPC lipid bilayer and monolayer on the boundary of bilayers. (a) 3 μm x 3 μm (the “square test” was performed in the middle of the left image), (b) 500 nm x 500 nm, and (c) 287.9 nm x 287.9 nm. AFM images on (b) and (c) are from the randomly selected area of (a). AFM images on (b) and (c) were not exposed to the square test. DNP-S (sharpened) tip was used with the low scan rate (under 0.8Hz) in 10mM tris (hydroxymethyl) aminomethane buffer (0.01M IS, pH 7.6). Sample was prepared by direct deposit method.

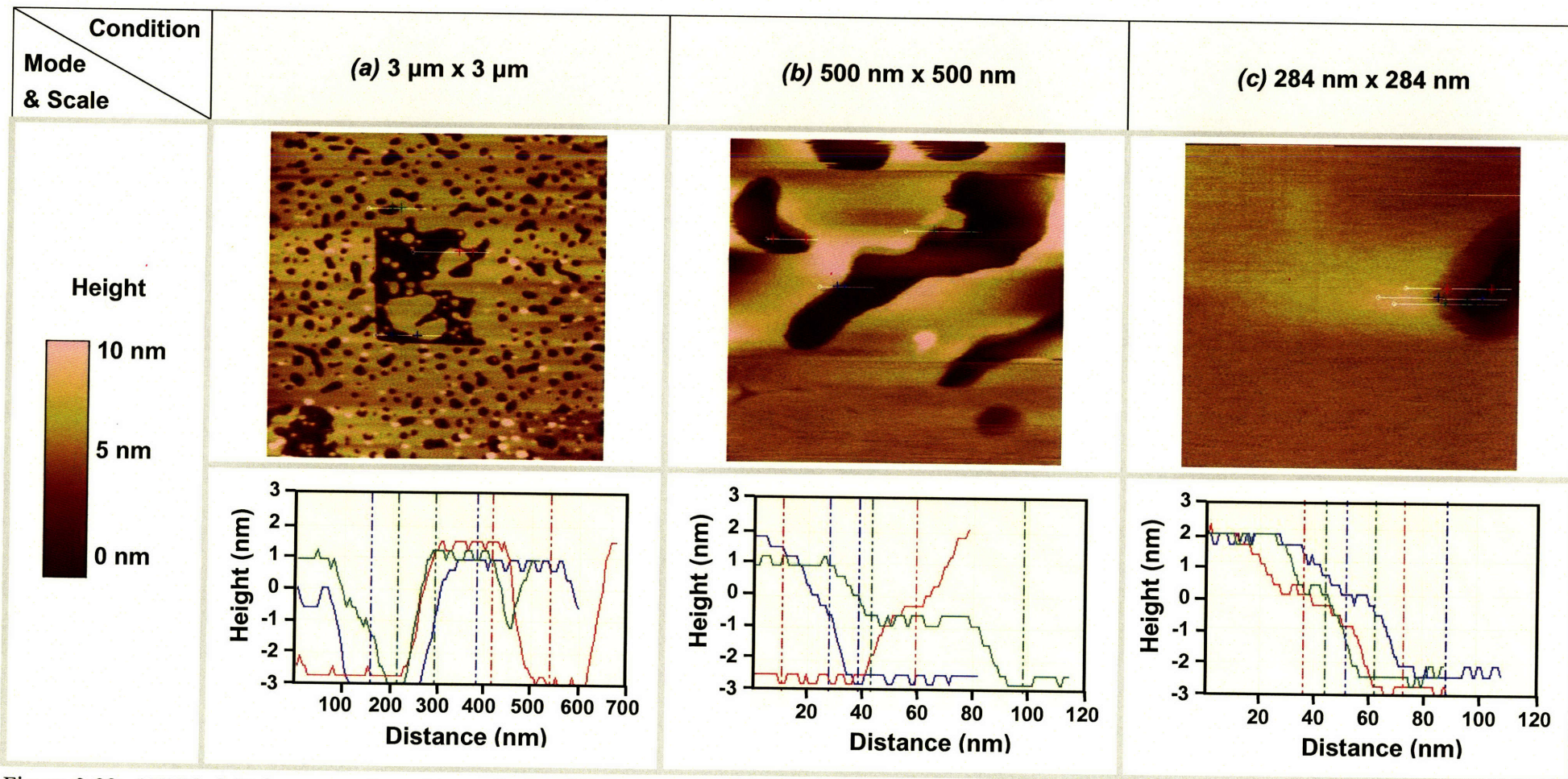


Figure 3-22. AFM height images and section analysis of lipid bilayer and monolayer on the boundary of bilayers. (a) 3 μm x 3 μm (the “square test” was performed in the middle of the left image), (b) 500 nm x 500 nm, and (c) 287.9 nm x 287.9 nm. Images are the same as those in Figure 3-17. DNP-S tip was used with the low scan rate (under 0.8 Hz) in 10 mM tris (hydroxymethyl) aminomethane buffer (0.01M IS, pH 7.6). Sample was prepared by the upgraded direct deposit method.

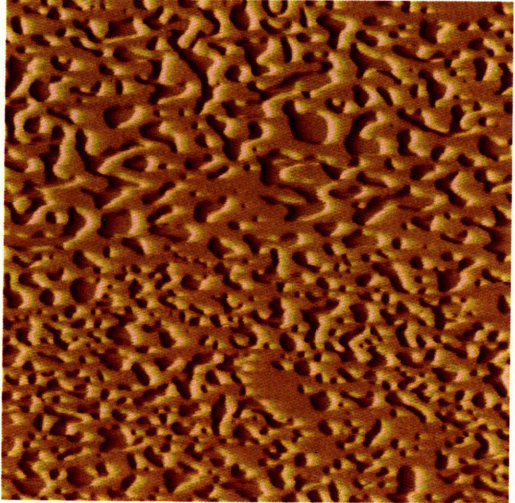
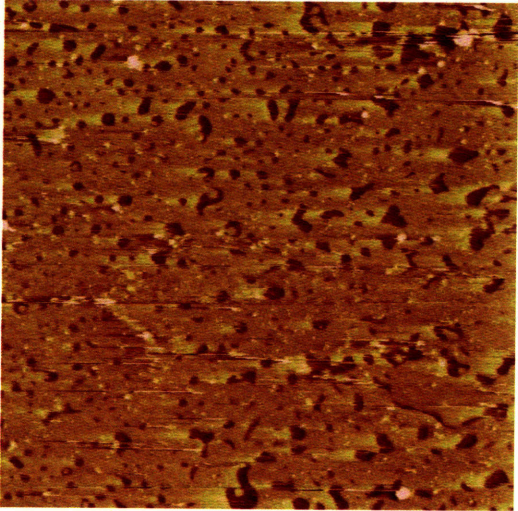
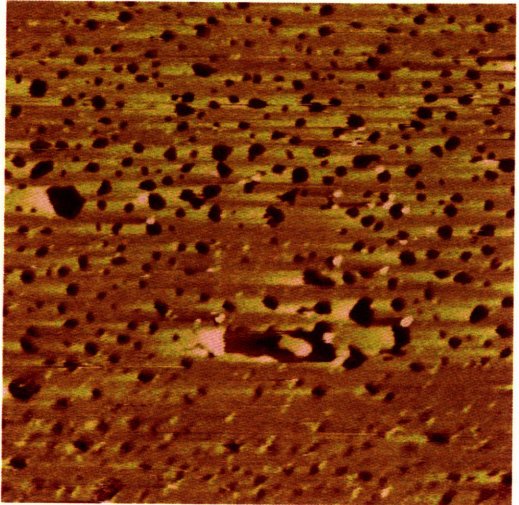
Condition Mode & Scale	(a) 5 μm x 5 μm	(b) 5 μm x 5 μm	(c) 5 μm x 5 μm
Deflection			

Figure 3-23. AFM images of lipid bilayer by (a) 5 μm x 5 μm by using DNP-S (sharpened) tip on 0.1M IS, (b) 5 μm x 5 μm by using Vista tip on 0.01 M IS (the end radii of the tip is under 10 nm diameter), and (c) 5 μm x 5 μm by using μmasch Sting tip on 0.01M IS. Tips were used with the low scan rate under 0.8 Hz. Sample was prepared by the upgraded direct deposit method. 10 mM Tris buffer was used.

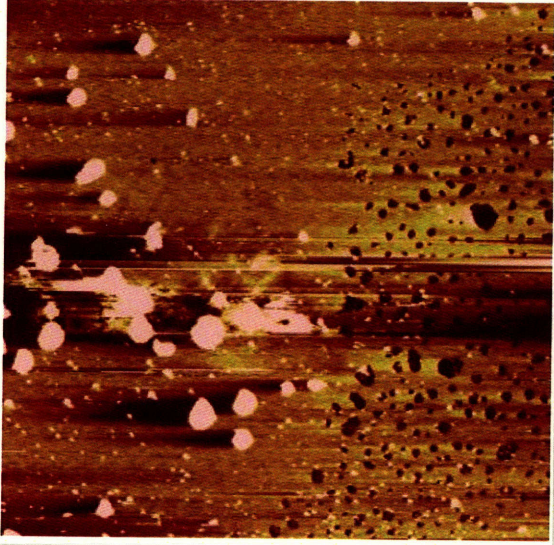
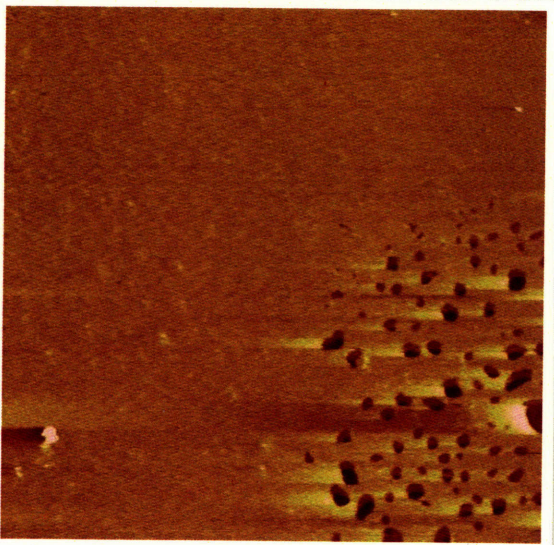
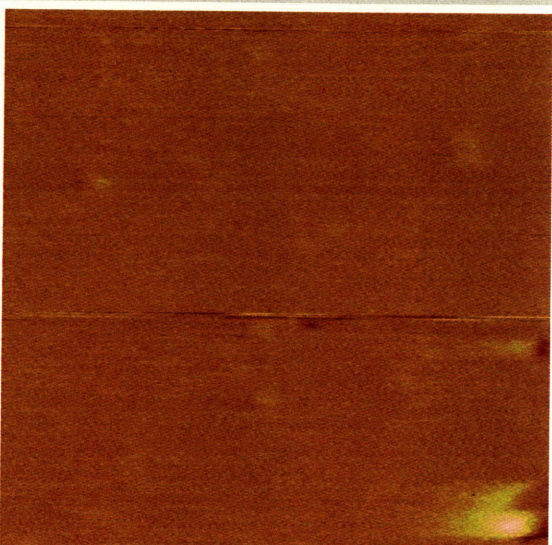
Condition Mode	(a) 7.5 μm x 7.5 μm	(b) 5 μm x 5 μm	(c) 1.2 μm x 1.2 μm
Deflection			

Figure 3-24. AFM images of the lipid bilayer by using an μmasch Sting tip after changing IS from 0.01M to 0.1M. (a) 7.5 μm x 7.5 μm , (b) 5 μm x 5 μm , and (c) 1.2 μm x 1.2 μm . Scanning images continuously from (a) to (c) made the surface more homogeneous. The debris (white spots on (a)) after changing from 0.01 M to 0.1 M ionic strength buffer disappeared after several scans. The low scan rate (under 0.8 Hz) was used in 10 mM tris (hydroxymethyl) aminomethane buffer (0.1 M IS, pH 7.6). This sample was prepared with the upgraded direct deposit method.

3.4 Conclusion

In this study, POPC and DPPC layers were made using vesicle fusion technique and the upgraded direct deposit method. The formation of stable lipid layer by vesicle fusion technique required long incubation time in AFM (here, 3 hr). However, the upgraded direct deposit method spent just on 1 hr in AFM to make the sample ready for the AFM experiment.

This upgraded direct deposit method is effective in making a consistent deposition and distribution of lipids on the targeted area with a consistent amount of DPPC solution because a consistent amount of droplets (7 μ l / droplet) are spread out on the targeted area. This upgraded direct deposit method enabled us to observe the clear lipid bilayer and monolayer (right next to the boundary of bilayer) together, which have never been reported together before. It is expected that the nature of the upgraded direct deposit method contributes to stabilizing the lipids on the flat mica surface, and enables a monolayer to form right next to the boundary. In addition, the upgraded direct deposit method played a critical role in obtaining the homogeneous DPPC lipid bilayer which is large enough to perform high resolution force microscope (HRFS) at the several positions in Chapters 4 and 5, without considering the boundary effect from holes and deformation effect from other positions of the HRFS experiment.

To verify if these are only lipid mono- or bilayers not multilayers, the square test was performed in the middle of the image. It was observed for the first that some DPPC lipid bilayer area which was eliminated by the square test partially recovered.

The existence of hydrogen bonded water layers on the surface could be expected from the section analysis of DPPC bilayer. As the ionic strength of solution increased, the surface of lipid layers were more homogeneous. Based on these

characterizations of the lipid layers, POPC and DPPC layers were ready for the HRFS experiment as described in Chapters 4 and 5.

CHAPTER 4

High Resolution Force Spectroscopy of Lipid Bilayers as a Function of Solution Ionic Strengths (ISs)

4.1 Introduction

Biological membranes play important roles such as sustaining a stable and non-clogging barrier from electrolyte solutions and transporting proteins from outside to inside of the cell. Lipids, which form the bilayer, are the main component of biological membranes, along with steroids and proteins; lipids also play a significant role in stabilizing membranes.

To understand the interaction mechanisms of biological membranes such as mechanical forces caused in cell-to-cell interactions (red blood cell vs. endothelium cells, or the penetration of proteins through cell membranes) and to develop a protein-resistant and versatile cell-membrane mimetic model system for blood-contact biosensors and biomedical devices,⁷⁶ it is crucial to study the nanomechanical properties and interactions of hydrated lipid bilayers for several ionic strengths. For the protein-resistant applications, one of the most important factors is that lipid bilayers should be homogeneous across the entire surface to prevent clogging or coagulation in the holes and strong enough to endure high blood pressure as discussed in section 2.2.

Previous high resolution force spectroscopy (HRFS) experiments using nanomechanic techniques such as the surface force apparatus (SFA), scanning force microscope (SFM), and atomic force microscope (AFM), have shown that the nanoscale compressibility and statistical distribution of one or two yield threshold forces (rupture or fusion forces) are needed to penetrate a lipid mono- or bilayer (so-called “yield

threshold forces”).^{103,120,121,122,123,124} HRFS at different ionic strengths (ISs)¹⁰³ or pHs¹²⁵ and lateral force microscopy (LFM) (as a function of different ISs¹²⁶) have been applied to lipid bilayers using a silicon nitride (Si_3N_4) tip or a chemically functionalized tip. One key result that is consistent across these experiments is that as the IS increases, both the yield threshold forces in the vertical HRFS to the lipid bilayer and the vertical force needed to break the lipid bilayer laterally in the LFM also increase. This can be explained by the screening and tighter packing effect of Na^+ and Cl^- ions on the charges of the zwitterionic lipid head groups^{103,125} (Figure 4-1). The positively charged nitrogen choline of the head group may be screened by the Cl^- group and the negatively charged phosphate phosphorus of the head group is screened by Na^+ . These ions also screen other polar head groups in the same manner and this screening effect helps to increase the lateral interaction of the head group and to tightly pack the lipids. Theoretical approaches such as the simple spring model, which considers the lateral forces, and the macroscopic Hertz model have also tried to show the increase of forces (before the force reaches the yield threshold force of rupture¹⁰³) when the AFM tip deforms and disrupts the surface. These studies have been aimed to better understand the rupture mechanism of the lipid bilayer via HRFS¹²⁷. The Hertz model is not well suited for the experimental results because it is the macroscopic model, but the spring model works well on the

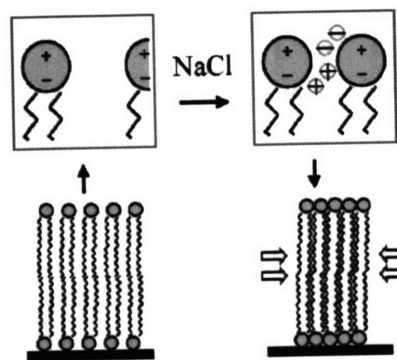


Figure 4-1. Effect of NaCl in lipid molecule packing.¹²⁵

elastic deformation of the lipid layer.

When examining the previous research on HRFS, and the interaction between two lipid bilayers or one lipid bilayer surface and a AFM probe tip, two regimes can be identified: (a) *a noncontact interaction regime*, which may include contributions from longer range surface forces (e.g., electrostatic force, van der Waals force) to shorter range surface forces (e.g., hydration force) and is highly dependent on the functionality of the head groups (b) *a contact interaction regime*, which includes steric compressibility and, in addition to the other noncovalent interactions listed above for the noncontact regime, hydrophobic interactions that derive from the lipid's tail group. The hydrophobic interaction of the tails maintains the structure of the layer until the tip thoroughly penetrates the layer. However, the precise mechanisms of fusion and rupture of the lipid layers are unknown and various studies^{103,119,123} have not had consistent results using HRFS on the same or similar structures of the lipid bilayer.

To clearly understand the nanomechanical properties of lipid bilayer, high resolution force spectroscopy (HRFS) was performed for the two kinds of lipid bilayers. At the start of this research, 1-palmitoyl-2-oleoyl-*sn*-glycero-3-phosphocholine (POPC, unsaturated tail) lipid bilayers and monolayers on both hydrophilic OH-terminated SAMs and hydrophobic CH₃-terminated SAMs, respectively, on the Au-coated tip and surface were tested by using a molecular force probe 1D (MFP 1D) of different ionic strengths (ISs, 0.01 M, 0.1 M, 1M). With some modification and improvement of experimental skills, the 1,2-dipalmitoyl-*sn*-glycero-3-phosphocholine (DPPC, saturated tail) lipid bilayer was also studied via Picoforce's atomic force microscopy of different ionic strengths (ISs, 0.01 M, 0.1 M, 1 M) with bare Si₃N₄ AFM probe tip. Because DPPC is a gel at the room temperature (the transition temperature from a gel to a fluid is

about 60°C⁹⁸), it has a more stable and rigid lipid bilayer at room temperature. This makes the result of the nanomechanical test more consistent and reliable than that of POPC, which is a fluid at room temperature (the transition temperature from a gel to a fluid is -6°C⁹⁷). In this research, only a solid support was used to achieve the nanomechanical properties of lipid layers without an effect from the soft surface.

4.2 1-Palmitoyl-2-Oleoyl-*sn*-Glycero-3-Phosphocholine (POPC)

4.2.1 Sample Preparation

The sample preparation is the same as was used in preparing the AFM imaging of lipid bilayer in the chapter 3. The POPC vesicle fusion technique⁴⁴ was optimized in order to prepare the lipid bilayer for the HRFS experiments. A 0.6 mL POPC in chloroform was dissolved in a 10 mg/mL 9:1 chloroform/methanol solution and the POPC solution was dried by nitrogen. The 6 mg POPC in a chamber was lyophilized for 8 hours. This lyophilized POPC was redissolved in 2 mL of 10 mM of a degassed Tris buffer (150 mM NaCl, pH8). This solution was sonicated and centrifuged. Finally the centrifuged solution was diluted to 2 mM with the Tris buffer.

The vesicle size was checked by using by a particle size analyzer (90 plus particle size analyzer made by Brookhaven Instruments Corporation) in order to maintain the diameter of the POPC vesicle under 100 nm, which helps to eventually distribute the lipid bilayer from the vesicle as was done in chapter 3. This POPC vesicle solution was injected onto the surface of hydrophobic CH₃-terminated SAM (AuS-(CH₂)₁₁-CH₃) to make monolayer or hydrophilic OH-terminated SAM (AuS-(CH₂)₁₁-OH) to make a lipid bilayer. The lipid solution was incubated for at least 15 minutes to establish lipid bilayer.

To prepare the SAM-functionalized planar substrates and probe tips, a gold-coated substrate and a gold-coated Veeco DNP pyramidal silicon nitride tip (spring constant: 0.06 N/m) were incubated for 24 hours in 25 mL of 5 mM solutions, which were prepared using 0.0255 g of 11-Mercapto-undecanol (HS-(CH₂)₁₁-OH, 45056-1) and 30 μ L of 1-dodecanethiol (HS-(CH₂)₁₁-CH₃, 47135-4) in ethanol. Both the 11-mercaptoundecanoic acid and 1-dodecanethiol were purchased from Sigma Aldrich. To insure a clean surface, all the gold-coated tips, and gold substrates were Piranha treated (1:3 H₂O₂:H₂SO₄): 3 seconds for the tips and 5 minutes for the planar substrates, which was done immediately before chemical functionalization.

All nanomechanical tests for POPC were done at room temperature. POPC has a fluid phase in room temperature; the transition temperature to a fluid phase is -6°C⁹⁷.

4.2.2 Experimental Method

A molecular force probe 1D (MFP 1D, Asylum research, Inc.) was first used for HRFS experiments on the POPC bilayer for all ISs experiments. Picoforce atomic force microscopy (AFM, Veeco) was used for the POPC monolayer experiment. AFM imaging was already done as described in Chapter 3 in order to ensure the formation of the lipid bilayer. Three different ionic strengths, 0.01 M, 0.1 M and 1 M, in 10 mM tris (hydroxymethyl) aminomethane buffer (pH 7.6) were used. As mentioned in Chapter 2, three different ionic strengths 0.01 M, 0.1 M and 1 M were selected and adjusted by NaCl. Considering the potential application of lipid layer to the bio-device *in vivo* for a mammalian bloodstream (0.15 M) and the marine structures under sea (0.50 M ~ 0.86 M), 0.1 M and 1 M were selected. While other multivalent ions exist in the bloodstream and seawater, only Na⁺ and Cl⁻, which are main ions in the bloodstream and seawater,

were selected for this study to simplify the experimental environment. In addition, to compare these results to a low IS, 0.01 M was selected.

The schematic of HRFS for monolayers is shown on the next page (Figure 4-2). It was expected that the lipid monolayers would be stabilized on both the CH₃-terminated SAM tip and the Au substrate after 30 minutes of incubation. Another schematic of HRFS for bilayers is shown in Figure 4-3. It was expected that the lipid bilayers would stabilize on both the OH-terminated SAM tip and Au substrate after 30 minutes incubation. These HRFS experiments for the POPC layers were focused on studying the electrostatic interaction, fusion, and rupture of the lipid layers.

For all HRFS experiments, the displacement rate was set to 1 $\mu\text{m}/\text{second}$ and the estimated nominal cantilever spring constant (set by the manufacturer) was about 0.06 N/m. Based on the thermal tune of the AFM, the spring constants of each individual tip were measured directly.

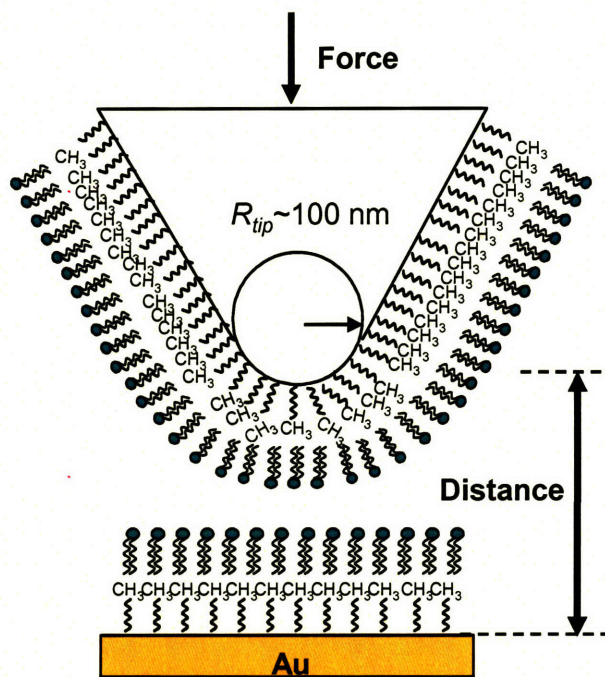


Figure 4-2. Schematic of HRFS experiment involving compression of opposing lipid monolayers; the size of the lipids and CH₃-terminated SAMs are not drawn to scale.

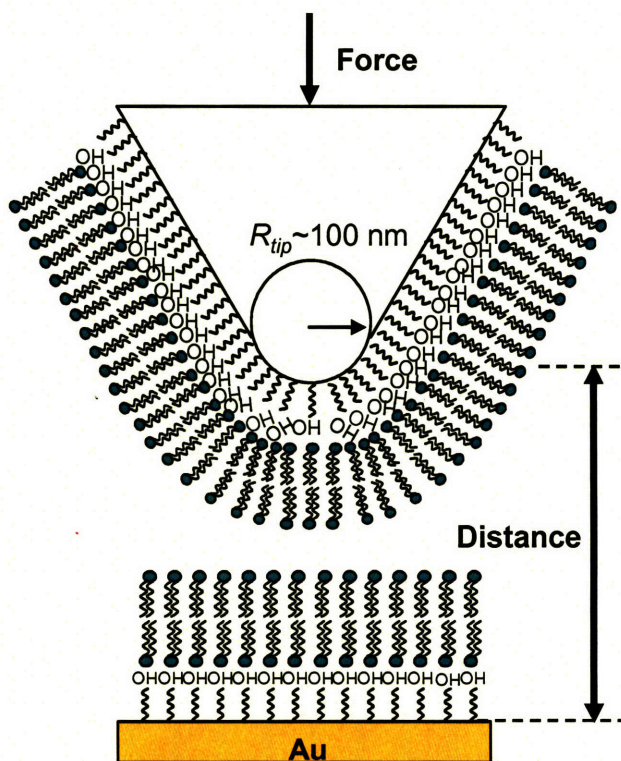


Figure 4-3. Schematic of the HRFS experiment involving compression of opposing lipid bilayers; the size of the lipids and OH-terminated SAMs are not drawn to scale.

4.2.3 Experimental Results and Discussion

HRFS of the POPC monolayer adsorbed on the CH₃-SAM tip on "approach" (probe tip advancing towards surface, Fig. 4-2) to the POPC monolayer adsorbed on an CH₃-SAM planar substrate, using a molecular force probe (MFP), showed a nonlinear net repulsive interaction starting at over 15 nm (0.01 M IS) followed by one or two yield thresholds (Figure 4-4), which was not observed on the HRFS of the bare CH₃-SAM tip vs. the CH₃-SAM control experiment. The second yield threshold forces were clearly distinguished for all experiments but the first lower yield threshold forces were sometimes ambiguous (approximately 30% of data). The second yield threshold forces were quite higher than the first one; on 1M IS, the second yield threshold force were about 6x higher than the first one. Both first and second yield threshold forces increased as the IS was changed from 0.01 M to 1 M (Figure 4-5 & 6). Almost all increases were statistically significant ($p < 0.001$) in the force as IS was changed from 0.01 M to 0.1 M. On the contrary, the first yield threshold distances decreased as the IS increased but the second yield threshold forces were within the same range (Figure 4-5 & 6). It is expected that the final yielding threshold happens almost at the same distance even if the ionic strength increases.

The HRFS experiment on the opposing POPC bilayers which were adsorbed on OH-SAMs in Tris buffer with different ionic strengths, 0.01 M, 0.1 M and 1 M, using a molecular force probe (MFP) on approach (Figures 4-9, 4-10, and 4-11) showed a nonlinear net repulsive interaction starting at over 15 nm and typically was followed by the two threshold forces on 0.01 IS or one threshold force on 0.1 M and 1 M ISs (Figures 4-10 & 11). As the ionic strength increased, the yield threshold forces increased in all experiments for lipid bilayers on both the OH-terminated SAM on tip

and surface (Figures 4-10 & 11). The distance of the initiation of a net repulsive interaction and the yield threshold distances decreased as the ionic strength increased (Figure 4-10 & 11); this is reasonable considering the decrease of the Debye length as the IS increases.

On 0.1 M and 1 M ISs, the second-yield threshold forces of HRFS experiments between the POPC monolayers on the CH₃-SAM tip and substrate were higher than those between the POPC bilayers on the OH-SAM tip and substrate (figures 4,-6 & 10). It is expected that the lipid monolayers were more homogenized on CH₃-SAM tips and surfaces with hydrophobic interaction than the lipid bilayers on OH-SAM tips and surfaces.

For overall POPC experiments, the monovalent Na⁺ and Cl⁻ ions were, as expected, important in making the lipid head groups hold together tightly so the yield threshold forces increased as the ionic strength increased. This can be explained by the screen and binding effect of ions on the charges of the zwitterionic lipid heads.^{103, 125}

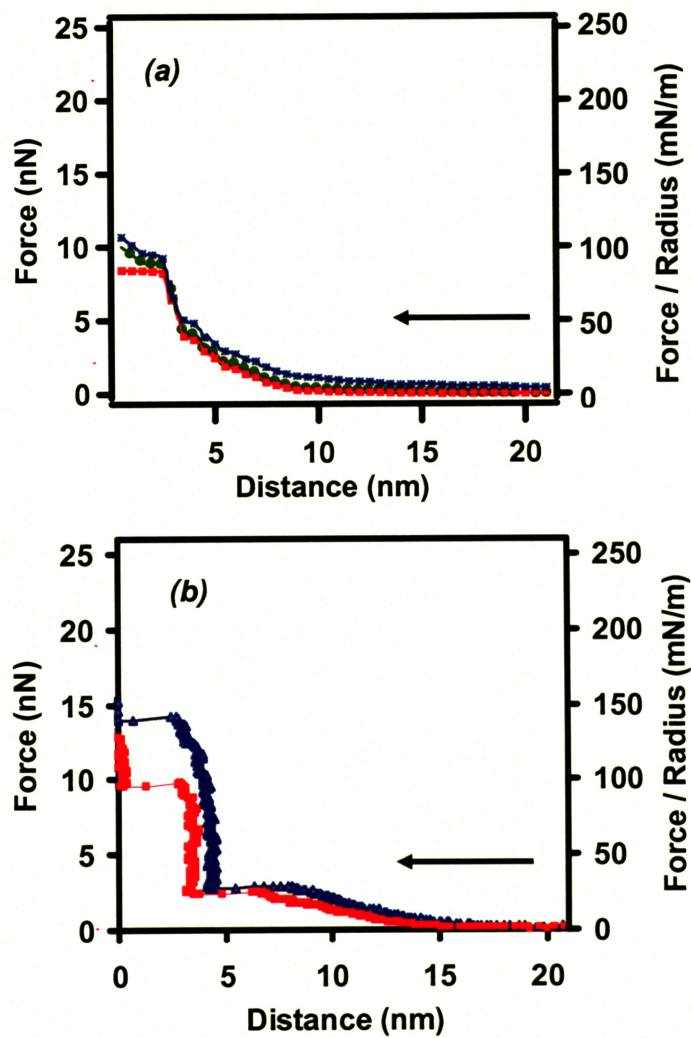


Figure 4-4. Examples of Individual Force-Distance curves on approach of opposing POPC mono layers interaction (Figure 4-2). (a) 0.01 M IS and (b) 0.1 M IS. On 1 M IS, same shape of two yield threshold forces were observed as shown in (b). Only difference is that the yield threshold forces were higher on 1 M IS than on 0.1 M IS.

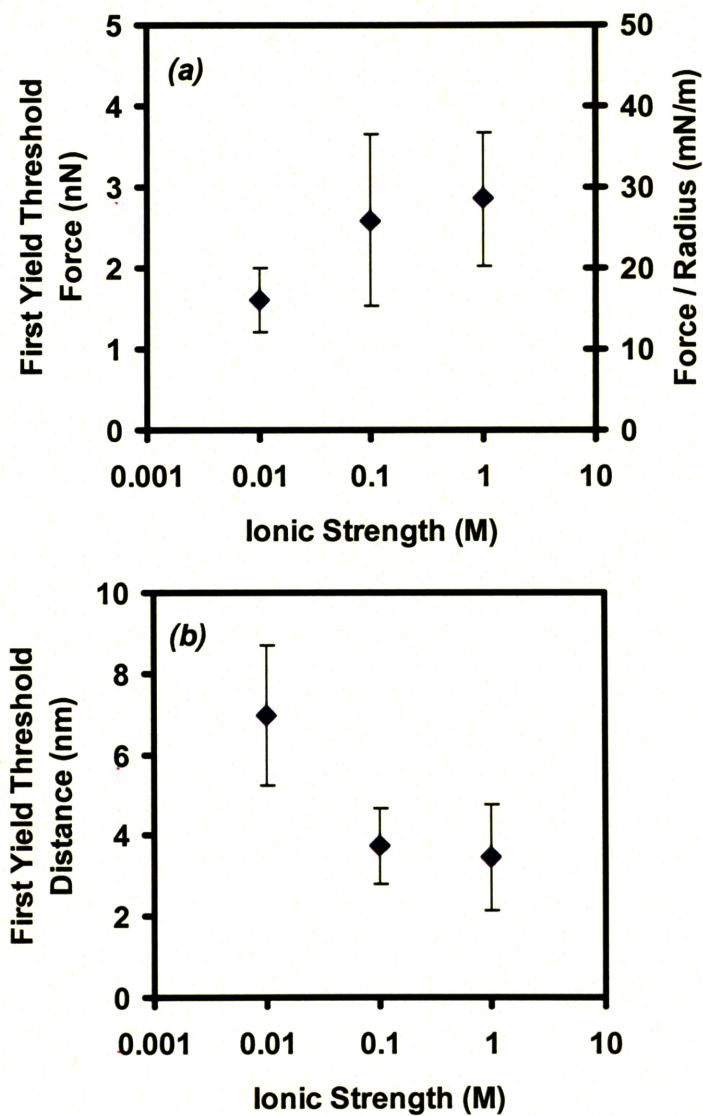


Figure 4-5 Plots on approach of opposing POPC mono-layer interactions (Figure 4-2). (a) Plots of a normalized first-yield threshold force with varying ionic strengths. (b) Plots of the first-yield threshold distance (the initial distance of break-through force) with varying ionic strengths. The difference is considered extremely statistically significant in force and distance as the IS changes from 0.01 M to 0.1 M (force: $p < 0.0003$, distance $p < 0.0001$). or 1 M ($p < 0.0001$).

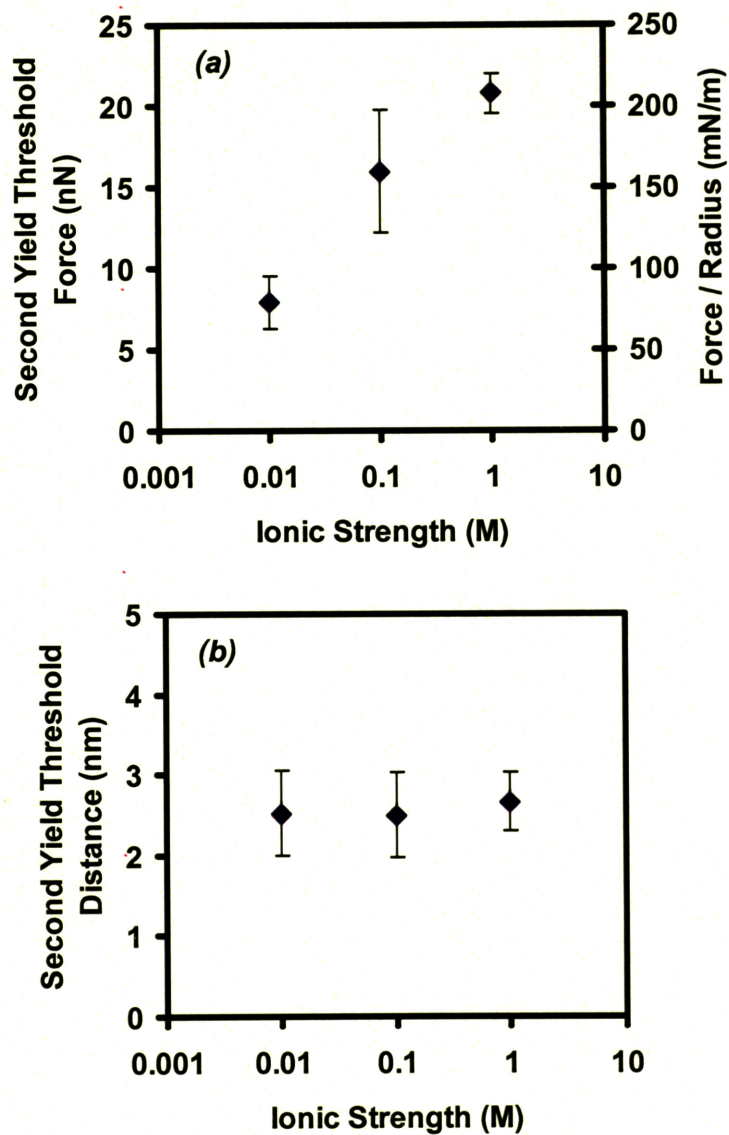


Figure 4-6. Plots on approach of opposing POPC mono layers interaction (Figure 4-2). (a) Plots of a normalized second yield threshold force with varying ionic strengths. (b) Plots of the second yield threshold distance (the initial distance of breakthrough force) with varying ionic strengths. The difference is considered to be extremely statistically significant in the force as IS is changed from 0.01M to 0.1M or 1M ($p < 0.0001$).

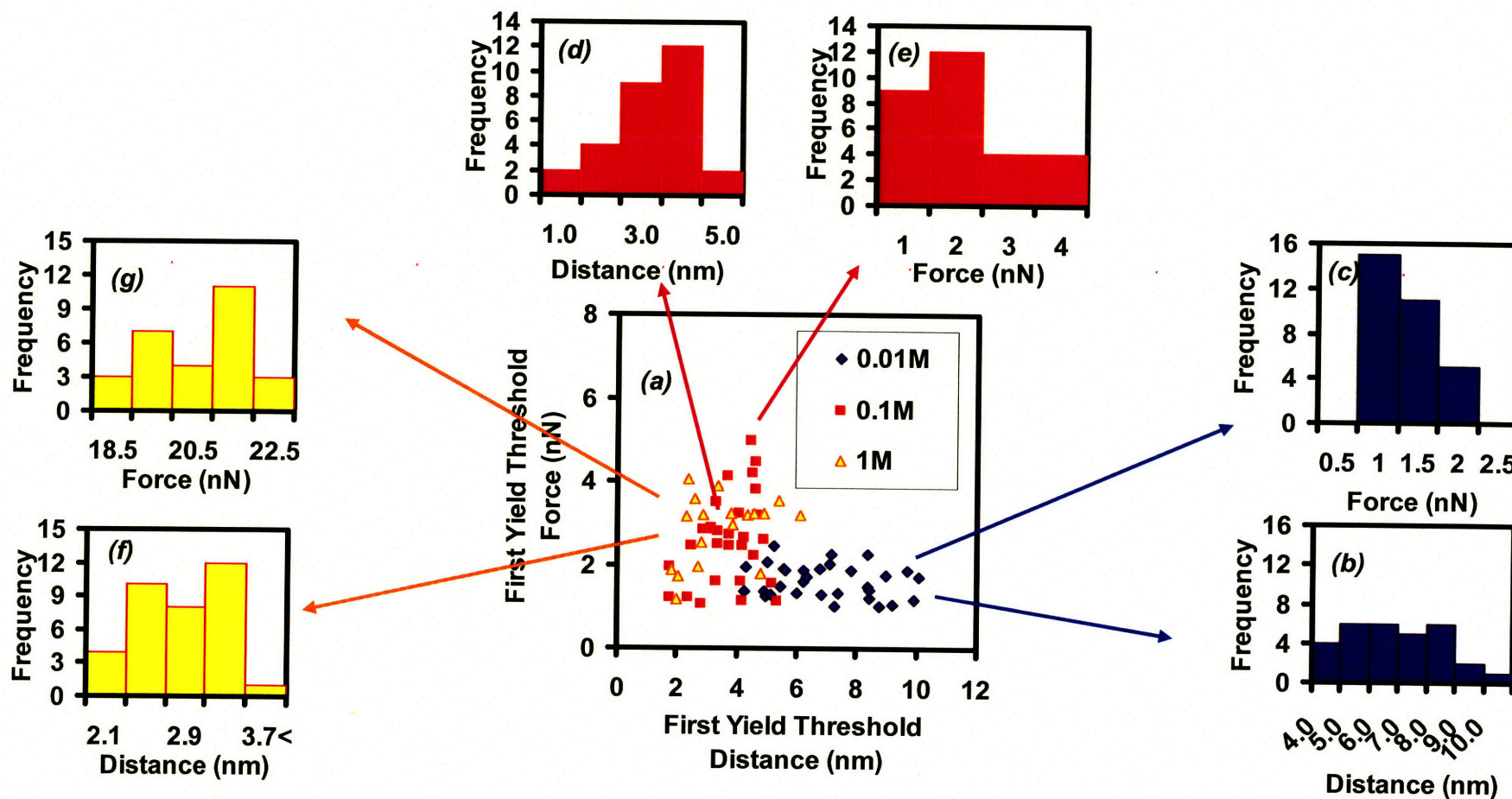


Figure 4-7. 2 Two-dimensional distribution and histograms of nanomechanical test on the approach of opposing POPC mono-layers interaction. (a) Distribution of the first yield threshold distances and forces with varying ionic strengths, (b) & (c) histogram of yield threshold distances and forces with 0.01 M IS (d) & (e); histogram of yield threshold distances and forces with 0.1 M IS (f) & (g), histogram of yield threshold distances and forces with 1 M IS.

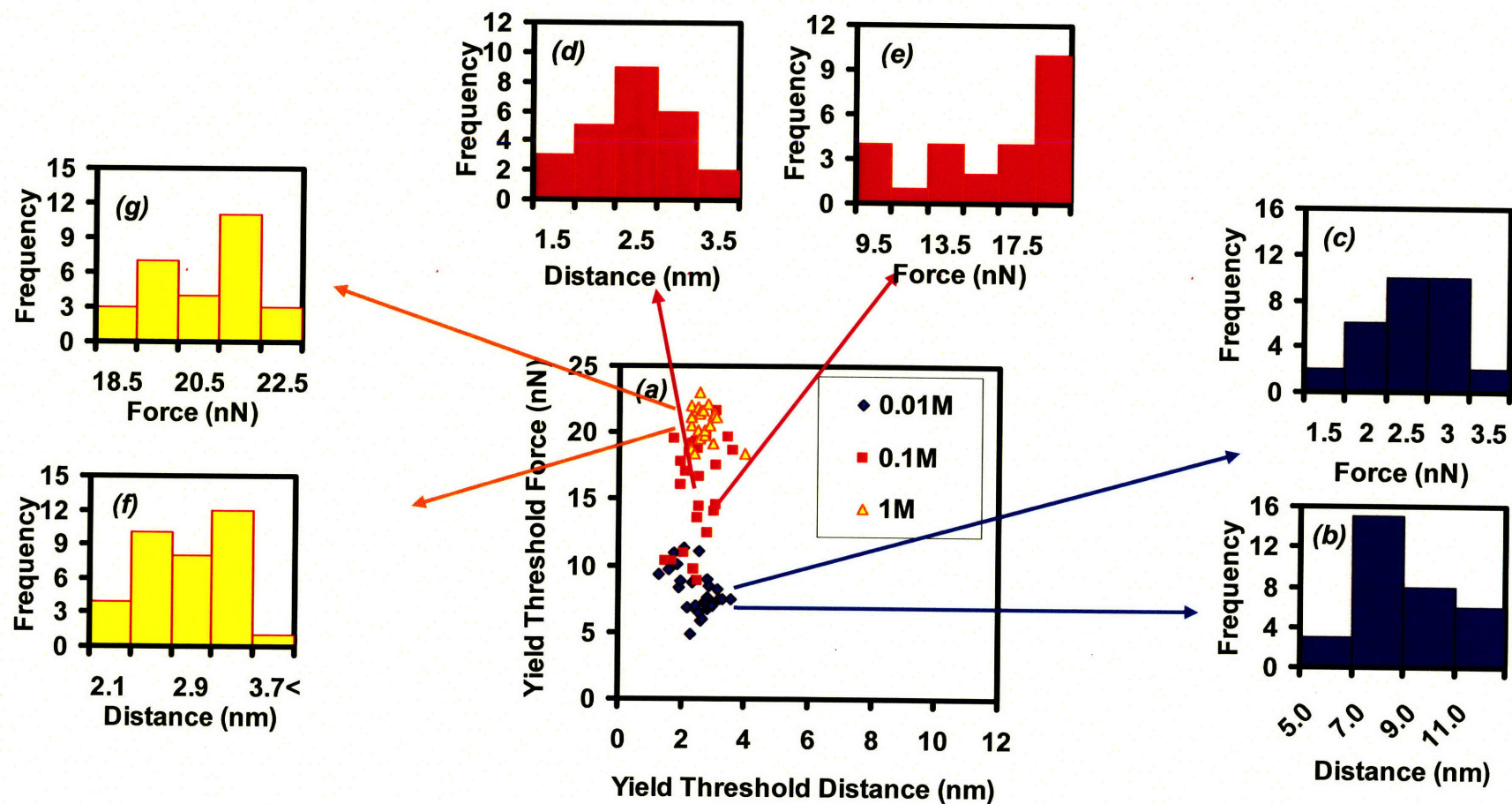


Figure 4-8. 2 Two-dimensional distribution and histograms of nanomechanical test on approach of opposing POPC mono-layers interaction. (a) Distribution of the second yield threshold distances and forces with varying ionic strength, (b) & (c) histogram of yield threshold distances and forces with 0.01 M IS; (d) & (e) histogram of yield threshold distances and forces with 0.1 M IS, (f) & (g) histogram of yield threshold distances and forces with 1 M IS.

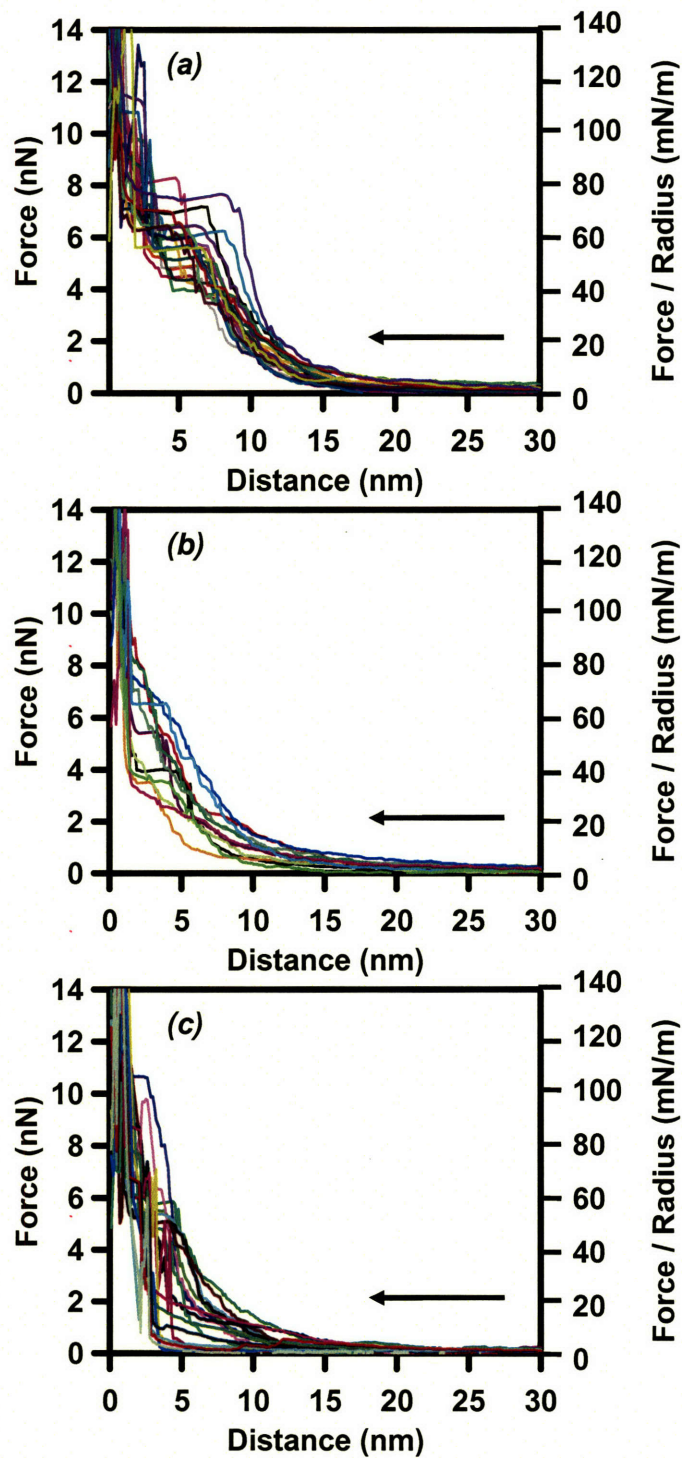


Figure 4-9. Individual force-distance curves on approach of opposing POPC bilayers interaction (Figure 4-3). (a) 0.01 M IS (b) 0.1 M IS and (c) 1 M IS solution concentration.

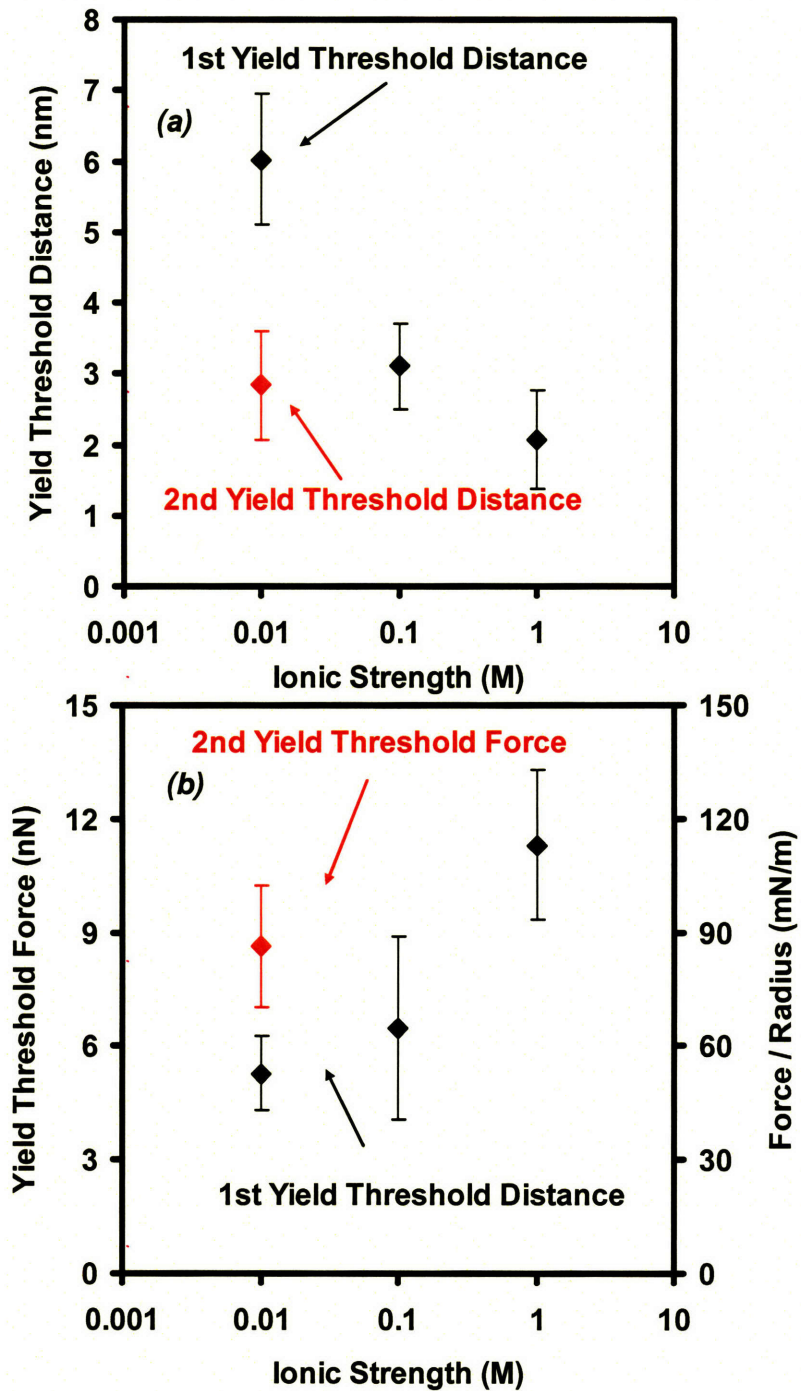


Figure 4-10. Plots on opposing POPC bilayers interactions (Figure 4-3). (a) Plots of the yield threshold force with varying ionic strength (b); plots of the yield threshold distance (the initial distance of breakthrough force) with varying ionic strengths. The difference is considered extremely statistically significant in force and distance as IS changes from 0.01 M to 1 M ($p < 0.0001$).

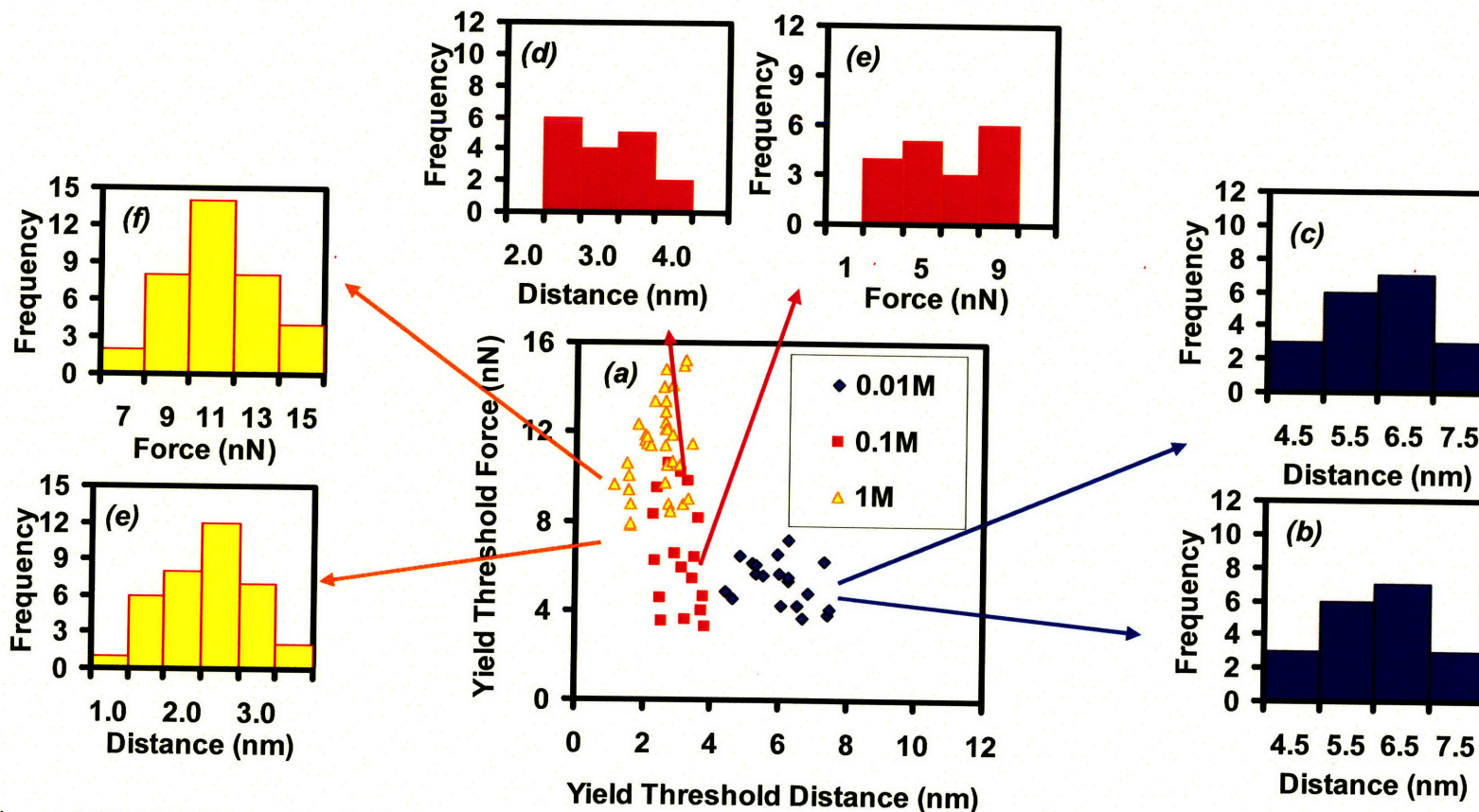


Figure 4-11. Two-Dimensional distribution and histograms for a nanomechanical test on opposing POPC bilayers interaction (Figure 4-3). (a) Distribution of yield threshold distances and forces with varying ionic strengths; (b) & (c) histogram of first yield threshold distances and forces with 0.01 M IS; (d) & (e) histogram of yield threshold distances and forces with 0.1 M IS; (f) & (g) histogram of yield threshold distances and forces with 1 M IS.

The interaction mechanisms between the lipid layers are complicated; two suggested pathways can reach the yield threshold forces by ruptures or fusions (Figure 4-12).¹²⁰ Even if these are the result of interactions from my SFA experiment, from these suggested pathways, the yield threshold mechanism of my HRFS experiment between bilayers on the tip and surface can be expected as follows. The two-yield threshold forces on 0.01 M IS seems to follow a hemi- and full fusion as shown in Figure 4-12; this scenario works well in the fluid phase of the lipid.¹²⁰ On 0.1 M and 1 M, only one clear yield threshold force was observed in this POPC experiment. It is expected that with the higher ionic strength, two lipid bilayers can be compressed together and fused or ruptured at one time because of the strong bindings of the head group on the higher ionic strength as discussed earlier in this chapter.^{103,125}

Returning to the HRFS experiment of POPC monolayers, it is assumed that the weaker monolayer ruptured or fused first and then the stronger monolayer ruptured later. For 30% of data, which did not show clear first-yield threshold forces, it is expected that both layers fused or ruptured together.

To better understand the nanomechanical properties of the lipid bilayer itself, the simpler experimental setup than used in POPC experiments was needed. Therefore, HRFS of the DPPC lipid bilayer versus the bare Si₃N₄ AFM probe tip were studied as detailed in the following section.

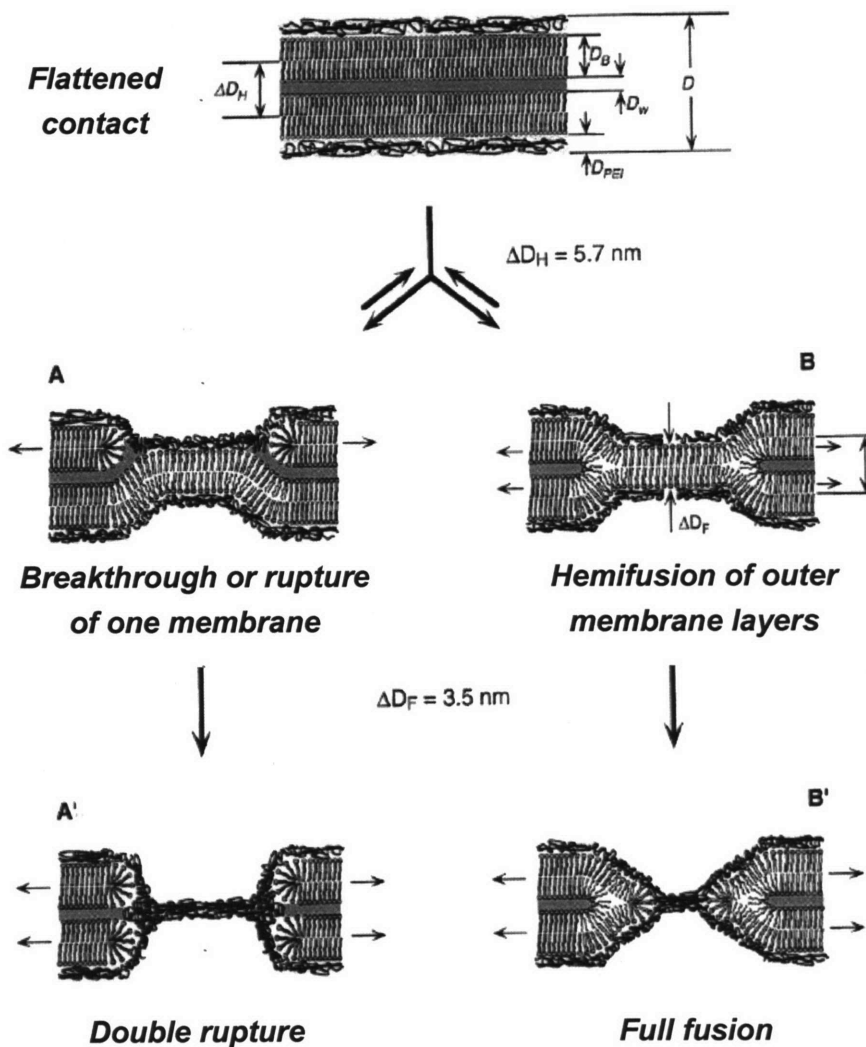


Figure 4-12. Schematic drawings of potential interaction mechanisms between lipid bilayers from SFA study.¹²⁰

4.3 1,2-Dipalmitoyl-sn-Glycero-3-Phosphocholine (DPPC)

4.3.1 Sample Preparation

After performing the POPC HRFS experiment, the direct deposit method for the sample preparation was tried and successfully optimized to reach the homogeneous DPPC bilayer region. As discussed in Chapter 3, this method is effective for ensuring the deposit of lipids on the targeted size of area with consistent amounts of DPPC

solution. The procedure is as follows: 100 $\mu\text{g/ml}$ DPPC (ethanol + chloroform 1:1) solution is prepared and is sonicated 3 times for total 30 minutes (10 minutes per one time) with extensive stirring between sonicating intervals. The DPPC solution (about 7 μl per drop on the mica) is deposited onto the mica surface. The solution is evaporated over 16 hr in the hood. This dried sample is then cleaned 3 times with 500 μl deionized water.

4.3.2 Experimental Method

Picoforce atomic force microscopy (AFM) was used mainly to perform HRFS of different ionic strengths (ISs, 0.01 M, 0.1 M, 1 M). In addition, scanning the DPPC bilayer with the AFM tip helps stabilize the planar homogeneous lipid bilayer. The tip speed was changed to 100 nm/sec (which is 10 times slower than that used in the POPC experiment) to make the static loading and to minimize the effects from the turbulence and vortex of the fluid and the impact. As the static loading in the macro-level gives the lower yielding force than the dynamic loading, the similar trend was observed on the nanomechanical test (Figure 4-13). The differences in yield threshold forces between the tip speeds of 100 nm/s and 200 nm/s was statistically significant ($p < 0.0168$) but between the tip speeds 1000 nm/s and 200 nm/s, the difference was not significant. This suggests that for static loading, the tip speed should be under 100 nm/s. Further study is needed to distinguish the criteria of the static loading.

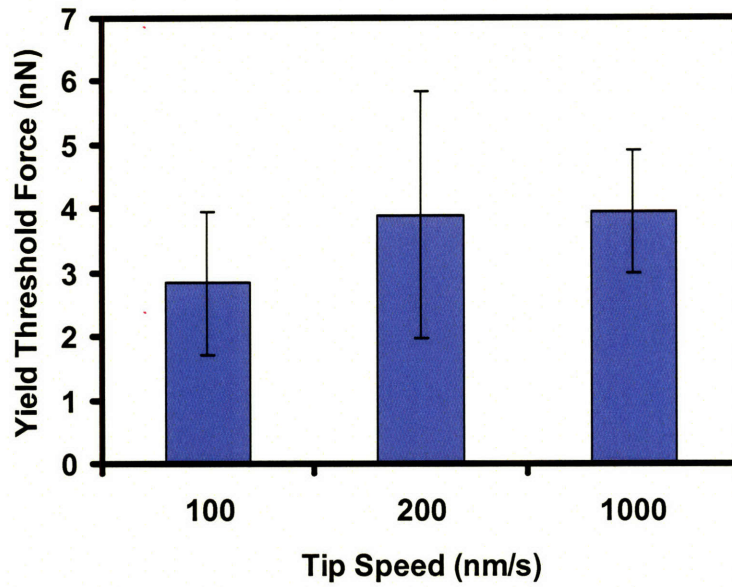


Figure 4-13. Plots of the yield threshold force with varying tip speed on approach. The difference in yield threshold forces between 100 nm/s and 200nm/s ($p < 0.0168$) is statistically significant.

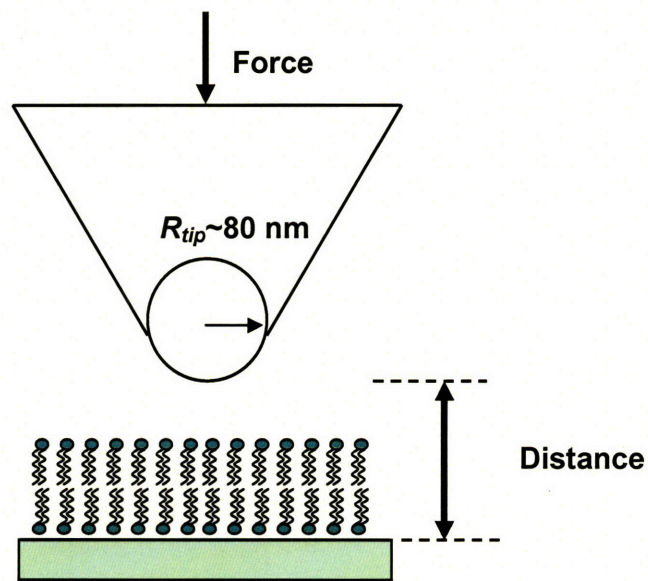


Figure 4-14. Schematic of the HRFS experiment involving the interaction of a bare Si_3N_4 AFM probe tip and a single lipid bilayer supported on planar mica.

4.3.3 Experimental Results and Discussion

HRFS of the silicon nitride tip ($R_{tip} = 80\text{nm}$) on "approach" (probe tip advancing towards surface, Figure 4-14) to the DPPC bilayer adsorbed on hydrophilic mica consistently showed single yield threshold force on 0.01 M IS and two-yield threshold forces on 0.1 M and 1 M (Figure 4-15). The most relevant research finding in this area was obtained using MFP1D, which shows that only 10~15% of the HRFS curves of 0.1 M and 1M have two-yield threshold forces and other curves have single yield threshold force.¹⁰³ In this research, however, two-yield threshold forces were observed consistently (Figure 4-15). It is expected that the static loading speed 100 nm/sec and a homogenized lipid bilayer surface after AFM scanning help the tip reach the two step forces. Typical individual HRFS curves (Figure 4-16, DPPC, 1 M) can be interpreted as seven distinct regimes based on the interaction of the lipid bilayer with the approach of the tip. The regimes of the approach curve are in the following order: (a) "noncontact surface interaction" regime governed achieved by electrostatic interaction, (b) "lipid bilayer contact" regime where the tip physically makes contact with the lipid bilayer, (c) "1st elastic compression of bilayer" regime where the bilayer is compressed by the end of the tip until the lipids hold the compressive force elastically, (d) "1st yield threshold" where the first layer is yielded at a distance near to the height of the lipid bilayer (e) "2nd elastic compression of bilayer" (f) 2nd yield threshold where the second layer, which is supported by the substrate, is obtained at a distance near to the height of the lipid monolayer (g) "substrate contact" where the end of the tip makes direct contact with the mica substrate. At steps d and f, the punctured yield threshold forces were observed when the tip penetrated the lipid bilayer.

In the case of the 0.01 M IS experiment, because there is only single yield

threshold force, it is used to compare both the first and second yield threshold forces (Figures 4-17 & 20). It is expected on the higher ionic strength, 0.1 M and 1M ISs, both upper and lower lipid layers are yielded in order from the upper layer to the lower layer. However, on 0.01 M IS, both layers are expected to be corrupted at once (Figure 14). The yield threshold distance on 0.01 M IS is shorter than the threshold distances on 0.1 M and 1 M ISs (the first-yield threshold distance, Figures 18 & 20). This shows that the entire lipid layers are holding forces and are yielded simultaneously on 0.01 M IS.

As the ionic strength increased, the final yield threshold force increased (Figures 18 & 20). The monovalent Na^+ and Cl^- ions are, as discussed before, important in making the lipid head groups hold together tightly. This can be explained by the screen and binding effect of ions on the charges of the zwitterionic lipid heads.^{103, 125}

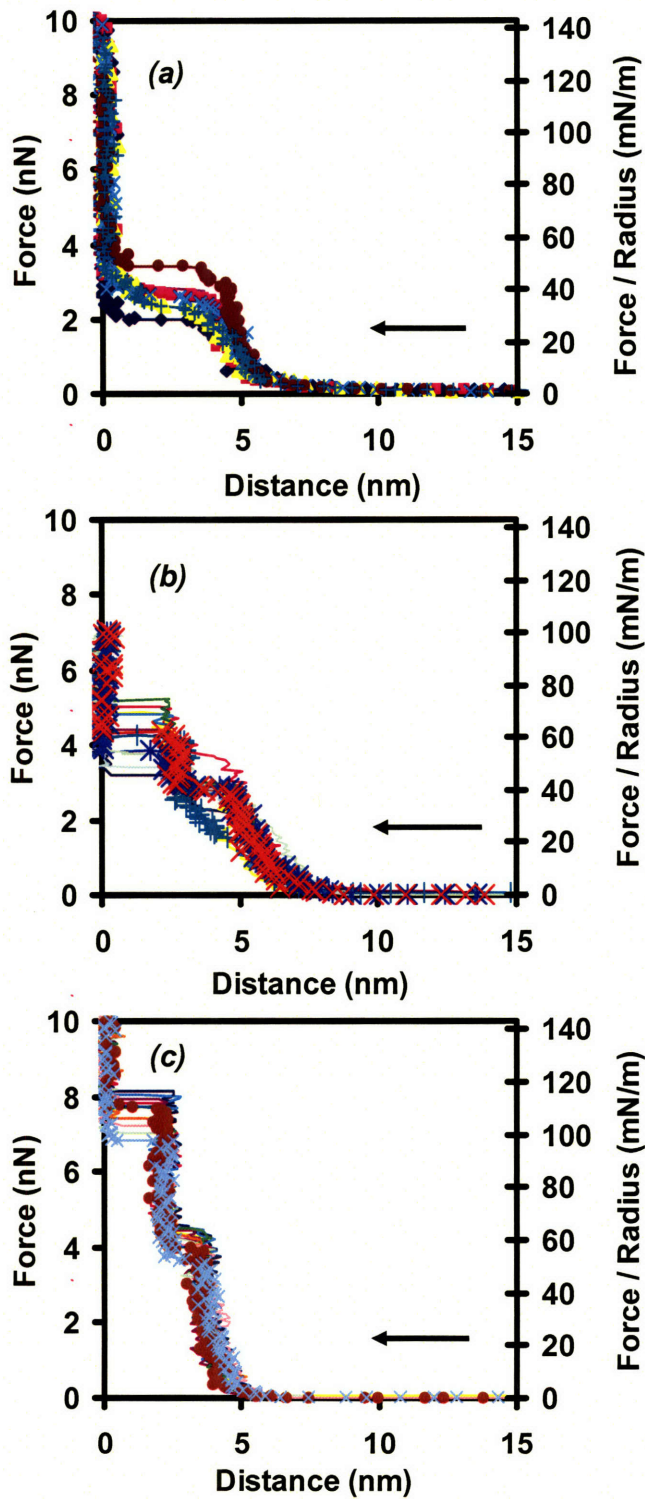


Figure 4-15. Nanomechanical data on the approach of the silicon nitride cantilever tip vs. the DPPC lipid bilayers on flat mica. (a) 0.01 M IS (b) 0.1 M IS and (c) 1 M IS.

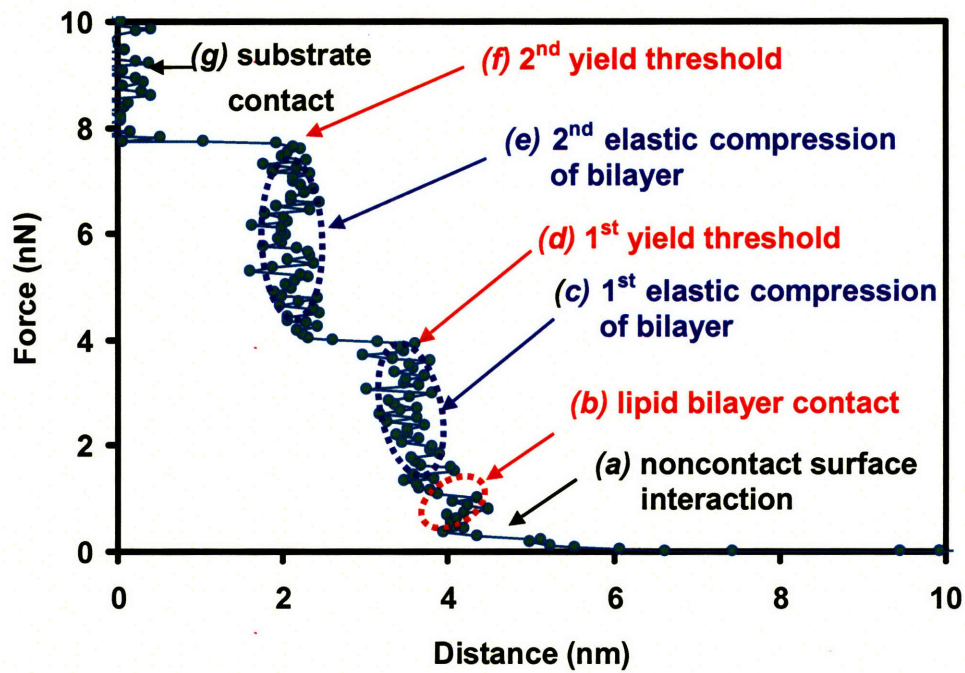


Figure 4-16. Typical individual approach curves for a DPPC-functionalized silicon nitride probe tip vs. a DPPC-functionalized substrate on 1 M IS (spring constant: 0.06 N/m, radius: 60 nm, displacement rate = 100 nm/sec).

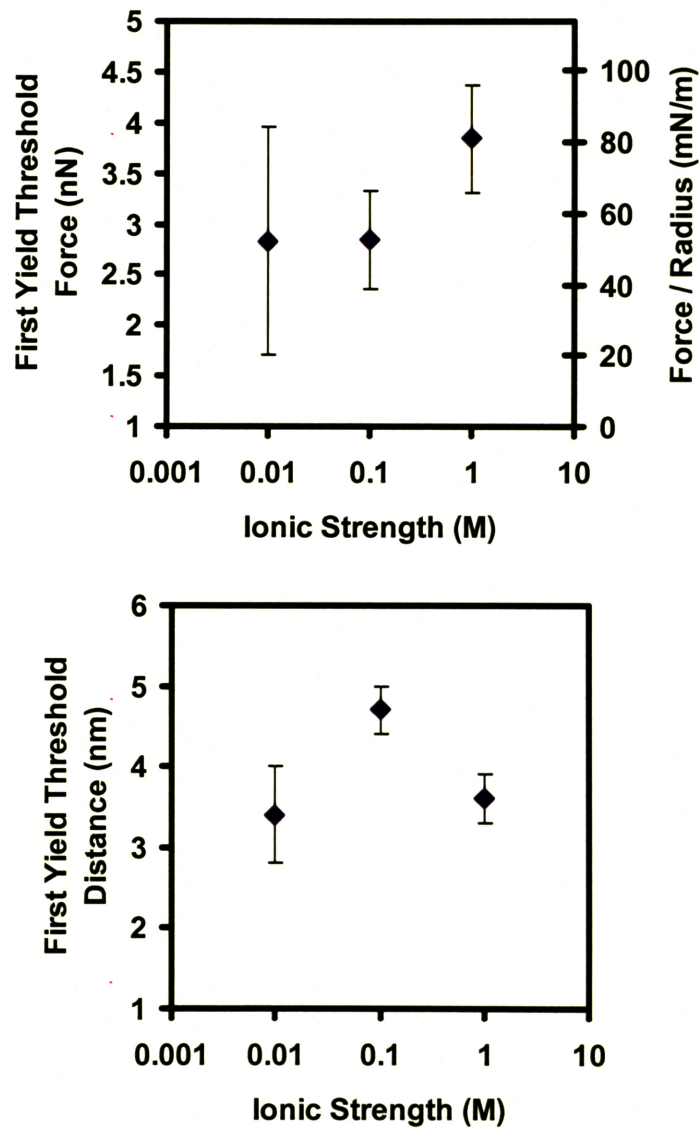


Figure 4-17. (a) Plots of a normalized first yield threshold force with varying ionic strengths. (b) Plots of the first yield threshold distance (the initial distance of breakthrough force) with varying ionic strengths. Because there is only one yield-threshold force and a distance of 0.01 M IS, these are plotted together.

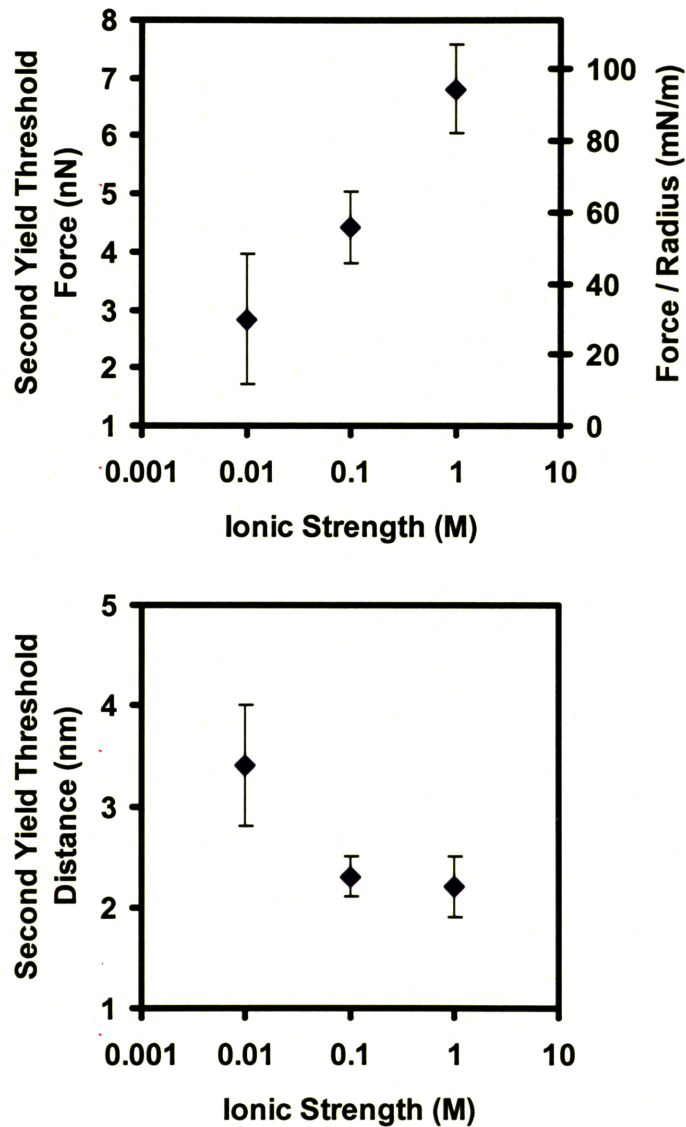


Figure 4-18. (a) Plots of a normalized second yield threshold force with varying ionic strengths. (b) Plots of the second yield threshold distance (the initial distance of breakthrough force) with varying ionic strengths. Because there is only one yield threshold force and distance of 0.01 M IS, these are plotted together. The difference is considered extremely statistically significant in the force as IS changes from 0.01 M to 1 M ($p < 0.0001$) and in the distance IS changes from 0.01 M to 0.1 M or 1 M ($p < 0.0001$).

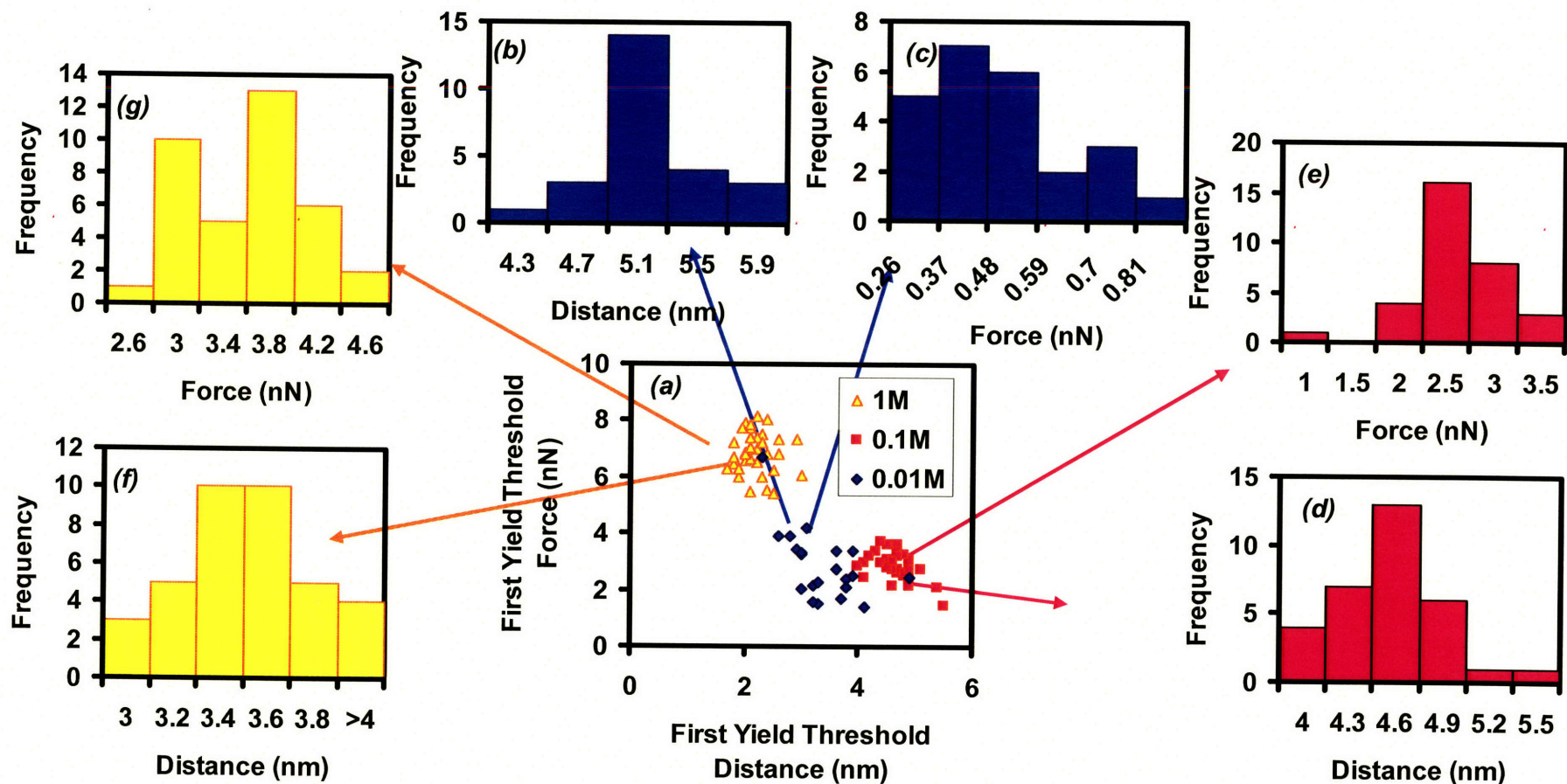


Figure 4-19. Two-dimensional distribution and histograms of a nanomechanical test (DPPC bilayer on mica vs. Veeco DNP tip). (a) Distribution of the first yield threshold distances and forces with varying ionic strengths; (b) & (c) histogram of yield threshold distances and forces with 0.01 M IS (d) & (e); histogram of yield threshold distances and forces of 0.1 M IS; (f) & (g) histogram of yield threshold distances and forces with 1 M IS.

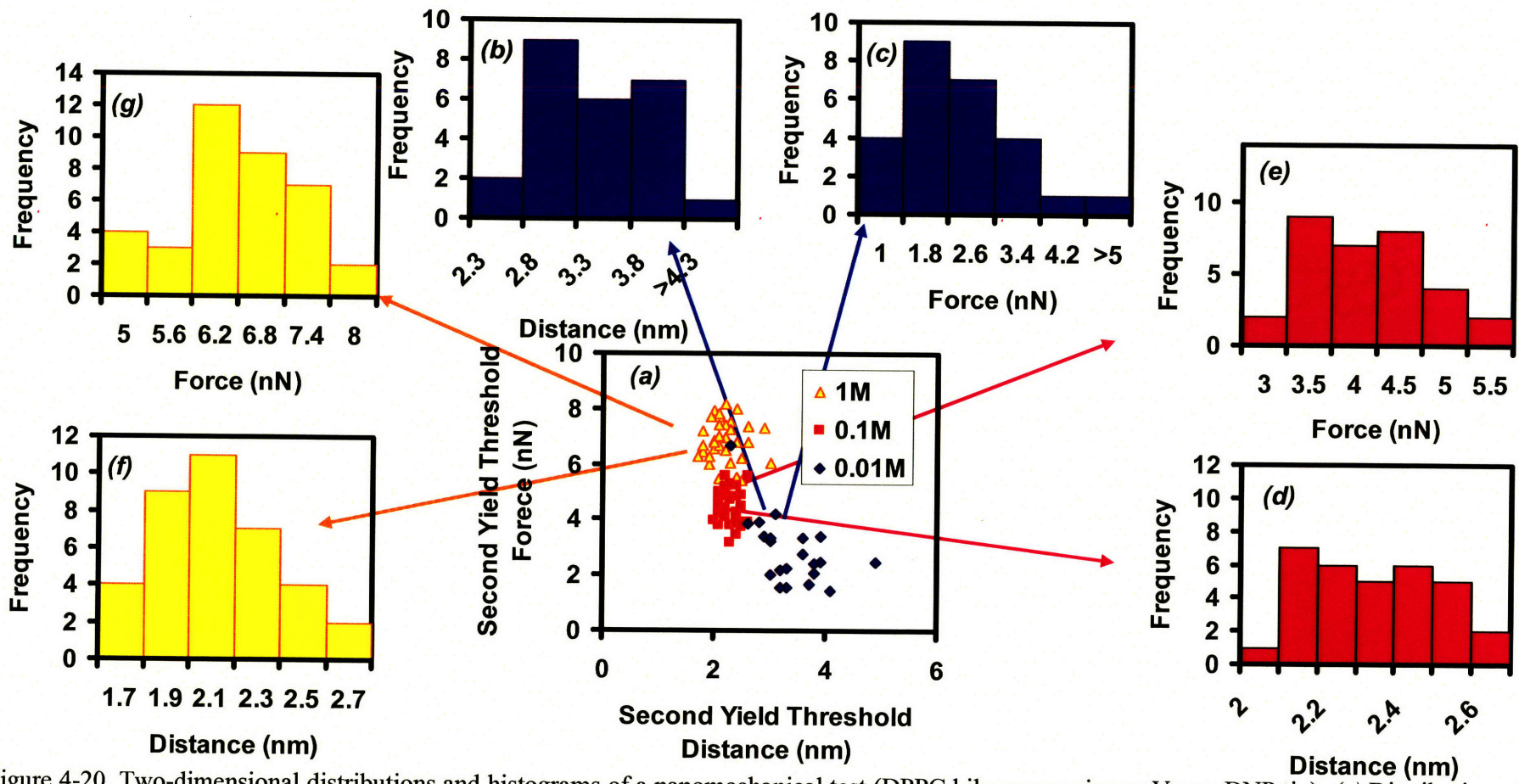


Figure 4-20. Two-dimensional distributions and histograms of a nanomechanical test (DPPC bilayer on mica vs. Veeco DNP tip). (a) Distribution of the second yield threshold distances and forces with varying ionic strengths; (b) & (c) histogram of yield threshold distances and forces with 0.01 M IS; (d) & (e) histogram of yield threshold distances and forces with 0.1 M IS; (f) & (g) histogram of yield threshold distances and forces with 1 M IS.

4.4 Interpretation and Comparison with the Literature

4.4.1 One-Yield Forces vs. Double-Yield Thresholds

As shown in Section 4.3.3 experimental results and discussion of DPPC, two yield thresholds were consistently observed on IS 0.1 M and 1 M for all of the data and one yield threshold was consistently observed on IS 0.01 M. This result differs from the experimental result by Garcia¹⁰³; only 10~15% of data showed two-yield thresholds on the higher ionic strength; these were assumed to be caused by the formation of another lipid layer on the tip as was discussed previously.¹²⁴ These researchers ignored the two yield threshold data mainly because a) the two yield thresholds were not observed when carboxyl-chemically-functionalized tips were used and b) the total distance for the two yield threshold from the substrate was greater than the lipid bilayer height, and the total length of the first-yield threshold was longer than the second yield regime.

In this research, however, as shown in the POPC experimental results and discussion in Section 4.2.3, even if a carboxyl-chemically-functionalized hydrophobic or hydrophilic tip was used, the experiment resulted in distinct one or two yield threshold forces. I assumed that the formation of the lipid layers on the tip's smaller curvature end rather than those on the planar surface would be of weaker strength and looser formation between the lipid head groups.

And as shown in the DPPC experimental results, the distances of the yield thresholds considering compression coincided with the height of the lipid layers. This result is different from other references.^{103, 124} Only a small change of the yield threshold distance was observed based on the change in ionic strength. For the higher ionic strengths, the yield threshold forces increased a statistically significant amount.

On the other hand, the reason why two yield thresholds were observed on the higher ionic strengths on DPPC experiments was because all my experiments were carried out after checking AFM images, which helped to form a well-defined planar surface via the scanning by AFM tips. The proper static experiment was also performed with a suitable tip speed (100 nm/sec), approach distance (over 500 nm) and time interval (5~10 seconds) between each individual experiment.

Considering this definitive result of two yield thresholds of the lipid bilayer, it is expected that with a higher ionic strength, the lateral interactive forces between the lipid head groups or lipid tail groups will be more dominant and stronger than the vertical forces between the lipid tails because in the lateral direction, there is strong lateral attraction between head groups from the hydrogen bonding in water molecules, Na⁺ and Cl⁻ monovalent ions' screening and binding on higher ionic strengths, and the hydrophobic lateral attraction of the 16 carbons (per one lipid tail) of the saturated DPPC lipid tails. On the contrary, the vertical hydrophobic attraction between tails was weak because there is only a one-to-one carbon interaction and there are possibly potential concentrated water molecules between lipid tails.¹⁰⁷

4.4.2 Change of the Slopes between the First Elastic Compression and the Second Elastic Compression

As shown in Figure 4-15 & 16, the HRFs of the higher ionic strengths 0.1 M and 1 M, the second elastic compression is stiffer than the first elastic compression. One reference using SFA shows a similar trend but this is due to the interaction between the lipid bilayers.¹²⁰ Before identifying the contact regime, it was expected that the electrostatic and van der Waals forces would be dominant. When the tip compresses lipid bilayers after initial contact, it is expected that the lateral attraction

among head groups resulting from the hydrogen bonding of water molecules, the screening and tighter packing effect of Na^+ and Cl^- ions on the charges of the zwitterionic lipid head groups will govern the initial increase of the elastic compression force and then, the strong hydrophobic interaction between the tails will create stiffer elastic compression on the first elastic compression regime. Furthermore, the deformations of both the upper and lower layers are expected until the upper layer reaches the first yield threshold.

After the first yield threshold, however, a stiffer increase of the compression forces was observed because the lower lipid layer has already been greatly compressed at the first compression regime and is strongly connected to the rigid planar mica with a strong hydrophilic attraction between the mica and lower lipid layer. In addition, the hydrophobic tails on the top are also laterally strongly connected each other. It is also expected that the lower layer, which is directly connected to the hydrophilic mica, will have a greater homogeneously arranged array than that of the upper layer because the mica is planar and strongly hydrophilic. And the lower lipid layer is the first formation on the mica substrate in the upgraded direct lipid deposit method.

One interesting finding is that even if both the upper and lower bilayer had the same structure, as the force increases the upper layer will most likely fail at the lower yield threshold, not simply because the upper layer is directly in contact with the tip but because of fracture mechanics whereby the relatively weaker head group will start to fracture easily due to defects of the upper lipid layer's contacted surface. This will be discussed in detail on the next chapter.

4.5 Conclusion

In this chapter, the nanomechanical properties of POPC and DPPC lipid layers were examined using HRFS. My findings clearly show that one or two yield threshold forces exist, whether the experimental setup is a POPC bilayer vs. a bilayer, a POPC monolayer vs. a monolayer or bare Si₃N₄ tip vs. a DPPC bilayer.

The simpler experimental setup, a bare Si₃N₄ tip vs. a bilayer, provided clearer experimental results. As the ionic strength increased on the same tip, the yield threshold forces increased and on the higher 0.1 M and 1 M ionic strengths, the yield threshold force of each layer could be detected at the proper range of distance between the tip and layer based on the height of the each lipid layer. This finding clearly differs from other studies as discussed in Section 4.4.1. The increased yield threshold forces based on the increase of ionic strength can be explained as follows. In the lateral direction, there is a stronger lateral attraction, which binds head groups tighter to each other from monovalent Na⁺ and Cl⁻ ions' screening and the binding effect on higher ionic strengths; consequently, this helps form well-distributed hydrogen-bonded water molecules from each head group and the closed hydrophobic lateral attraction of 16 carbons (per one lipid tail) of the saturated DPPC lipid tails.

CHAPTER 5

Effect of Length Scale and Geometry on the Nanoscale Surface Interactions and Compressibility of Supported Lipid Bilayers

5.1 Introduction

Chapter 5 discusses the high resolution force spectroscopy (HRFS) study of lipid bilayers. Pyramidal Veeco DNP silicon nitride tips with typical end radii, R_{tip} , ~20 nm but R_{tip} as sharp as ~60 nm were used. These tips have been used both with and without gold coating and have given stable images and HRFS results. However, as shown in chapter 3, detailed images of the DPPC bilayer and DPPC monolayer on the bilayer's boundary could best be observed using the sharpened, pyramidal Veeco DNP-S probe tip with a typical R_{tip} ~10 nm with an R_{tip} as sharp as 40 nm. In addition, a good AFM deflection image could be obtained using the conical μ masch sting probe tip with a smaller end radii, R_{tip} ~5 nm. These results indicate the potential effects of the length scale and geometry of AFM tips on imaging. As discussed in Chapter 3, as a result of prolonged use (in the square test, AFM imaging and HRFS tests), tips could be worn down and their radii increased. This will be discussed further in the experimental method.

This is the first study in which varying length scales and geometries of AFM tips have been used in lipid research. Previous work has been limited to standard size NP, NPS, Olympus, and other similar tips.^{121,122,123,124,125,126,127} In addition, previous work has not clearly articulated the time scale or number of tips used in a given experiment nor have researchers documented the small differences between tips.

Because there is always variance in manufacturers' specifications, the actual properties (e.g., spring constant and radius) of each tip may be different. In a nanoscale experiment, these small physical differences between AFM tips can lead to drastic differences in final results. Thus, it is extremely important to use only one tip for a series of experiments in order to minimize HRFS errors from tips.

On the other hand, researchers have not clearly shown how much the used silicon nitride tip wears out after hundreds of HRFS experiments and numerous AFM imagings. This wear and tear can cause a fundamental error in the quantitative analysis because the forces divided by radii of the tips is compared. The radius of the tip should be correctly measured before and after an experiment. This "worn-out" environment is inevitable for the silicon nitride tip but it is still used for AFM imaging and HRFS experiments because it can make the finer end radii of the tip by oxide sharpening.¹²⁸

This chapter details how HRFS was employed to study the effects of length scale and geometry on the nanoscale interactions and compressibility of supported lipid bilayers. My ultimate goal is to better understand the transition from localized molecular deformations of small groups of phospholipids to the more homogenized continuum-like responses of many lipids. This study on the effect of length scale and geometry has not been carried out before in lipid-related research.

5.2 Materials

5.2.1 Selection of Lipid

1,2-dipalmitoyl-sn-glycero-3-phosphocholine (DPPC) on mica was used as a model system because the gel-type DPPC bilayer at room temperature showed stable AFM images and HRFS results as described in Chapters 3 and 4.

5.2.2 Sample Preparation

The direct deposit method that was described in chapters 3 and 4 was used again in this experiment (Figure 3-15). A drop (7 μ l) of 100 μ g/ml DPPC solution (1:1 methanol + chloroform) was deposited on the planar mica surface and allowed to dry for 24 hr. Next, two ionic strengths, 0.01 M and 0.1 M, of 10 mM Tris (hydroxymethyl) aminomethane buffer (pH 7.6) was added to the DPPC's dried surface.

5.2.3 Selection of Tips

Two types of AFM tips were used to investigate the tip's length scale and geometry effects. Pyramidal Veeco DNP silicon nitride probe tips with typical R_{tip} ~20 nm and maximum R_{tip} ~60 nm, and conical μ masch sting probe tips with smaller, R_{tip} ~5 nm were used for the HRFS study; results obtained using these two different tips were compared.

5.3 Experimental Method

Before performing the HRFS experiment, the square test described in Chapter 3 was performed first for all the tips including the DNP tip to ensure that only one lipid bilayer was established. As discussed in Chapter 3, because of the square test, several imagings and HRFS tests, tips were worn out and the radii of tips were increased with R_{tip} ~80nm (DNP) and R_{tip} ~50nm (DNP-S), and R_{tip} ~30nm (μ masch sting probe tip). The tips that were used in chapter 3 for the square test and imaging were used for HRFS in the consecutive manners. After the square tests, AFM imaging and HRFS, using a scanning electronic microscope (SEM) were employed to view the tips. Nanomechanical experiments performed on areas perpendicular to the sample plane on

the “approach” (tip advancing towards the sample surface) with a tip speed 100 nm/sec were carried out, under a static loading condition in a 10 mM Tris (hydroxymethyl) aminomethane buffer (0.01M ionic strength or 0.1M, pH 7.6). The tip speed for the static loading is detailed in Section 4.3.2.

5.4 Results and Discussion

5.4.1 0.01 M IS condition

The yield threshold forces, F_y s, required for the tip to penetrate the lipid bilayers were quantified. It was observed that F_y increased as the probe size decreased (Figure 5-1). F_y s were 35 ± 14 mN/m ($R_{tip} \sim 80$ nm), 234 ± 38 mN/m ($R_{tip} \sim 50$ nm), and 693 ± 280 mN/m ($R_{tip} \sim 30$ nm) (Figure 5-2 (a)). The intermediate-sized (middle) tip ($R_{tip} \sim 50$ nm) experienced one lower F_y , 90 ± 19 mN/m before reaching the final F_y (Figure 5-2 (a)). It is assumed that this tip size can achieve the optimum range needed to observe the yield threshold force of each layer. If the tip size is too big, lipid bilayers will be ruptured simultaneously. In contrast, if the tip size is too small, it will penetrate the lipid bilayers with friction rather than disrupt each layer. The F_y values reflected a statistically significant difference. In contrast, the yield threshold distances were consistently lower than the height of the DPPC bilayer (Figure 5-2 (b)) within a similar range. The compression (repulsion) for the lipid bilayer was initiated at the height near the DPPC bilayer and remained compressed until it reached the yield threshold. The smaller tip ($R_{tip} \sim 30$ nm) was expected to create higher compression and localized molecular deformations for all the layers rather than each individual layer. However, the larger tip seemed to have a yield threshold force on the lower level because the stress concentration and fracture on the weaker or dislocated region; the failure of the

structure under the yield strength of the material used can be explained by using the stress concentration on defects (fracture mechanism). Assuming a hemispherical geometry, a $0.5 \text{ nm}^2/\text{lipid molecule}$, and the 4.5 nm height of the lipid bilayer from the AFM imaging, the smallest tip ($R_{tip} \sim 30 \text{ nm}$) interacted with ~ 101 molecules at the yield distance (4.23 nm), the intermediate tip interacted with ~ 163 molecules at the first yield distances (4.24 nm) and 200 molecules at the second yield distances (1.93 nm; the lower layer was from $4.5/2 = 2.25 \text{ nm}$) and the largest tip ($R_{tip} \sim 80 \text{ nm}$) interacted with $\sim 1,098$ molecules at the yield distance (3.4 nm). The observed trend for decreasing F_y with increasing R_{tip} might be attributed to probing a larger number of molecular scale holes, dislocations or imperfect lipid bilayer regions causing increased stress concentration and eventually failure. In order to support this hypothesis, the following analysis was carried out.

The largest tip ($R_{tip} \sim 80 \text{ nm}$) exhibited a discontinuous jump without a change of the force in the constant compliance regime after the yield threshold force, F_y was reached. This result indicates that the fracture mechanism is dominant once the yield threshold force is reached. The middle tip ($R_{tip} \sim 50 \text{ nm}$) exhibited first discontinuous jump after the first-yield threshold force, 1st F_y was reached. After the second yield threshold force was reached, a continuous increase in force and compression was observed until the constant compliance regime was reached at the ultimate force, F_u . Similarly, for the smallest probe tip ($R_{tip} \sim 30 \text{ nm}$), a continuous increase in force and compression was observed until the constant compliance regime was reached at the ultimate force, F_u achieved after the yield threshold force, F_y , was reached. The ultimate forces were $234 \pm 38 \text{ mN/m}$ ($R_{tip} \sim 50 \text{ nm}$), and $966 \pm 321 \text{ mN/m}$ ($R_{tip} \sim 30 \text{ nm}$) (Figure 5-3 (b)) and the difference between F_u and F_y (F_{u-y}) and between the mean

values were 35 mN/m ($R_{tip} \sim 50$ nm) and 273 mN/m ($R_{tip} \sim 30$ nm). These results indicate that an inelastic or hardening homogeneous compression without instability on the smallest tip plays a greater role than the fracture mechanism. The reason why the difference F_{u-y} of the smallest tip is greater than that of middle tip is because the smallest tip penetrates the entire bilayer whereas the middle tip penetrates just the lower layer of the bilayer.

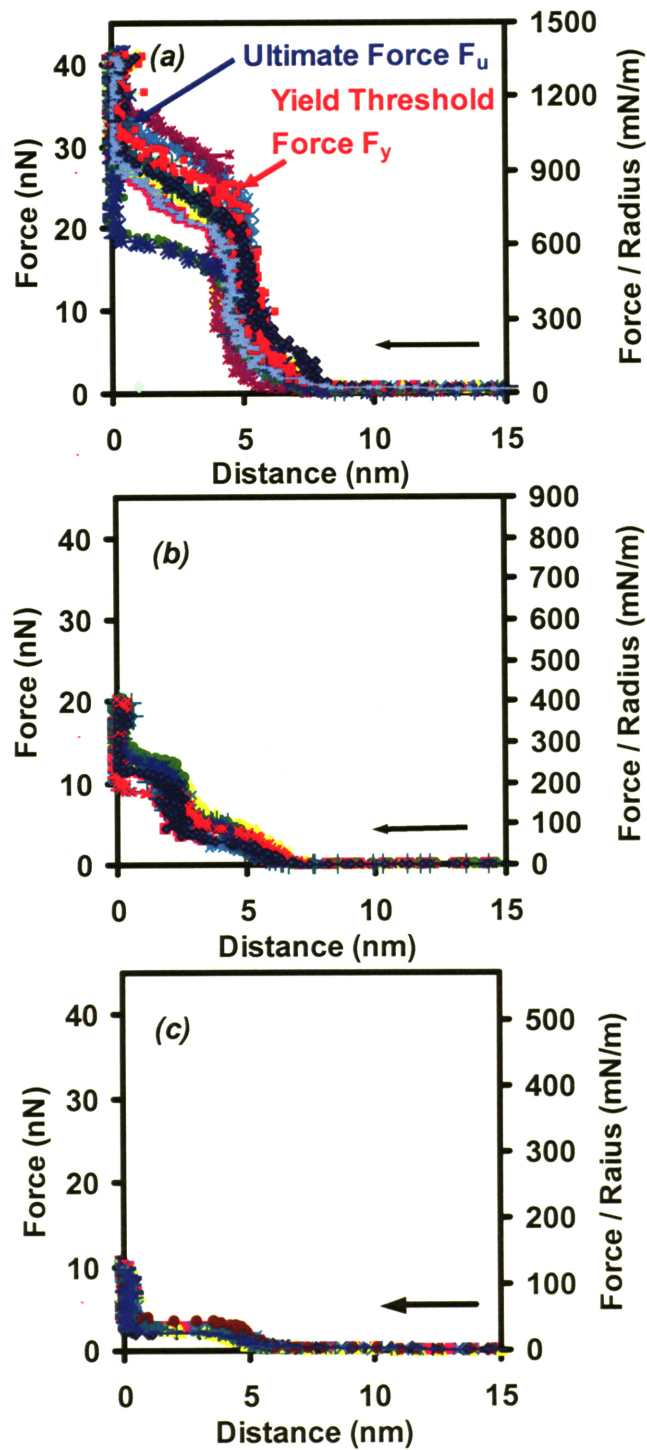


Figure 5-1 Nanomechanical data on approach. (a) μ masch sting ($R_{tip} \sim 30$ nm), (b) DNP-S ($R_{tip} \sim 50$ nm), (c) DNP ($R_{tip} \sim 80$ nm) silicon nitride cantilever tip vs DPPC lipid bilayers on flat mica with Tris buffer (0.01 M IS).

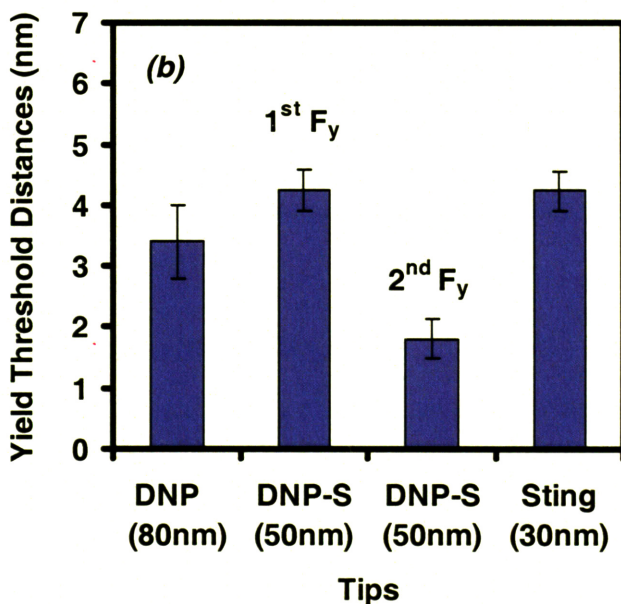
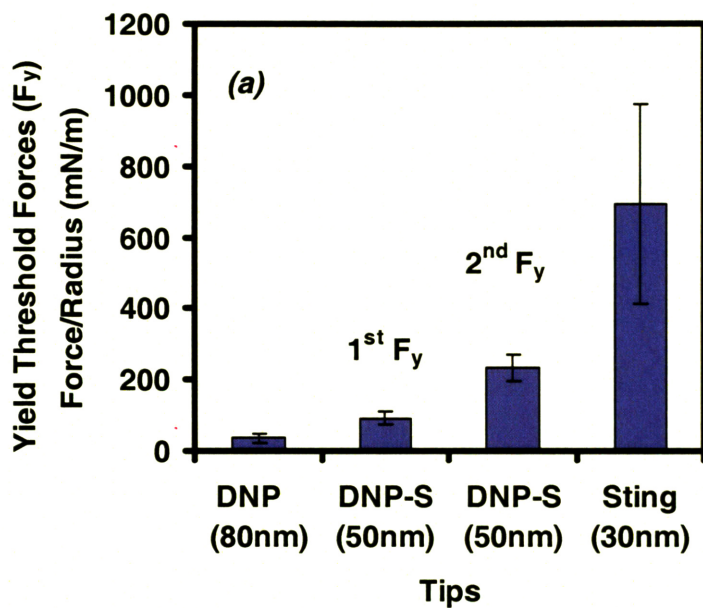


Figure 5-2. (a) Nanomechanical data on the approach of (a) μ masch sting ($R_{tip} \sim 30$ nm), silicon nitride cantilever tip on DPPC lipid bilayers (unclear yield threshold) on flat mica or flat mica with Tris buffer (0.01 M IS); (b) Plots of normalized ultimate forces of the DPPC bilayers (0.01 M IS) when the tip reaches the compliance regime of HRFS with DNP ($R_{tip} \sim 80$ nm), DNP-S ($R_{tip} \sim 50$ nm) and μ masch sting ($R_{tip} \sim 30$ nm) probe tips.

Some of the results of smallest tip did not have the yield threshold forces but the repulsive force increased to the ultimate force, F_u . This could be easily distinguished from the empty region where the tip directly touched the mica (Figure 5-3(a)). These results are assumed to be caused by the less-packed, dislocated or imperfect lipid bilayer region as conferred in the suggested hypothesis.

To check how much of these HRFS data were distributed across a certain area, an equally spaced (100 nm) HRFS was performed for a well-defined DPPC bilayer (Figure 5-4(b) and 5-5(b)) and compared with the two smaller tips with 0.01M IS (Figure 5-4(c) and 5-5(c)). In Figure 5-4(c), the dark gray square indicates one (the smallest tip) or two (the mid-sized tip) clear yield threshold forces and the light gray square shows that it has an ambiguous or no yield threshold force (as discussed in the previous page) and that the repulsive force gradually increases. White squares mean there was no detection of a yield threshold force and distance. This suggests that there are holes that are not within the lipid bilayer's domain. For the middle and smallest tips, 88% ($R_{tip} \sim 50$ nm) and 57% ($R_{tip} \sim 30$ nm) respectively, the overall positive HRFS data shows a clear yield threshold force (the increase of the repulsive force after the yield threshold force was observed for all of the data). The rest of the HRFS data (12% ($R_{tip} \sim 50$ nm) and 43% ($R_{tip} \sim 30$ nm) of the data within the lipid domain) had an unclear or no yield threshold force and the repulsive force gradually increased until it reached the ultimate force, F_y (Figure 5-4 (c) & 5-5 (c)).

These results were consistent with my hypothesis. As the tip size decreases, there are more possibilities to meet the less packed, dislocated or imperfect lipid bilayer region outside of the well-packed region the well packed region. Because of this, the inelastic hardening mechanism (less stress concentration) during penetration is more

dominant than the fracture mechanism of the larger tip.

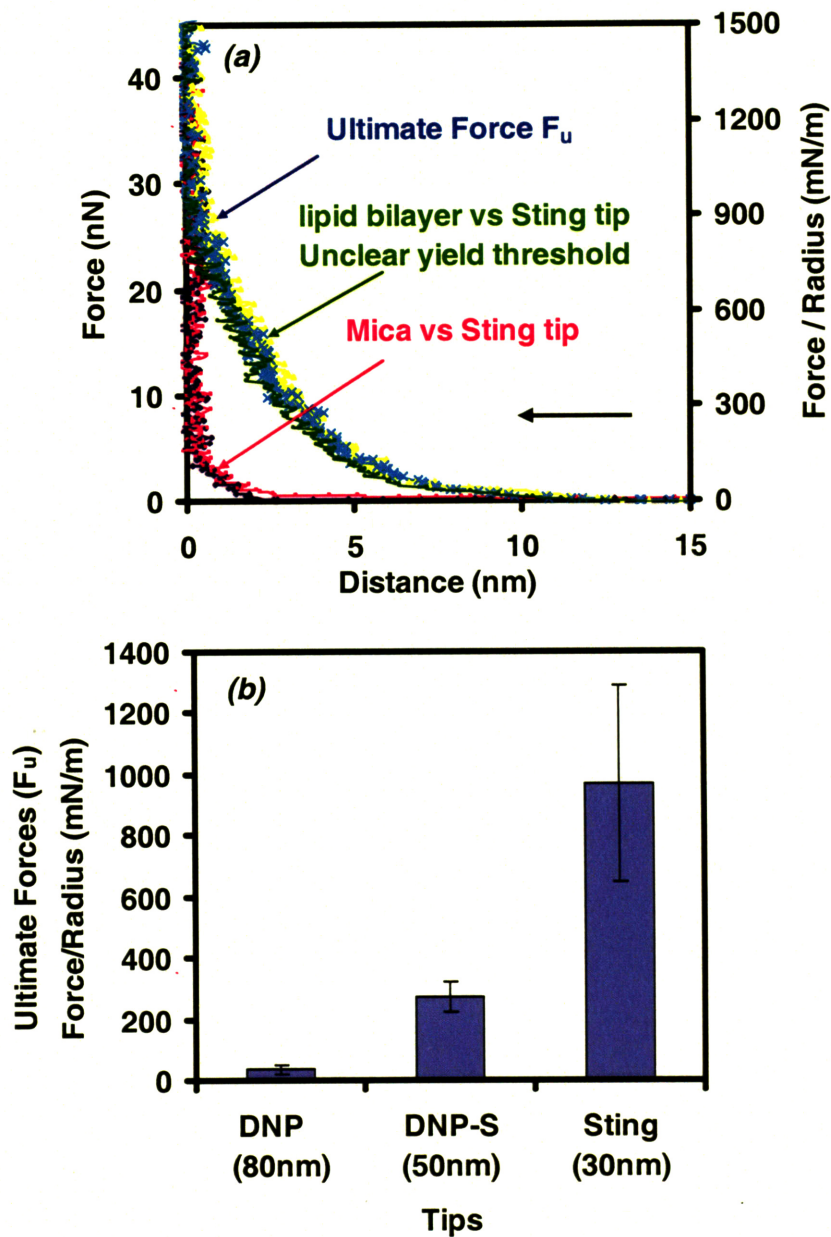


Figure 5-3 (a) Nanomechanical data on the approach of (a) μ masch sting ($R_{tip} \sim 30$ nm), silicon nitride cantilever tip on DPPC lipid bilayers (unclear yield threshold) on flat mica or flat mica with Tris buffer (0.01 M IS); (b) Plots of normalized ultimate forces of the DPPC bilayers (0.01 M IS) when the tip reaches the compliance regime of HRFS with DNP ($R_{tip} \sim 80$ nm), DNP-S ($R_{tip} \sim 50$ nm) and μ masch sting ($R_{tip} \sim 30$ nm) probe tips.

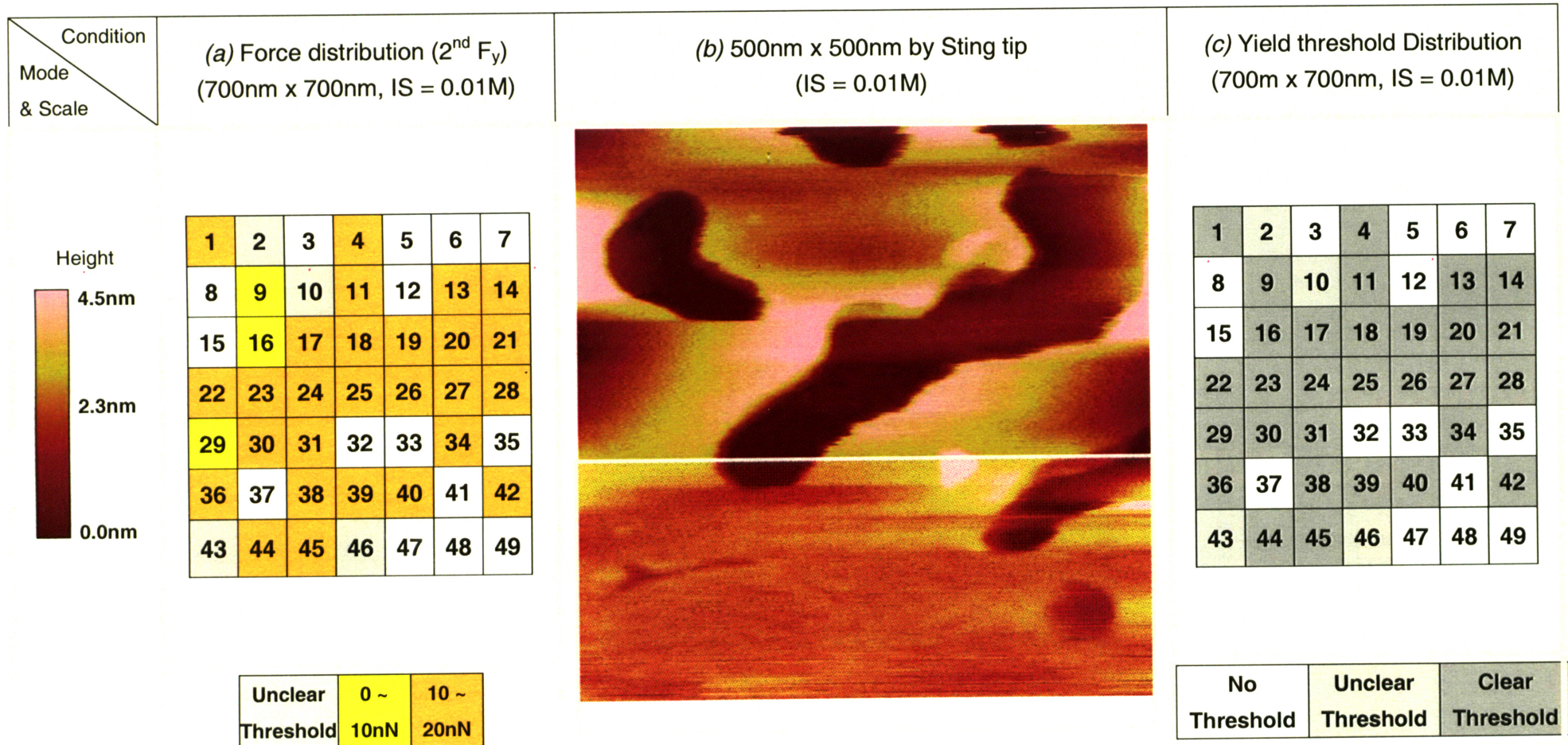


Figure 5-4 (a) Force distribution (700 nm x 700 nm size); (b) AFM image (500 nm x 500 nm size); and (c) Threshold distribution (700 nm x 700 nm size) of HRFS data with DNP-S ($R_{tip} \sim 30$ nm) probe tip (0.01 M IS). Spacing in each HRFS experiment is 100 nm and the HRFS experiment was performed only one time in each position. The dark gray boxes indicate a clear yield threshold (well-packed DPPC layers), light gray boxes, an unclear yield threshold (less packed DPPC layers), and white boxes indicates no yield threshold (no DPPC layers).

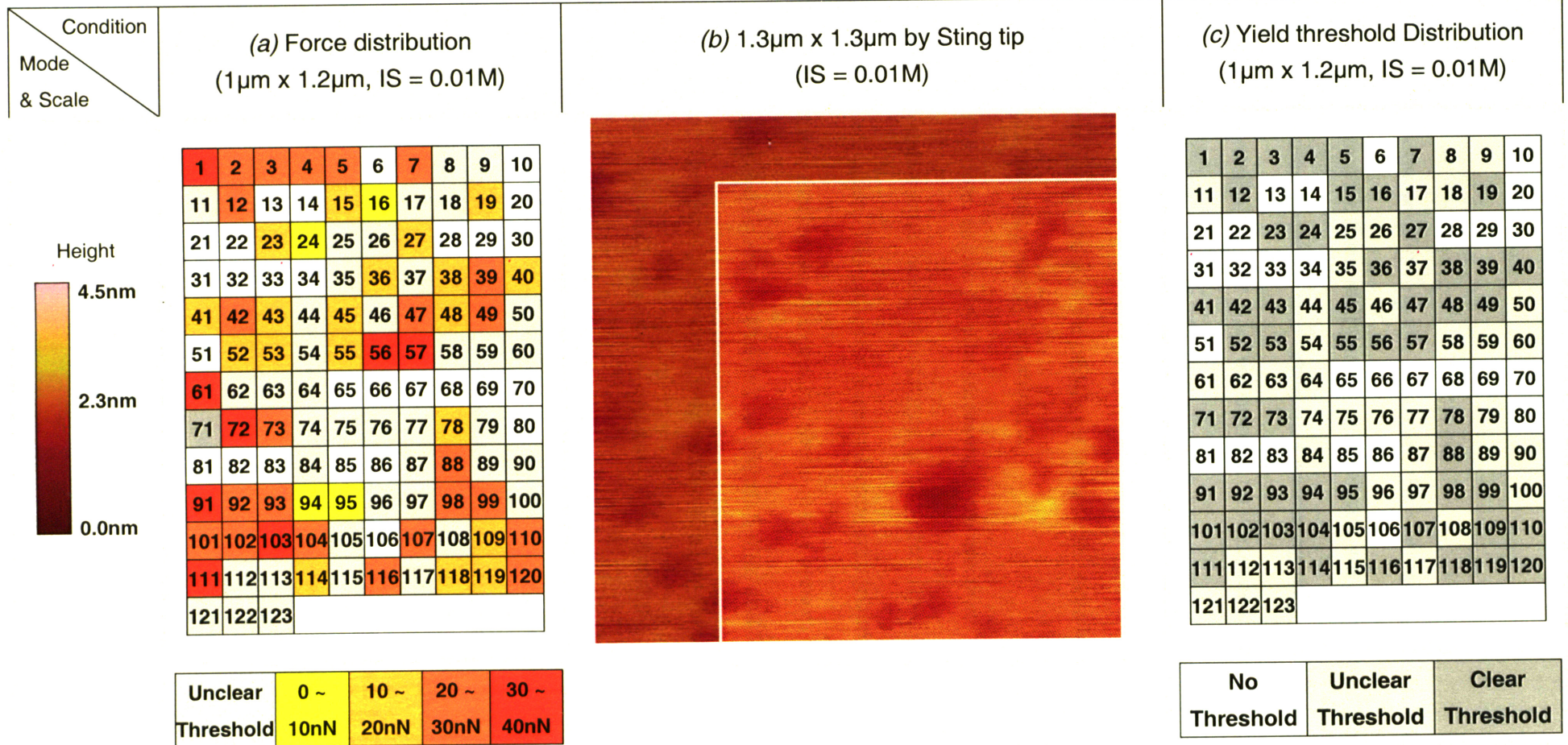


Figure 5-5 (a) Force distribution (b) AFM image, and (c) Threshold distribution (1 μm x 1 μm size) of HRFS data with μmasch sting ($R_{\text{tip}} \sim 30 \text{ nm}$) probe tip (0.1 M IS). Spacing in each HRFS experiment is 100 nm and the HRFS experiment was performed only one time in each position. The dark gray boxes indicate a clear yield threshold (well-packed DPPC layers), light gray boxes, an unclear yield threshold (less packed DPPC layers), and white boxes indicates no yield threshold (no DPPC layers).

In contrast, as the tip size decreases, there are more also more possibilities for the tip to meet the finer, well-packed lipid bilayer, which is why the yield threshold forces increased as the tip size decreased. Considering only the ultimate forces of the middle and smallest tip, the F_u of the smallest tip was quite a bit higher than that of the middle tip. Considering the effects of fracture energy and inelastic hardening energy and a statistical view, the HRFS results of the smallest tip are mostly governed by inelastic energy but those of the middle tip are affected more by fracture energy even if the inelastic hardening energy is combined.

Therefore, as the tip size increases, there are more possibilities for probing more molecular scale holes, dislocations or imperfect lipid bilayer regions within a well-packed region. This causes an increased stress concentration and eventually failure of the fracture mechanism as suggested above in this section. The force distribution of the medium-sized tip and the smallest tip (Figure 5-4 (a) and 5-5 (a)) also supports this hypothesis. The force distribution of the middle-sized tip has a very stable force on an entire area with small amounts of unclear or no threshold positions, but the force distribution of the smallest tip has unclear or no threshold positions adjacent to clear threshold positions. The clear yield threshold force position is surrounded by the unclear or no yield threshold force positions when considering all directions shown in Figure 5-5.

As for the largest tip ($R_{tip} \sim 80$ nm), several HRFS experiments were performed at one position with time intervals (over 30 seconds) and the tip moved to another position. As shown in other studies^{103,104,119} and this research (in chapters 3 and 4), the DPPC bilayer reforms itself quickly after HRFS so HRFS experiments can be reproduced on the same position multiple times.

5.4.2 0.1M IS condition

The HRFS results on 0.1M IS showed higher yield threshold forces than those on 0.01M IS using the same size tips (Figure 5-6). The result was discussed earlier in Chapter 4: that monovalent Na^+ and Cl^- ions play an important role in causing the zwitterionic head groups to hold each other more strongly with higher ionic strengths. Consequently, the AFM image clearly shows a well-packed surface (Figure 5-8 (b)). The yield threshold force of the smallest tip ($R_{tip} \sim 30$ nm, 1095 ± 28 mN/m) was much higher than the final yield threshold force of the largest tip ($R_{tip} \sim 50$ nm, 55 ± 8 mN/m) (Figure 5-6 (a)). However, the yield threshold distance (2.8 ± 0.85 nm) of the smallest tip with 0.1M IS decreased from that of the smallest tip with 0.01M IS. This phenomenon is also thought to be caused by the stronger binding effect of the head group, which enables the lipid bilayer to more effectively hold the compression force from the tip. The 85% ($R_{tip} \sim 50$ nm) HRFS data, (excluding the white squares (no-color space)), had a distinct yield threshold force (the increase of the repulsive force after the yield threshold force was observed for all of the data). Considering only 57% of the HRFS data had a clear yield threshold force with 0.01 M IS, this evidently shows how important it is to increase the ionic strength to create a densely packed surface. Furthermore, all subsequent HRFS data showed the formation of the lipid bilayer except the first four and the last one segment of data (the white area) with no lipid bilayer.

This ionic strength is similar to the *in vivo* state when the membrane faces the blood stream (0.15 M IS). This result clearly shows that the lipid bilayer clearly forms a well-packed surface on *in vivo* state.

The force distribution of the HRFS result shows a periodical increase of the

force in the scale from 10 to 50 nN in any direction as shown in Figure 5-8; the positions of the highest yield threshold forces (40~50 nN) were well distributed with the distance of several hundred nanometers; the highest yield threshold forces (40~50 nN) were not detected for more than three consecutive times in all directions. It is expected that even if the lipids are well packed and ordered across an overall area, there are still more densely packed areas. It is also expected that the additional components (cholesterol, other lipids, etc.) of an actual human membrane such as that of an endothelium cell, help to establish the rigid, more densely packed surface.

5.5 Conclusion

Larger HRFS tips have a greater chance of making contact with a surface on a less ordered regime that has defects or dislocations in homogeneous groups of lipid bilayer. This causes stress concentration and failure on the defects and dislocations, which strongly suggests that the fracture mechanism prevails on the yielding mechanism. To the contrary, a shorter scale tip can make contact with only a homogenized regime or a non-homogenized regime. Therefore, HRFS will have either an unknown yield threshold force on the non-homogenized regime or a clear yield threshold force on the homogenized regime. This means that yielding mechanism prevails on the fracture mechanism. As the ionic strength increases, the DPPC bilayer surface is more homogeneous and achieves higher yielding threshold forces across the entire area.

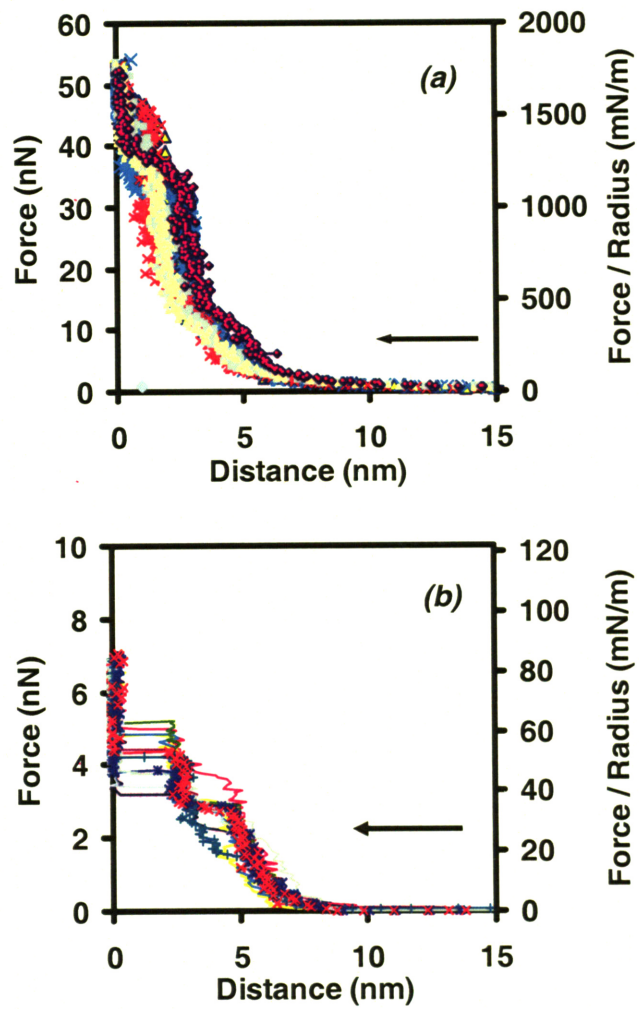


Figure 5-6 Nanomechanical data on approach. (a) μ masch sting ($R_{tip} \sim 30\text{nm}$), (b) DNP ($R_{tip} \sim 80\text{nm}$) silicon nitride cantilever tip vs DPPC lipid bilayers on flat mica with Tris buffer (0.1M IS).

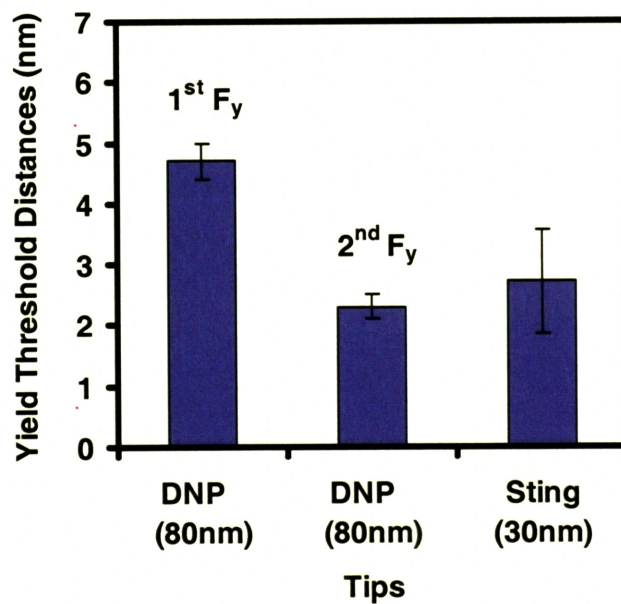
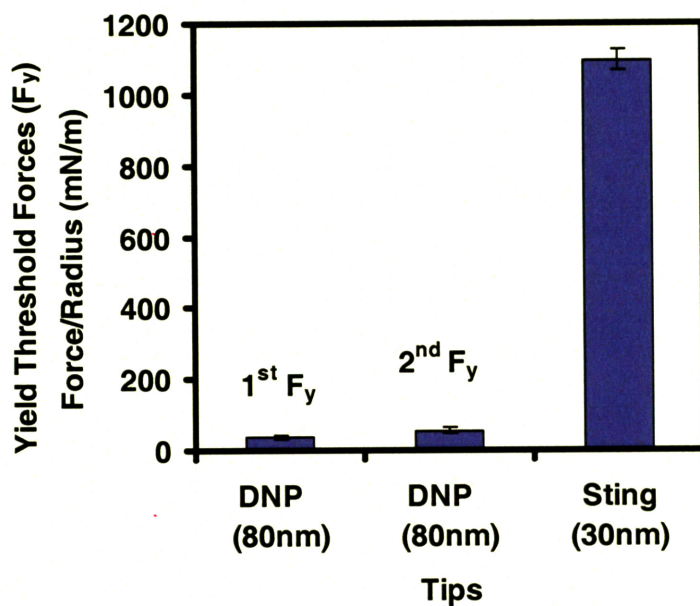


Figure 5-7 (a) Plots of the normalized yield threshold forces of DPPC bilayers (0.1M IS) with varying probe tips; DNP ($R_{tip} \sim 80\text{nm}$) and $\mu\text{masch sting}$ ($R_{tip} \sim 30\text{nm}$) in order, (b) Plots of the yield threshold distances of DPPC bilayers on 0.1M IS with varying probe tips; DNP ($R_{tip} \sim 80\text{nm}$), and $\mu\text{masch sting}$ ($R_{tip} \sim 30\text{nm}$) in order. Only DNP probe tip has consistent two yield threshold forces.

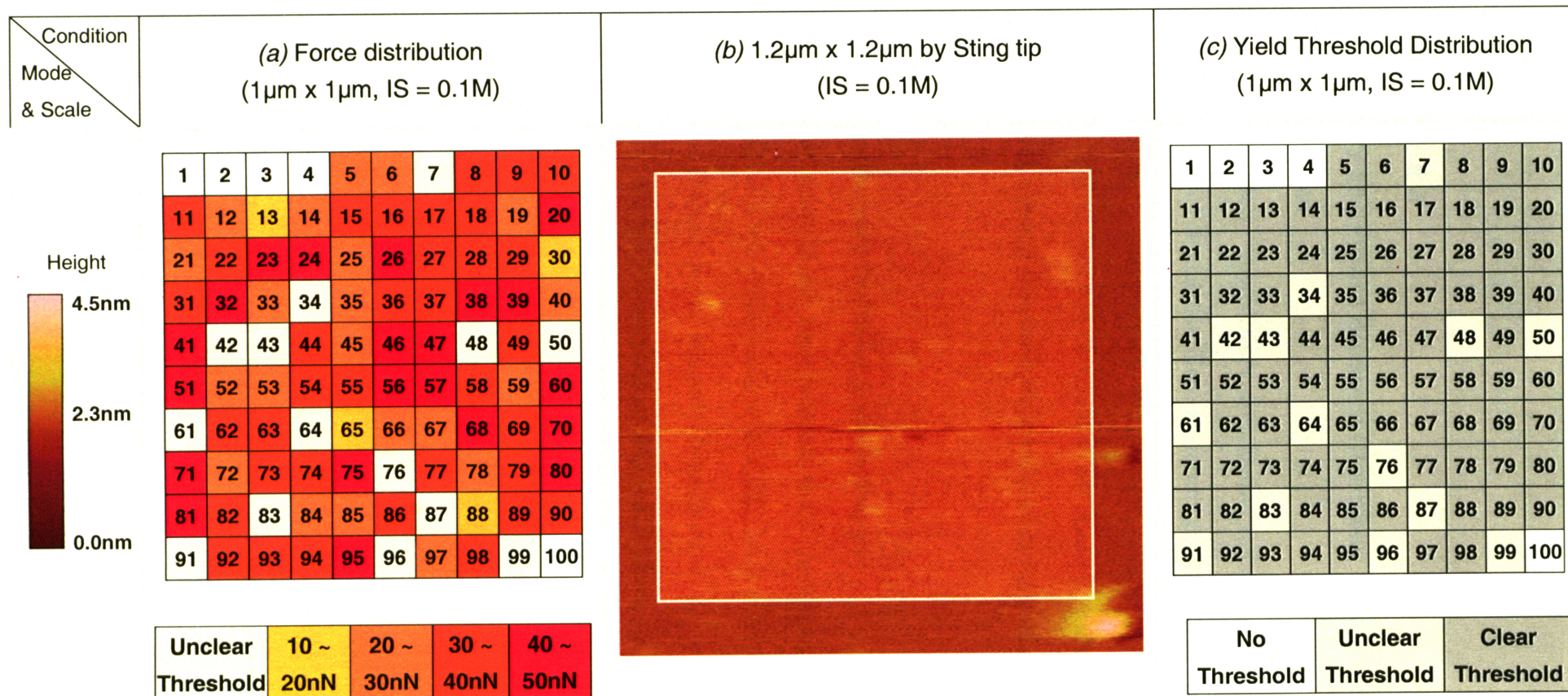


Figure 5-8 (a) Force distribution, (b) AFM image, and (c) Threshold distribution (1 μ m x 1 μ m size) of HRFS Data with μ masch sting ($R_{tip} \sim 30$ nm) probe tip (0.1M IS). Each space between HRFS experiment is 100nm and only one time HRFS experiment was performed per one position. Colors stand for dark gray: clear yield threshold (well packed DPPC layers), light gray: unclear yield threshold (less packed DPPC layers), white: no yield threshold (no DPPC layers).

CHAPTER 6

Summary and Future Research Directions

6.1 Introduction

This study explored the nanomechanical properties of two prospective protein-resistant hydrated organic thin films: a synthetic polymer, oligo ethylene oxide (C_3EO_5) self-assembled monolayer (SAM), and biomimic polar zwitterionic phosphorylcholine (PC) lipid bilayers. Based on the results of this research, in this chapter, I offer options for designing a protein-resistant surface and provide suggestions for future directions of study.

6.2 Protein Resistant Design for Synthetic Polymer

The result of the high-resolution force spectroscopy (HRFS) study clearly shows a repulsive interaction between the C_3EO_5 SAM at 60-80% surface coverage and the protein (human serum albumin) functionalized tip or any other hydrophilic, hydrophobic, or negatively-charged tip. The results showed that the repulsive forces are caused not only by the “flexibility” (mobility) of the C_3EO_5 SAM in a contact regime but also by the “long-range electrostatic repulsion” from the negative charge of the protein-functionalized tip vs. the effective negative surface charge from the bigger dipolar moment of a less ordered C_3EO_5 chemical structure at 60-80% surface coverage in a noncontact interaction regime, (Figure 6-1). Moreover, the short-range hydrogen bonded water-layers in a noncontact regime also were shown to cause repulsive forces (Figure 6-1). In the case of hydrogen-bonded water layers, more repulsive forces occur when more hydrophilic ethylene oxide groups are exposed on the surface. These three components are necessary to create a protein resistant surface.

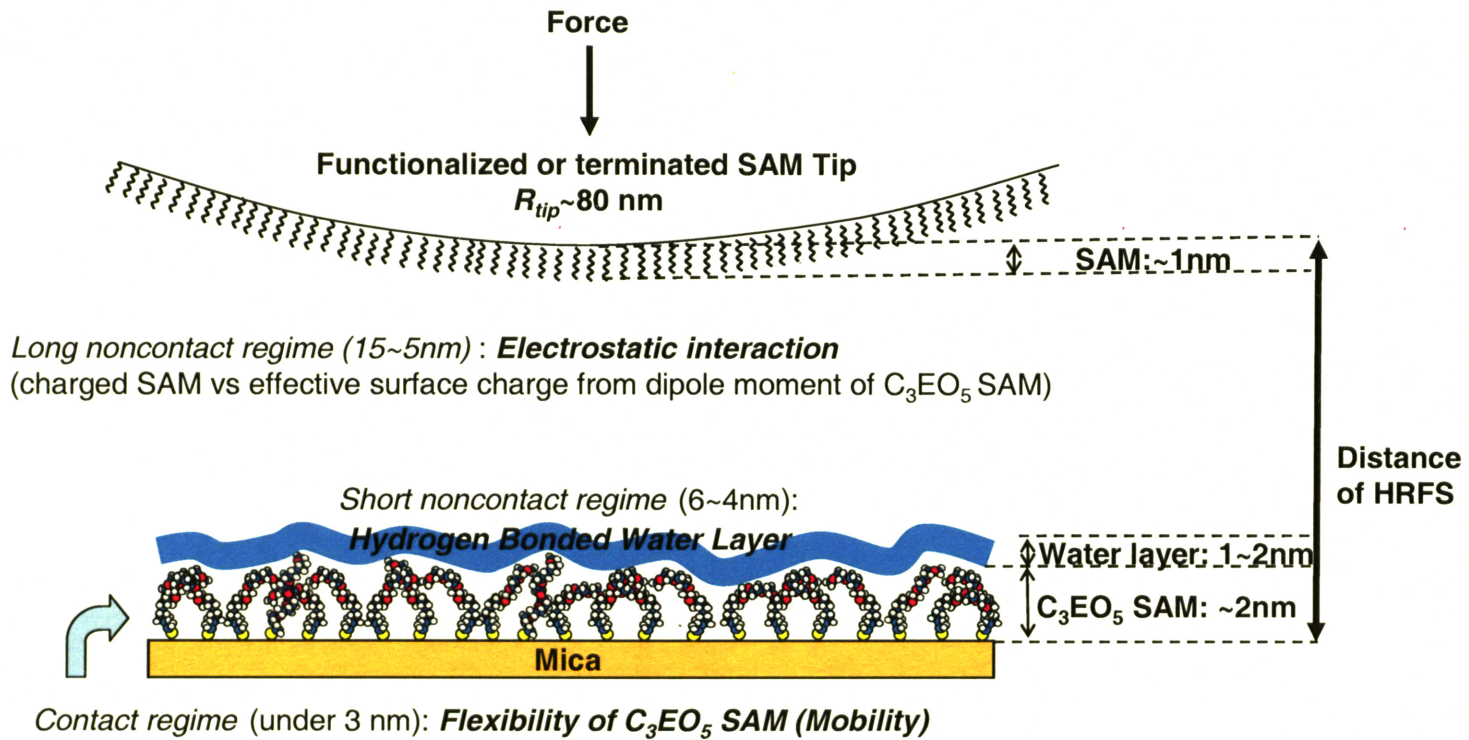


Figure 6-1 Repulsive interaction mechanism of the HRFS experiment between protein functionalized or chemically terminated tip vs. C_3EO_5 SAM at 60-80% surface coverage.

In short, the design of a protein resistant oligo ethylene oxide surface requires a proper surface-packing density that can maximize the dipole moment (from helical or amorphous conformation) and the formation of a water layer and the flexibility of the oligo ethylene oxide itself. However, if the surface packing density is too low, the effect from the Au substrate should be considered. Therefore, it is important to find the proper surface-packing density that can enable the entire surface coverage to screen the effect from the substrate with the less-ordered conformation, which can maximize the dipole moment of both the structure and the hydrated water layers. In addition, the durability of the thiol-bonded SAM on the Au substrate should be evaluated for long-term usage.

Alternatively, instead of using the Au substrate, a graft copolymer that has two subunits can be employed (Figure 6-2). The structure unit 1 should be attached to the targeted surface by chemical bonding. By changing the sequence of Structural Unit 2, which can be an oligo ethylene oxide, the grafting density can be controlled. If Structural Unit 1 is also hydrophilic, it can also improve protein resistance because it helps to create hydrated water layers.

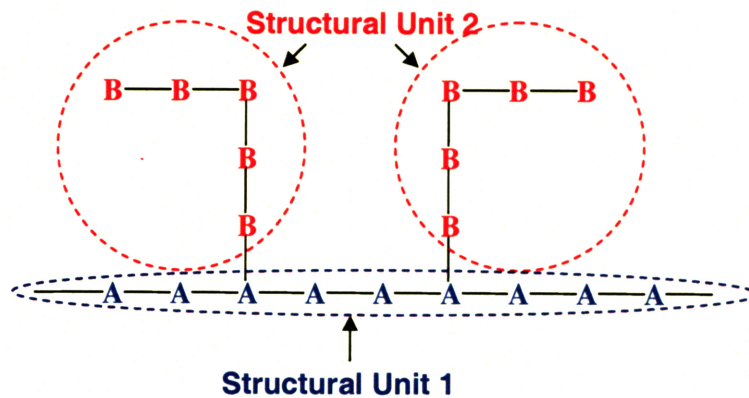


Figure 6-2. Example of a graft copolymer. A & B are monomers. Structural Unit 1 is composed of A monomers and Structural Unit 2, of B monomers.

Another key factor to be considered is the length and shape of Structural Unit 2. If it is much longer than the size of the protein, it does not provide resistance to the small and elliptical-shaped proteins (the thickness along the semi-major axis is about 2-3 nm)¹²⁹ because these small proteins can get stuck between the long chains. In this sense, it is best to use a short oligo ethylene oxide, the height of which is about 2 nm for C₃EO₅ rather than long chains such as PEO and PEG.

In short, to design an optimal protein-resistant surface by using a grafted ethylene-oxide-based oligomer or polymer, the surface-packing density and length of the chemical structure should be optimized to maximize the dipole moment, the hydrated surface water layers and the flexibility of the chemical structure.

6.3 Protein Resistant Design for Phosphorylcholine (PC) Lipid Bilayers

This study examined the nanomechanical properties of zwitterionic DPPC and POPC lipid bilayers. As discussed in Chapters 1 and 3, these lipid bilayers are protein resistant because of the hydrophilic and zwitterionic head groups. One of the most important factors of a protein-resistant design for PC lipids is that the lipid bilayers

should be homogeneous across the overall surface to prevent clogging or coagulation in the holes. On the other hand, this homogeneous surface should be strong enough to endure high pressures such as in high blood pressure (human medical) contexts. Therefore, we must understand the structural properties of the lipid bilayers. As shown in Chapters 4 and 5, the lipid bilayers have high yield threshold forces whereby the overall surface becomes more homogeneous as the ionic strength increases. It is quite noticeable that with 0.1 M IS, which is similar to the IS of human blood, the DPPC lipid bilayer has good structural properties in an overall area even if yield threshold forces periodically rise and fall based on the positions of HRFS experiment. It seems that this periodic change in structural property is the nature of the PC lipid bilayer. In addition, the proper incubating approach, the direct-deposit method, can improve the homogeneity of the lipid layer.

Another factor that can improve the design of a protein-resistant homogeneous PC lipid bilayer is the length of the hydrophobic tail group; the longer the tail group the better it will bind and stabilize lipids.

To apply this lipid layer system to an actual product such as a bio-device or artificial artery, one could modify the lipid tail group polymerization with a proper incubating method. In this way, the lipid group will consistently remain on the surface and retain its strong mechanical property.

As shown in the study of the lipid bilayer, the length scale and geometry of the AFM probe tip are crucial to understanding and designing solid nanomechanical properties because the improper use of the tip can underestimate or overestimate the nanomechanical properties of hydrated organic thin films.

6.4 Future work

This research suggests three directions for future study. First, the optimization of the graft copolymer, which was discussed in Section 6.2, could be studied to further maximize protein resistance. A study using HRFS and AFM imaging of the graft copolymer could be compared to the MD simulation of it to better understand the protein-resistant mechanism.

Second, the durability of the OEO-SEMs needs to be further studied in order to apply them to biosensors, biological implants, and marine antifouling coatings, etc. Also, the enhanced attachment of OEO-SEMs on the substrate and the prevention of the degradation of OEO-SEMs should be studied.

Third, the potential protein resistance of the PC Lipid bilayer combined with other components such as oligosaccharides and sterols that mimic the endothelium cell could be studied via HRFS and MD simulations. Because oligosaccharides are hydrophilic and because sterols increase the structural strength of the lipid layers, both seem to improve protein resistance. The polymerization of these combinations could be applied to actual bio-devices.

Forth, the length scale (from microscale to nanoscale) and geometry effect of the AFM probe tip on the thin films need to be further studied because as they relate to the study of the representative elementary volume (REV) of nanometer- and micrometer-scale materials. If the length scale of the tip is too much larger or smaller than that of REV, it can not detect the proper nanomechanical properties of material. In addition, the proper tip speed of HRFS should be studied in greater depth in order to measure the proper nanomechanical properties of the application of the materials.

APPENDIX

Self-Assembled Monolayers (SAMs)

The chemisorption of linear thiols (in this research, OEO-SAMs) to Au (111) creates an equally spaced and stable SAM with 100% surface packing density^{130,131,132} (Figure A-1). The thiol bonding on Au is more favorable than other kinds of bonding. The thiol bonding mechanism is still being studied.^{133,134} To explore the binding state of the Au-S head group, X-ray photoelectron spectroscopy (XPS) has been used to show the S 2p photoemission spectra.¹³⁴ The size of S 2p spectra is changed according to the packing density of thiol-bonded self assembled monolayer on Au.¹³⁴

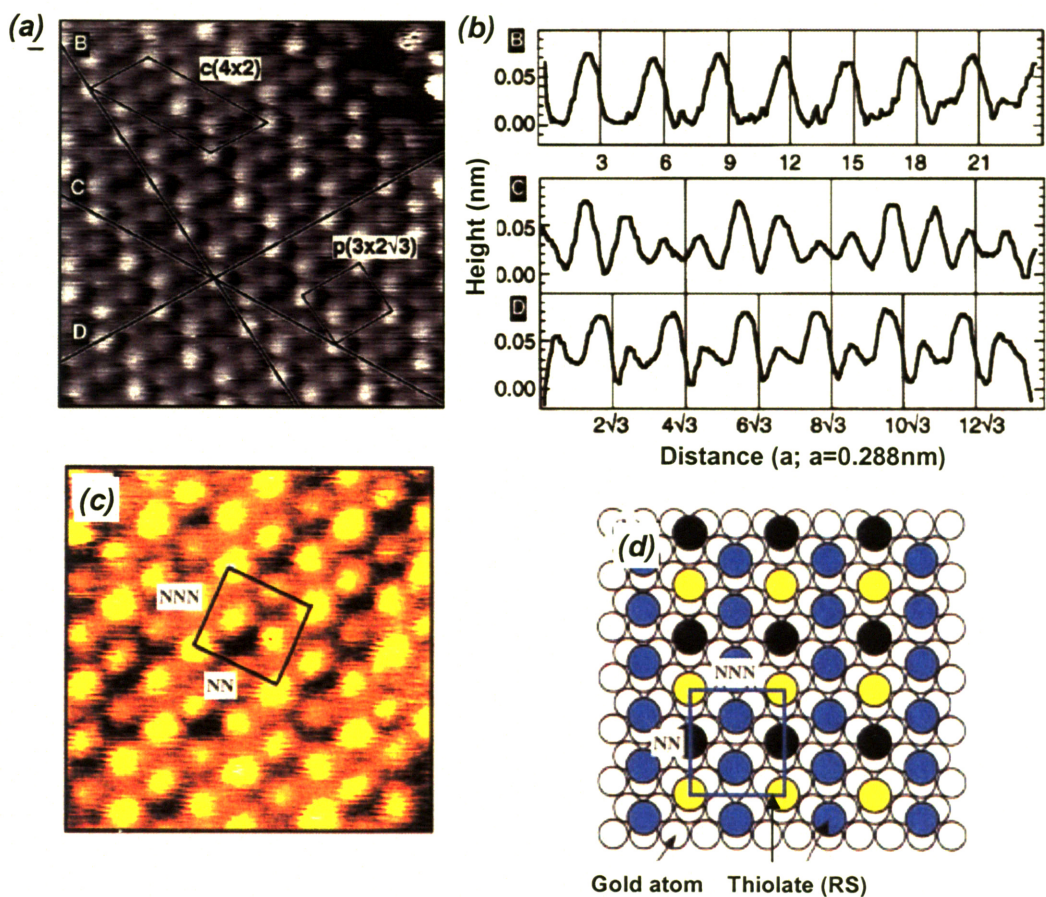


Figure A-1 (a) STM image (6nm x 6nm) of Oxtanethiol on Au (111). The $(2\sqrt{3} \times 3)$ unit mesh and $c(4 \times 2)$ superlattice unit cell are outlined¹³¹. (b) Plot of cross-section B in (a) running in the Au nearest-neighbor (NN) direction. (C and D) Cross-sectional plots running in two of the Au next-nearest-neighbor (NNN) directions.¹³¹ (c) High-resolution STM image showing $c(4 \times 2)$ superstructure containing three different molecular states in a unit cell (3.8 nm \times 3.8 nm)¹³². (d) Schematic model describing the $c(4 \times 2)$ superstructure. White circles correspond to gold atoms and colored circles correspond to alkanethiol molecules.¹³²

REFERENCES

1. Wade, L. G., Jr., *Organic Chemistry*, Fifth edition, Prentice Hall, Upper Saddle River, NJUSA, 2003.
2. Ulman, A. (Editor), et al., *Organic Thin Films and Surfaces: Directions for the Nineties*, Vol. 20, Elsevier Science & Technology Books, 1995.
3. Dee, K. C., et al., *An introduction to tissue-biomaterial interactions*, Wiley-Liss, Hoboken, NJUSA, 2002.
4. Jordan, S. W., et al., *Biomaterials*, 2006, 27, 3473-3481.
5. Hanefeld, P., et al., *Biomacromolecules*, 2006, 7, 2086-2090.
6. Domb, A. J.; Kost, J.; Wisemann, D. M. *Handbook of Biodegradable Polymers*; Harwood Academic Publishers: Chichester, U.K., 1997.
7. Szleifer, I., *Biophys. J.*, 1997, 72, 595.
8. Szleifer, I., *Current Opinion in Solid State and Materials Science*, 1997, 2, 337-344
9. Halperin, A., *Langmuir*, 1999, 15, 2525-2533.
10. Leckband, D., *Annu. Rev. Biophys. Biomol. Struct.*, 2000, 29, 1-26.
11. Ostuni, E., et al., *Langmuir*, 2001, 17, 6336-6343.
12. Ostuni, E., et al., *Langmuir*, 2001, 17, 5605-5620.
13. Massia, S. P., et al., *Biomaterials* 2000, 21, 2253-2261.
14. Ostuni, E., et al., *Langmuir*, 2003, 19, 1861-1872.
15. Ostuni, E., et al., *Colloids and Surfaces B: Biointerfaces*, 1999, 15, 3-30.
16. Ishihara, K., et al., *J. Biomed. Mater. Res.*, 1998, 39, 323-329.
17. Ross, E. E., et al., *Langmuir*, 2001, 17, 2305-2307.
18. Ishihara, K., et al., *J. Biomed. Mater. Res.*, 1998, 39, 323-329.
19. Dicke, C., et al., *J. Phys. Chem. B*, 2002, 106, 4450-4456.
20. Dicke, C., et al., *J. Am. Chem. Soc.*, 2002, 124, 12619-12625.
21. Feldman, K., et al., *JACS*, 1999, 121, 10134-10141.
22. Efremova, N. V., et al., *Biochemistry*, 2000, 39, 3441-3451.
23. Huang, N. P., et al., *Langmuir*, 2001, 17, 489-498.
24. Metzke, M., et al., *J. Am. Chem. Soc.*, 2003, 125, 7760-7761.
25. Cevc G., *Biophysical Chemistry*, 1995, 55, 43-53.
26. Pictures from http://en.wikipedia.org/wiki/Ethylene_oxide.

-
27. Harder, P., et al., *J. Phys. Chem. B*, **1998**, 102, 426.
 28. Jeon, S. I., et al., *J. Colloid Interface Sci.*, **1991**, 142, 149-158.
 29. Jeon, S. I.; et al, *J. Colloid Interface Sci.*, **1991**, 142, 159-166.
 30. Herrwerth, S., et al., *JACS*, **2003**, 125, 9359-9366.
 31. Wang, R. L. C., et al., *J. Chem. Phys.*, **1997**, 101, 9767.
 32. Pertsin, A. J., et al., *J. Phys. Chem. B*, **1998**, 102, 4918-4926.
 33. Dormidontova, E. E., *Macromolecules*, 35, **2002**, 387-1001.
 34. Bedrov D., et al., *Langmuir*, 22, **2006**, 6189-6194.
 35. Zheng, J., et al., *Biophysical Journal*, Vol. 89, **2005**, 158-166.
 36. Vanderah, D.J., et al., *J. Am. Chem. Soc.*, **2004**, 126, 13639-13641.
 37. 3D Chemical drawing was modified from the similar helical structure of EO₆ provided by David Vanderah.
 38. Vanderah, D. J., *Langmuir*, **2002**, 18, 4674-4680.
 39. Takahashi, Y., et al., *Macromolecule*, 1973, 23, 672-675.
 40. Garcia-Manyes, S., et al., *Biophysical Journal*, **2005**, 89, 4261-4274.
 41. Keough, K., *Biophysical Journal*, **2003**, 85, 2785-2786.
 42. Leckband, D. et al., *Quarterly Reviews of Biophysics*, **2001**, 34, 2, 105-267.
 43. Butt, H., et al. *Surface Science Reports*, **2005**, 59, 1-152.
 44. Lingler, S., et al. *Langmuir*, **1997**, 13, 7085-7091.
 45. Spangenberg, T., et al., *Phys. Stat. Sol.*, **2004**, (a) 201, No. 5, 857-860.
 46. Von Smoluchowski, M. Z., *Phys. Chem.*, **1917**, 92, 129-168.
 47. Kramers, H. A. *Physica*, **1940**, 7, 284
 48. Hammes, G. G., *Principles of Chemical Kinetics*; Academic Press.: New York, **1978**.
 49. Van Oss, C. J., *Journal of Molecular Recognition*, **1997**.
 50. Verwey, E., et al., *Theory of Stability of Lyophobic Colloids*, Elsevier, Amsterdam, The Netherlands, **1948**.
 51. Derjaguin, B. V., et al., *Acta Physiochim.*, URSS, **1941**, 14, 633.
 52. Derjaguin, B. V., *Kolloid Z.*, **1934**, 69, 155-164.
 53. http://en.wikipedia.org/wiki/Blood_pressure#_note-8.
 54. Chambers, L. D., *Surface & Coatings Technology*, **2006**, 201 3642-3652.

-
55. Nogaoka, S., et al., *Polymers as Biomaterials*; Shalaby, S., Hoffman, A., Ratner, B. D., Horbett, T. A., Eds.; Plenum Press: New York, **1984**; 361-374.
 56. Satulovsky, J., et al., *PNAS*, **2000**, 97, 9037-9041.
 57. Herrwerth, S., et al., *JACS*, **2003**, 125, 9359-9366.
 58. Wang, R. L. C., et al., *PCCP*, **2000**, 2, 3613-3622.
 59. Wang, R. L. C., et al., *PCCP*, **1999**, 2, 1721-1727.
 60. Pertsin, A. J., et al., *PCCP*, **2000**, 2, 1729-1733.
 61. Desai, D. V. M., et al., *Journal of Radioanalytical and Nuclear Chemistry*, **1994**, 187, 197-205
 62. US National Library of Medicine: <http://www.nlm.nih.gov/medlineplus/ency/article/003398.htm>.
 63. The physics fact book edited by Glenn Alert: <http://hypertextbook.com/facts/1999/IrinaVinar.shtml>.
 64. Science and Public Health, June 2006, page 402: <http://www.ama-assn.org/ama1/pub/upload/mm/38/a-06csaph.pdf>.
 65. Sturges, H. A., *J. American Statistical Association*, **1926**, 65-66.
 66. Creager, S. E., et al., *Langmuir*, **1994**, 10, 3675.
 67. Smalley, J. F., *J. Phys. Chem. B*, **1999**, 103, 1676-1685.
 68. Israelachvili, J., *Intermolecular & Surface Forces. Second edition*, Academic Press, **1992**.
 69. Bell, G. M., et al., *J. Colloid Interface Sci.*, **1980**, 74, 530-548.
 70. Belaya, M., et al., *Langmuir*, **1994**, 10, 2010-2014.
 71. Vandivar, J., et al., *Journal of Biomedical Materials Research: Part A*, **2006**, 78A, (2), 352-363.
 72. Rixman, M. A., et al., *Langmuir*, **2003**, 19, 9357-9372.
 73. Control data of Professor Christine Ortiz's group
 74. Sethuraman, A., et al., *Langmuir*, **2004**, 20, 7779-7788.
 75. Lee, J. H., et al., *Prog. Polym. Sci.*, **1995**, 20, 1043-1079.
 76. Sackmann, E., *Science*, **1996**, 271, 43-48.
 77. Künneke, S., et al., *Biophysics Journal*, **2004**, 86, 1546.
 78. Ross, E. E., et al., *Langmuir*, **2003**, 19, 1766.

-
79. Artyukhin, A. B., *Ind. Eng. Chem. Res.*, **2003**, 42, 2156.
 80. Silin, V. I., et al., *JACS*, **2002**, 124, 14683.
 81. Papo, N., et al., *Biochem.*, **2004**, 43, 6393.
 82. Rossi, S., et al., *Biochem.*, **2003**, 42, 15273.
 83. Reimhult, E., et al., *Langmuir*, **2003**, 19, 1681.
 84. Kam, L., et al., *Journal of Biomedical Materials Research*, **2001**, 487.
 85. Reviakine, I., et al., *Langmuir*, **2000**, 16, 1806.
 86. Chan, P., et al., *J. Cell. Bio.*, **1991**, 115, 245.
 87. Malmsten, M., *J. Colloid Interface Sci.*, **1995**, 172, 106-115.
 88. Malmsten, M., *Colloids Surf., A*, **1999**, 159, 77-87.
 89. Terrettaz, S. et al., *Langmuir*, **1993**, 9, 1361-1369.
 90. Puu, G., *Anal. Chem.*, **2001**, 73, 72-79.
 91. Glasmästar, K. et al., *J. Colloid Interface Sci.*, **2002**, 246, 40-47.
 92. Israelachvili, J., *Intermolecular & Surface Forces. Second edition*, Academic Press, p375, **1992**.
 93. Chiras, D., *Human biology*. Jones & Bartlett Pub. **1997**.
 94. Zhang, L., et al., *Langmuir*, **2002**, 18, 1318.
 95. Mann, D. A., et al., *JACS*, **1998**, 120:41, 10575.
 96. Plant, A. L., et al., *Langmuir*, **1993**, 9, 2764.
 97. Keough, K., *Biophysical Journal*, **2003**, 85, 2785-2786.
 98. Higgins, M. J., et al., *Biophysical Journal*, **2006**, 91, 2532-2542.
 99. Seantier, B., et al., *Nano Letters*, **2004**, 4, 1-5.
 100. Jass, J., et al., *Biophysical Journal*, **2000**, 79, 3153.
 101. Deleu, M., et al., *Biophysical Journal*, **1999**, 77, 2304.
 102. Steinem, C., et al., *Phys. Chem. Chem. Phys.*, **2000**, 2, 4580-4585.
 103. Garcia-Manyes, S., et al., *Biophysical Journal*, **2005**, 89, 1812-1826.
 104. Garcia-Manyes, S., et al., *Biophysical Journal*, **2005**, 89, 4261-4274.
 105. Fukuma, T., et al., *Biophysical Journal*, **2007**, 92, 3603-3609.
 106. Lopez, C. F., et al., *J. Phys. Chem. B*, **2004**, 108, 6603-6610.
 107. Perera, L., et al., *Langmuir*, **1996**, 12, 2625-2629.
 108. Lipowsky, R., et al., *Mol. Cryst. Liq. Cryst.*, **1991**, 202, 17-25.

-
109. Seifert, U., *Phys. Rev. A*, **1991**, 43, 6803-6814.
110. Seifert, U., et al., *Phys. Rev. A*, **1990**, 42, 4768-4771.
111. Lipowsky, R., et al, *Langmuir*, **1991**, 7, 1867-1873.
112. Lipowsky, R., *Festkörperprobleme - Advances in Solid State Physics 32*; **1992**; Vol. 32, 19-44.
113. Zhdanov, V. P., et al., *Langmuir*, **2001**, 17, 3518-3521.
114. Zhdanov, V. P., et al., *J. Chem. Phys.*, **2000**, 112, 900-909.
115. Keller, C. A., et al., *Phys. Rev. Lett.*, **2000**, 84, 54443-55446.
116. Lipowsky, R., *Nature*, **1991**, 349, 475-481.
117. Lipowsky, R., et al., *Mol. Cryst. Liq. Cryst.*, **1991**, 202, 17-25.
118. Noh, J., et. al., *RIKEN Review*, **2001**, No. 38, 49-51.
119. Richter, R. P., et al., *Langmuir*, **2003**, 19, 1632-1640.
120. Wong, J. Y., et al., *Biophysical Journal*, **1999**, 77, 1458-1568.
121. Künerk, S., et al., *Biophysical Journal*, **2004**, 86, 1545-1553.
122. Schneider, J., et al., *Biophysical Journal*, **2000**, 79, 1107-1119.
123. Schneider, J., et al., *Langmuir*, **2003**, 19, 1899-1907.
124. Franz, V., et al., *Colloids and Surfaces B: Biointerfaces*, **2002**, 23, 191-200.
125. Garcia-Manyes, S., et al., *Anal. Chem.*, **2006**, 78, 61-70.
126. Oncins, G., et al., *Langmuir*, **2005**, 21, 7373-7379.
127. Butt, H., et al., *Physical Review E*, **2002**, 66, 031601.
128. Hafner, J., H., et al., *Probes in scanning in microscopies, Handbook of Nanotechnology*, Second Edition, Springer, **2007**.
129. Weiss, Ch., *Human Physiology* (R. F. Schmidt and G. Thews Eds.), Ch. 16, Springer-Verlag, Berlin, **1983**.
130. Schriber, F., *Progress in Surface Science*, **2000**, 65, 151-256.
131. Poirier, G. E., et al., *Langmuir*, **1994**, 10, 2853.
132. Noh, J., et al., *RIKEN Review*, **2001**, No. 38, 49-51.
133. Grönbeck, H., et al., *J. Am. Chem. Soc.*, **2000**, 122, 3839-3842.
134. Yang, Y. W., et al., *Langmuir*, **2002**, 18, 1157-1164.